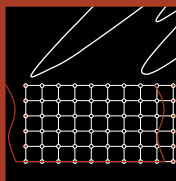
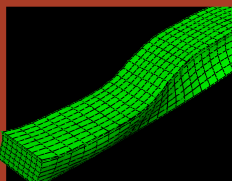
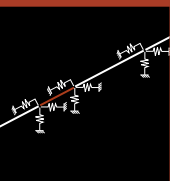
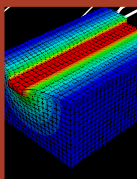
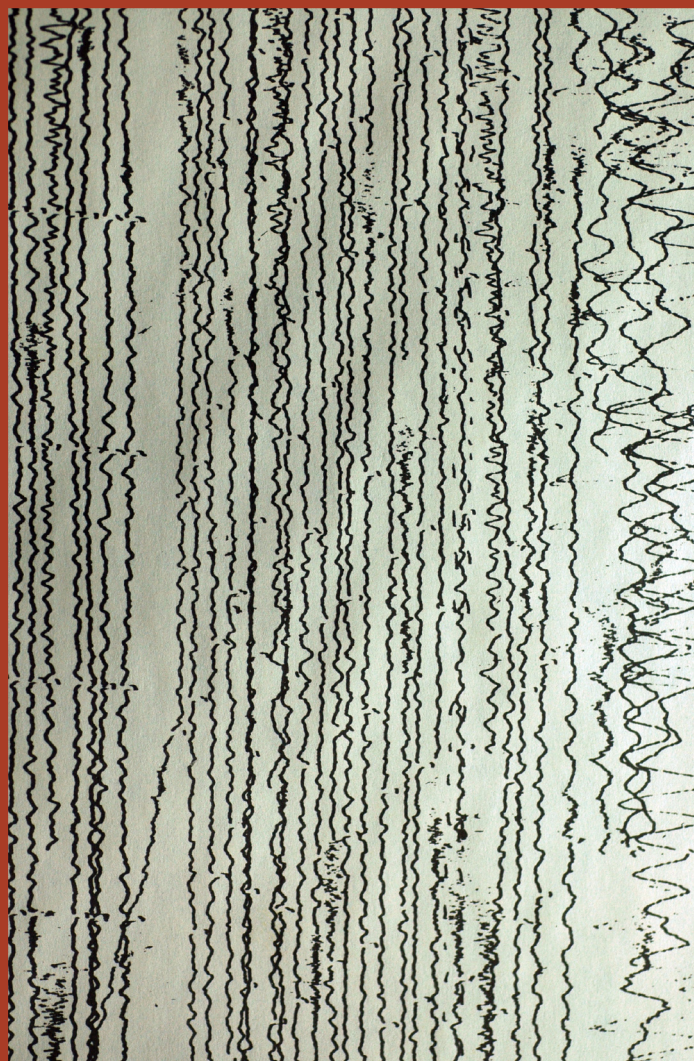
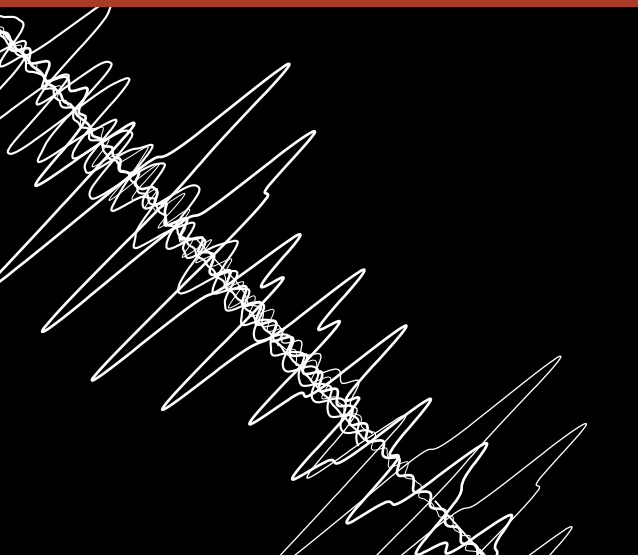


# MODEL ACCURACY IN ASEISMIC DESIGN OF IMMERSSED TUNNEL



Master's Thesis, 2008  
Jakob Hausgaard Lyngs  
Master of Science in Civil and Structural Engineering  
The School of Civil Engineering, Aalborg University



# *Model accuracy in aseismic design of immersed tunnel*

---

MASTER'S THESIS  
THE SCHOOL OF CIVIL ENGINEERING  
MASTER OF SCIENCE IN CIVIL AND STRUCTURAL ENGINEERING  
AALBORG UNIVERSITY, 2008

*Jakob Hausgaard Lyngs*



## PREFACE

This master's thesis is prepared at the Master of Science Programme in Civil and Structural Engineering at Aalborg University, Denmark. The thesis is the outcome of a long candidate project on the 3<sup>rd</sup> and 4<sup>th</sup> semester. The subject for the project period is Design and Analysis of Advanced/Special Structures.

The thesis consists of the following parts:

- Main thesis
- Appendices. The appendices are located in the back of the main thesis.
- DVD with developed programs, data files, animations, and a pdf-version of the thesis with working hyperlinks. The DVD is found in the back of the thesis.

The thesis project has been supervised by Associate Professor Lars Andersen, whose invaluable inspiration and tutoring have been greatly appreciated. Furthermore, the thesis work has been inspired by the real-world immersed tunnel design experience and knowledge of Senior Project Manager Michael Tonnesen, COWI, and R&D Manager Carsten S. Sørensen, COWI. I would like to thank them for their highly appreciated guidance.

The thesis may also be found on the website [finalthesis.hausgaard-lyngs.dk](http://finalthesis.hausgaard-lyngs.dk).

Aalborg, 11<sup>th</sup> June 2008

---

Jakob Hausgaard Lyngs



## ABSTRACT

This thesis deals with the model accuracy for seismic design of immersed tunnels, like the proposed underwater artery in Thessaloniki, Greece.

The soil response to seismic waves is analysed in the frequency domain by means of the domain transformation method and the finite element method. The seismic response of an immersed tunnel and the damage in the gasket joints have been calculated with a closed form solution, a Winkler-type model, and a full three-dimensional continuum model. The Winkler model and the continuum model are applied in the time domain.

Focus is especially given to the diverging results from the Winkler model, commonly used in seismic design, and the continuum model, which is considered to be more accurate. Through comparative analyses it is shown that the presented Winkler model is not able to model retroaction from the tunnel to the soil. This entails that the presented Winkler model is not suited for seismic design of an immersed tunnel with non-uniform cross section.

Sensitivity analyses are performed to analyse the influence of the many parameters which must be determined for a seismic design. It is shown that the stratification and the soil parameters, together with the earthquake magnitude, influence significantly on the tunnel damage. On the other hand, the modelling of the immersed tunnel gasket joints has very little influence on the calculated gasket deformation. Finally, it is shown that the critical direction of wave propagation is an angle of approximately  $45^\circ$  to the tunnel axis.



## RESUMÉ

Dette afgangprojekt omhandler modelusikkerheder ved jordskælvsdesign af sænketunneler, med en sænketunnel i Thessaloniki i Grækenland som case.

Jordens respons som følge af jordskælvsbølger er analyseret i frekvensdomæne ved hjælp af domænetransformationsmetoden og finite element metoden. Responset af sænketunnelen og skaderne i koblingerne mellem tunnelementerne er beregnet med en løsning på sluttet form, en model af Winkler-typen samt en fuld tredimensionel kontinuummodel. Analyserne med de sidste to modeller foregår i tidsdomæne.

Winkler-modellen anvendes ofte ved jordskælvsdesign, mens kontinuummodellen er anset for at være mere nøjagtig. De to modeller giver meget forskellige resultater, og årsagen til denne forskel er undersøgt nøje. Gennem sammenlignende analyser er det vist, at den opstillede Winkler-model ikke er i stand til at modellere tilbagekobling fra tunnelen til jorden. Dette indebærer at den opstillede Winkler-model ikke er egnet til at designe en sænketunnel med fleksible koblinger mod jordskælv.

Ved design mod jordskælv er der mange parametre der skal bestemmes. For at undersøge hvor nøjagtigt disse parametre bør bestemmes er der udført følsomhedsanalyser. Det er vist at lagdelingen, jordens parametre samt jordskælvets størrelse har stor indflydelse på den beregnede skade på tunnelen. På den anden side har det meget lille betydning for skaden på tunnelen, hvordan det vælges at modellere koblingerne mellem tunnelementerne. Endelig er det vist at den kritiske udbredelsesretning for jordskælvsbølgen er en vinkel på omtrent  $45^\circ$  med tunnelens længdeakse.



# CONTENTS

<b>Preface</b>	<b>i</b>
<b>Abstract</b>	<b>iii</b>
<b>Resumé</b>	<b>v</b>
<b>1 Introduction</b>	<b>1</b>
1.1 Thessaloniki immersed tunnel . . . . .	1
1.2 The thesis . . . . .	3
1.3 Demarcation . . . . .	3
<b>2 Conclusion</b>	<b>5</b>
<b>I Introduction and definitions</b>	<b>9</b>
<b>3 Immersed tunnels</b>	<b>11</b>
3.1 Construction techniques . . . . .	11
3.1.1 Construction and transport . . . . .	11
3.1.2 Installation . . . . .	12
3.2 Advantages of immersed tunnels . . . . .	14
<b>4 Earthquakes</b>	<b>17</b>
4.1 Plate tectonics . . . . .	18
4.2 Wave types . . . . .	19
4.3 Determination of design earthquake . . . . .	21
4.3.1 Size of earthquake . . . . .	21
4.3.2 Seismic hazard analysis . . . . .	22
4.3.3 Code spectra . . . . .	23
4.3.4 The present thesis . . . . .	24
4.4 The influence of earthquakes on underground structures . . . . .	25

## Contents

4.5	Damage modes of tunnels . . . . .	25
4.6	Incoherence . . . . .	26
<b>5</b>	<b>Design Basis</b>	<b>27</b>
5.1	Geometry of tunnel . . . . .	27
5.2	Geotechnical parameters . . . . .	28
5.3	Damping . . . . .	29
5.3.1	Loss factor . . . . .	29
5.3.2	Viscous damping . . . . .	29
5.3.3	Hysteretic damping . . . . .	30
5.3.4	Conversion . . . . .	31
5.4	Design cross section . . . . .	31
5.5	Input motion . . . . .	33
5.5.1	Time series . . . . .	33
5.5.2	Apparent velocity . . . . .	35
5.5.3	Direction of propagation . . . . .	35
5.6	Stiffness of gaskets . . . . .	35
5.6.1	Longitudinal stiffness . . . . .	35
5.6.2	Shear stiffness . . . . .	37
5.7	Damage criterion . . . . .	38
<b>II</b>	<b>Methods of analyses</b>	<b>41</b>
<b>6</b>	<b>Wave propagation through soil</b>	<b>43</b>
6.1	Generalized geometry . . . . .	44
6.2	The domain transformation method . . . . .	45
6.3	The finite element method . . . . .	46
6.3.1	Elements . . . . .	46
6.3.2	Frequency response . . . . .	47
6.3.3	Convergence . . . . .	47
6.3.4	Choice of calculation method . . . . .	48
6.4	Frequency response . . . . .	48
6.5	Earthquake response . . . . .	49
6.5.1	Frequency domain . . . . .	49
6.5.2	Time domain . . . . .	50
<b>7</b>	<b>Closed form solution</b>	<b>53</b>

## Contents

7.1	Axial strain . . . . .	53
7.2	Deformation at gaskets . . . . .	54
7.3	Input . . . . .	54
<b>8</b>	<b>Winkler model</b> . . . . .	<b>57</b>
8.1	Model assumptions . . . . .	58
8.2	Modelling . . . . .	59
8.2.1	Soil spring stiffness . . . . .	59
8.2.2	Gasket stiffness . . . . .	63
8.2.3	Damping . . . . .	64
8.2.4	Discretization . . . . .	64
8.3	Input motion . . . . .	64
8.4	Output . . . . .	65
8.4.1	Translations . . . . .	65
8.4.2	Rotations . . . . .	65
<b>9</b>	<b>Continuum model</b> . . . . .	<b>67</b>
9.1	Parts and meshes . . . . .	67
9.1.1	Tunnel . . . . .	68
9.1.2	Gaskets . . . . .	68
9.1.3	Soil . . . . .	69
9.1.4	Discretization considerations . . . . .	69
9.2	Material modelling . . . . .	70
9.2.1	Soil . . . . .	71
9.2.2	Tunnel . . . . .	71
9.2.3	Gasket . . . . .	71
9.2.4	Damping . . . . .	72
9.2.5	Summary . . . . .	73
9.3	Earthquake loading . . . . .	73
9.4	Assembly . . . . .	75
9.4.1	Ties . . . . .	75
9.4.2	Master and slave surfaces . . . . .	75
9.5	Output . . . . .	76
9.5.1	Deformation at corners . . . . .	76
9.5.2	Degrees of freedom equivalent to Winkler model . . . . .	76
9.6	Verification of models . . . . .	78
9.6.1	Boundary conditions . . . . .	78

## Contents

9.6.2	Representation of free-field soil deformation . . . . .	81
9.6.3	Time step . . . . .	82
<b>III Analyses of methods and parameters</b>		<b>85</b>
<b>10 Comparison of models</b>		<b>87</b>
10.1	Initial results from design basis . . . . .	87
10.1.1	Closed form solution . . . . .	87
10.1.2	Winkler model . . . . .	88
10.1.3	Continuum model . . . . .	88
10.1.4	Comparison . . . . .	89
10.2	The Winkler model vs. the continuum model . . . . .	91
10.2.1	Crude errors . . . . .	91
10.2.2	Three-dimensional wave propagation . . . . .	92
10.2.3	Deformation in gasket . . . . .	92
10.2.4	Importance of retroaction . . . . .	94
10.2.5	Modelling without gaskets . . . . .	99
10.3	Winkler soil springs . . . . .	100
10.4	Prestress in tunnel . . . . .	101
<b>11 Soil parameters and stratification</b>		<b>103</b>
11.1	Method of analysis . . . . .	103
11.2	Impact of layer depths . . . . .	104
11.2.1	Thickness of layer A . . . . .	104
11.2.2	Thickness of layer B . . . . .	105
11.2.3	Distance to bedrock . . . . .	105
11.3	Wave velocity . . . . .	106
11.4	Damping . . . . .	107
11.4.1	Sensitivity . . . . .	107
11.4.2	Hysteretic damping and viscous damping . . . . .	108
<b>12 The earthquake</b>		<b>111</b>
12.1	Apparent velocity . . . . .	111
12.2	Direction . . . . .	113
12.3	Earthquake amplitude . . . . .	116
<b>13 Modelling of gasket joints</b>		<b>117</b>
13.1	Longitudinal stiffness . . . . .	117

13.2 Shear stiffness . . . . .	119
<b>Bibliography</b>	<b>123</b>
<b>Appendices</b>	<b>127</b>
<b>A Derivation of the domain transformation method</b>	<b>129</b>
A.1 Constitutive model . . . . .	129
A.2 Governing equation . . . . .	130
A.3 Transformation into frequency domain . . . . .	130
A.4 Relation between the layers . . . . .	131
A.5 Boundary conditions . . . . .	132
A.6 Solution for inner interfaces . . . . .	133
<b>B Derivation of the finite element method for wave propagation</b>	<b>135</b>
B.1 Geometry and topology . . . . .	135
B.2 Element matrices . . . . .	136
B.2.1 Stiffness matrix . . . . .	136
B.2.2 Mass matrix . . . . .	136
B.3 Solution of the system . . . . .	137
<b>C Enhancements to FE Winkler model</b>	<b>139</b>
C.1 Damping and mass matrices . . . . .	139
C.2 Time integration . . . . .	140
C.3 Forced displacements . . . . .	141
C.4 Spring elements . . . . .	141
<b>D Cross section data</b>	<b>143</b>
D.1 Length of gasket . . . . .	144
D.2 Area . . . . .	144
D.3 Second moment of area . . . . .	144
<b>E Rotation matrices</b>	<b>145</b>



## INTRODUCTION

In this chapter, a brief outline of the Thessaloniki immersed tunnel project and the present thesis project is given.

### 1.1 Thessaloniki immersed tunnel

Thessaloniki is the second-largest city in Greece with a population around one million inhabitants. The location of Thessaloniki is depicted in Figure 1.1. Thessaloniki is located in the Axios-Vardaris zone, adjacent to the Servomakedonian zone, which is characterized as one of the most active seismotectonic zones in Europe. Several active faults are present in the region. (Pitilakis *et al.* 2007, p134)



**Figure 1.1:** Location of Thessaloniki.

This project deals with the seismic design process of a proposed immersed tunnel, planned as a 6-lane road toll-tunnel. The intended location is shown in Figure 1.2 on the following page. The principal objective of the project is to provide congestion relief to the centre of Thessaloniki by the creation of an underground by-pass. The

heavily trafficked avenue on the seafront is to be pedestrianised upon the completion of the tunnel project.



**Figure 1.2:** The location of the immersed tunnel in the Thermaikos Gulf outside the city centre of Thessaloniki. The tunnel is depicted with a red dashed line. (Google Earth 2008)

The immersed tunnel will be about 1.2km in length and is placed on the seabed at a water depth of around 10m. In both ends, the immersed tunnel is linked to cut & cover tunnels. In Figure 1.3 a sketch of the immersed tunnel on the seabed is shown.

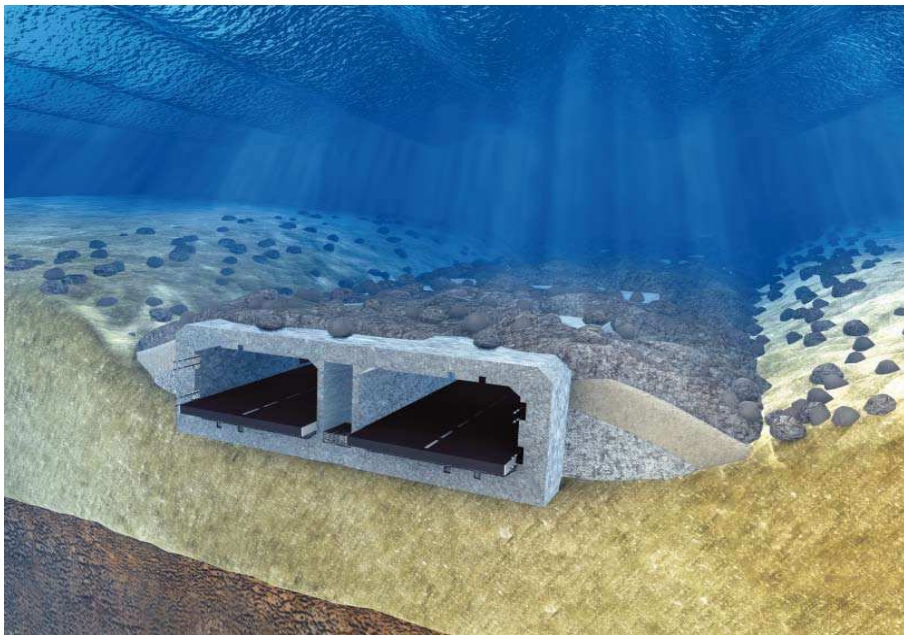


**Figure 1.3:** Illustration of the Thessaloniki tunnel. (COWI 2008)

## 1.2 The thesis

The focus in the present thesis is the accuracy of the presented calculation models for seismic design of immersed tunnels. While the Thessaloniki immersed tunnel is used as case for the thesis project, a final design for the specific tunnel is not provided. Effort is concentrated on the development and analysis of five calculation models: the domain transformation method and the finite element method for wave propagation, and a closed form solution, a Winkler-type model, and a full three-dimensional continuum model for the soil-structure interaction.

The thesis consists of three parts. In Part 1 the basis for the thesis is formed, as the general concepts of immersed tunnels and earthquakes are presented, and a basis of design parameters is found.

In Part 2 the calculation methods are presented. The domain transformation method and the finite element method have been derived and used for a one-dimensional calculation of the wave propagation from bedrock to the level at the immersed tunnel. Thereafter, the closed form solution is presented, followed by the Winkler model and the continuum model.

Part 3 encloses analyses and comparisons of the models. The reasons for divergences in the obtained results are discussed, and sensitivity analyses are performed to clarify the influence of various parameters on the tunnel damage.

Following the bibliography, appendices containing lengthy or trivial derivations not suited for the main thesis are gathered.

## 1.3 Demarcation

To maintain focus on the analysis of the accuracy of the calculation models and to provide a feasible workload, the demarcation of this thesis has elided many potential phenomena. Some of these are:

- **Gasket compression variations**  
Temperature variations will cause the length of the tunnel elements to vary, thereby changing the compression of the gasket joints between the elements. Furthermore, due to relaxation, the compression stress in the gaskets will decrease in time. Both of these effects are disregarded.
- **Cut & cover tunnels**  
The thesis purely deals with the immersed tunnel. The cut & cover tunnels have not been regarded, nor have the connections between the immersed tunnel elements and the cut & cover tunnels been given any considerations.
- **S-waves**  
As it is discussed in Section 4.2 on page 19, only S-waves are regarded for the calculations of the wave propagation.
- **No permanent deformation**  
In the analyses, only transient earthquake motion is analysed. Thus any permanent deformation – which could stem *e.g.* from a fault displacement directly

beneath the tunnel – is disregarded.

- **Damage related to the gasket joints**

Only the deformation in the gaskets are defined as damage in the analyses, as it is discussed in Section 5.7. Thus, the stresses in the tunnel elements are not given any consideration. This is done since *e.g.* Vrettos *et al.* (2007) and Tonnesen (2008) state that the gaskets are normally the critical spots for seismic analyses of immersed tunnels.

- **Linearization**

Even though some rather harsh non-linear problems are dealt with, all of the models presented in this thesis are purely linear. This is chosen in order to reduce computation time, and since it is deemed that only small strains will occur in the dynamic analyses. Also, to utilise the frequency domain, linear material behaviour is a prerequisite. Where very non-linear behaviour is occurring, *e.g.* for the soil and for the gasket behaviour, sensitivity analyses are performed in Part 3 to quantify the possible error.

Also, the use of linear material models entails that nominal tensile stresses will occur in the soil. This is not compatible with the general observed behaviour of (non-cohesive) soils. However, the soil pressures due to gravity are not incorporated in the models, since the dynamic analysis only models oscillations around the state of equilibrium. Thus, the real stresses will most likely vary between more or less compression, making the linear material models acceptable from an engineering point of view.

## CONCLUSION

In the following, the conclusions of the thesis are summarized.

### Part 1

In Part 1 the common basis for the thesis has been established.

The general concepts of immersed tunnels and earthquakes are presented, and the design cross section has been established on the basis of microzonation by Anastasiadis *et al.* (2001) and data from design reports by COWI (2007). An acceleration time series from the 1995 Aegion earthquake has been used as the seismic input, since a seismic hazard analysis is outside the scope of this thesis.

Hysteretic and viscous damping have been applied in the models, and the differences between the mechanisms are discussed. Furthermore, the behaviour of the gasket joints under tunnel axial and cross axial loading has been presented, and the linearization has been discussed. Finally, the damage criterion has been defined as the opening and compression of the gasket joints, which are calculated in the following parts.

### Part 2

In Part 2 the applied calculation models are presented.

The wave propagation from bedrock to the level at the tunnel has been calculated in the frequency domain with the domain transformation method and the finite element method, both of which are derived. It has been shown that the models produce identical results if the finite element method is discretized sufficiently. But since the domain transformation method is based on an analytical solution it is more computational efficient and is used in general in the thesis.

The gasket deformation has been calculated with three different methods. A closed form solution is presented as a very simple way of estimating the order of magnitude of the gasket deformation, based on the free-field soil response.

Subsequently a Winkler-type model has been established, where the immersed tunnel elements are equated with beams, and the soil-structure interaction is modelled with linear springs. The Winkler model has been solved in the time domain by means of a finite element code, which has been developed for this purpose. The model is coded in MATLAB, and the spring stiffness's are determined with ABAQUS and PLAXIS.

Finally, a full three-dimensional continuum model is presented. The model is coded in the commercial finite element code ABAQUS with use of user subroutines and solved in the time domain. The postprocessing is done with MATLAB.

### Part 3

In Part 3 the analyses of the thesis are gathered.

The three different ways of calculating the gasket deformation have been held up against each other. The three models yield very different results. The closed form solution provides nearly twice the deformation of the Winkler model, which furthermore calculates deformations of more than 10 times the deformation of the continuum model.

It may in particular cause surprise that the Winkler model and the continuum model differ with an order of magnitude. The continuum model is regarded as the more accurate model of the physical problem, while the Winkler model is commonly used for seismic design of immersed tunnels. Therefore this divergence has been analysed.

It has been shown that no crude errors have been made in the coding of the models, and that the models yield very similar output if the tunnel is modelled with a uniform cross section. However, the immersed tunnel has a non-uniform cross section, as it consists of concrete tunnel elements which are connected with rubber gaskets.

Through comparative analyses it has been found that the Winkler model fails to model any retroaction from the tunnel to the soil, and this specific property is shown to be the single most significant effect on the gasket deformation. In the continuum model the gasket deformation increases dramatically if retroaction is obstructed. It has been briefly outlined how retroaction could be implemented in the Winkler model, and it is the conclusion that without this enhancement, the Winkler model is *not* suited for modelling of structures with non-uniform cross section, such as the immersed tunnel.

The deformation modes of the immersed tunnel have also been analysed, and it has been found that with the chosen damage criterion, the dominating mode is axial compression and extension, illustrated in Figure 4.10a on page 25. Also, bending of the tunnel provides some gasket deformation, but only approximately 10% of the total deformation.

During design of the immersed tunnel subjected to earthquake strong ground motion, many different parameters must be determined. To analyse the importance of the ac-

curacy of these parameters, sensitivity analyses have been carried out. The thickness, wave velocity and damping parameters of the subsoil layers have been analysed, together with the apparent velocity, angle of propagation and displacement amplitude of the earthquake. Finally, the gasket joint behaviour is analysed.

The results from the sensitivity analyses indicate first and foremost, that the general linearization is acceptable. The gasket behaviour is in principle very non-linear, but it is shown that the gasket deformation is highly insensitive to variations in the gasket stiffness. Thus, only little effort should be given to the determination of the gasket stiffness for a final design. Furthermore, the general non-linear behaviour of soil will not influence significantly on the gasket deformation, cf. Section 10.3.

The sensitivity analyses further show, that the most important parameters to define are those related to the ground conditions at the project site. The stratification and the wave speed may exert significant influence on the gasket deformation. The analyses show that the eigenfrequency of the soil column influences the results. Thus, it is not possible to choose the stratification and the soil parameters on the safe side without performing sensitivity analyses. Furthermore, the determination of the correct design earthquake obviously will exert significant influence on the calculated tunnel damage.

The influence of the apparent velocity – the observed propagation velocity of the earthquake wave front at the ground surface – is only moderate according to the sensitivity analysis. For increasing apparent velocity the tunnel damage decreases, and therefore the apparent velocity for a final design should be chosen as the lowest reasonable value. Additionally, it has been shown that the critical direction of wave propagation is oblique to the tunnel with an angle of approximately  $45^\circ$ . Finally, it is shown that the chosen damping parameters only have very little influence on the tunnel damage.

It should be noted, that for normalized deformation, the continuum model, the Winkler model, and, where applicable, the closed form solution, provide very similar results for most of the sensitivity analyses. Thus, even though the Winkler model and the closed form solution in general provide overly conservative results for the gasket deformation, these models can be used for some parameter analyses.



PART I

**INTRODUCTION AND DEFINITIONS**



## IMMERSED TUNNELS

Tunnels are, in general, constructions used to pass under soil, mountains or water. The construction techniques are many and count among others bored tunnels, cut & cover tunnels, NATM tunnels, blasted tunnels and floating tunnels, each type of tunnel having its specific strengths. The choice of tunnel type depends *i.a.* on economy, the geography of the project site, and the construction time. In Thessaloniki, an immersed tunnel connected with cut & cover tunnels on shore is under design. In the present chapter, the immersed tunnel type will be described.

### 3.1 Construction techniques

An immersed tunnel consists of prefabricated tunnel elements, made so that when temporary bulkheads are applied in both ends, a tunnel element can be floated to the project site. There, the tunnel elements are, one by one, lowered into an excavated trench in the seabed. Finally, the trench are backfilled around the tunnel.

The construction methods of immersed tunnels are developed in the beginning of the 1900s in the USA. The cross sections were at that time typically circular and of steel. In the 1930s rectangular cross sections of reinforced concrete were developed in Europe. (DGF 2005, p137)

#### 3.1.1 Construction and transport

The tunnel elements are constructed on shore, and are typically of 100m to 180m in length. A suitable area of the right size and connected with the project site with waterways has to be found. A veritable dry dock is built by damming the construction area, as it can be seen in Figure 3.1 on the next page. With respect to an optimization based

on time and economy, the dry dock should be able to contain all, or some fraction, of the tunnel elements.



**Figure 3.1:** The Conwy tunnel in Wales during construction (1988). The connection tunnels are fully constructed, and plugged with bulkheads. The completed immersed tunnel elements in the dry dock can be seen in the lower left corner. (DGF 2005, p140)

When the construction of a series of tunnel elements has finished, temporary bulkheads are applied to the ends of the tunnel elements. The tunnel elements are now floated off to the project site, either on barges or simply, if the tunnel elements have positive buoyancy, with the help of tugboats, as it can be seen in Figure 3.2.



**Figure 3.2:** Tug boats manoeuvring an immersed tunnel element. (ITA 1999)

### 3.1.2 Installation

When arrived at the project site, the tunnel elements are installed one by one. The tunnel element is ballasted with water until negative buoyancy exists, and the tun-

## Installation

nel element is lowered into the excavated trench with the help of cranes mounted on barges. The lowering process is illustrated in Figure 3.3.

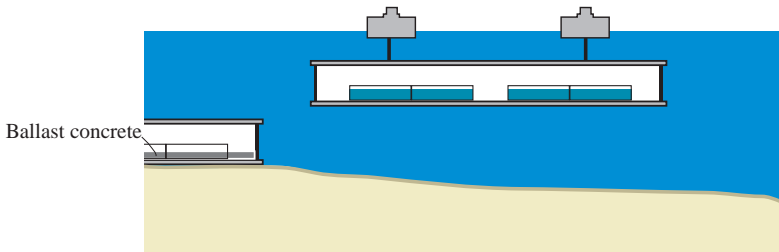


**Figure 3.3:** Lowering of an immersed tunnel element. After Trelleborg (2007).

On one of the tunnel ends, a gasket is mounted. The purpose of this gasket is to seal the connection between two adjacent tunnel elements, ensuring the water tightness of the structure. The gaskets used in the tender design in Thessaloniki are *Gina* gasket profiles, manufactured by Trelleborg Bakker, The Netherlands. (COWI 2007) In Figure 3.4, a cross section and a mounted gasket are depicted.

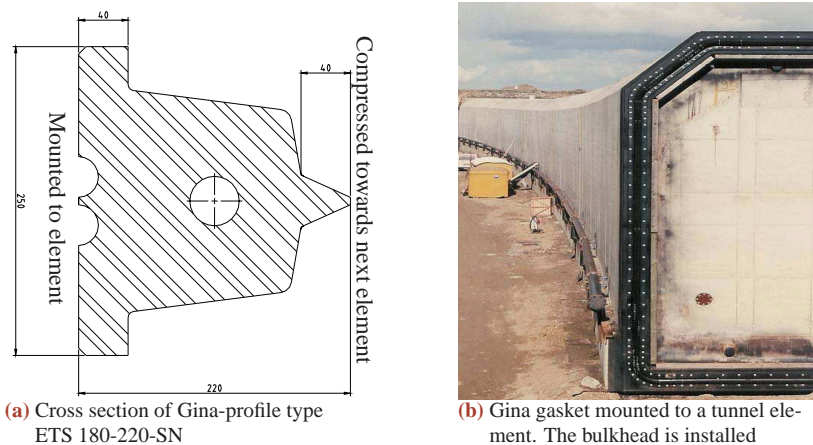


**Figure 3.4:** Gina gasket profile. (Trelleborg 2007)

The tunnel element is placed adjacent to the previously installed element (or the cut & cover tunnel in Thessaloniki, if it is the first element to be placed). The steps in the coupling of the two tunnel elements are illustrated in Figure 3.5.

The tunnel elements are pulled against each other, and the gasket compresses and forms a reservoir between the bulkheads, cf. Figure 3.5b and 3.5c. When the reservoir is emptied and filled with air at atmospheric pressure, the hydrostatic pressure at the free end of the tunnel element under installation compresses the Gina gasket, as it is shown in Figure 3.5d.

Finally, to ensure that the tunnel element stays on the seabed, ballast concrete is cast in the tunnel element, as it is depicted in Figure 3.3.

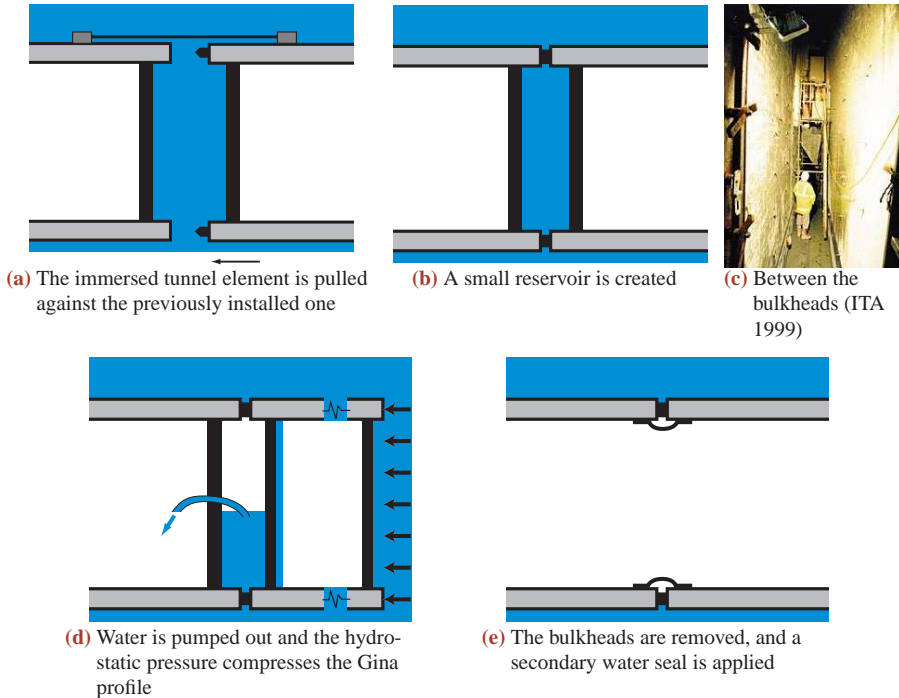


**Figure 3.5:** Coupling of immersed tunnel with Gina gasket. After Trelleborg (2007).

## 3.2 Advantages of immersed tunnels

Immersed tunnels should be considered whenever it is needed to cross water. Typical, the choice will stand between a bored tunnel, an immersed tunnel, or a bridge. Some of the advantages of immersed tunnels are:

- **Alignment**  
Since an immersed tunnel is placed on the seabed, its total length will be less than the length of a bored tunnel, thus reducing costs.
- **Cross section**  
Since the immersed tunnel elements are constructed on shore, it is possible to construct various cross sections. The cross section of a bored tunnel is normally restricted to being circular.
- **Ground conditions**  
While both a bridge and a bored tunnel requires relative good ground conditions, it is possible to install an immersed tunnel in most types of soil, including soft alluvial materials. However, in relation to the topic for the present thesis it should be noted that soft soil may amplify seismic waves significantly.
- **Land availability**  
Even though immersed tunnel construction requires much space for the construction dry dock, this could be located relative far from the project site, making it possible to construct an immersed tunnel in urban areas, such as Thessaloniki.
- **Reclamation**

## Advantages of immersed tunnels

When spotting a site for the construction dock, opportunities to reshape riverbanks and coastlines as part of a tunnel construction scheme may be observed. For example, the specific tunnel construction costs may be reduced if the project is associated with a land reclamation scheme.

- **Construction process**

Compared to the boring of a tunnel or the construction of a bridge, much of the immersed tunnel work is done on shore, in the construction dock. This makes the process easier to handle for the contractor, thus reducing the uncertainties for construction time and budget.

(ITA 1999)

Even though many advantages for immersed tunnels exist, the final choice of construction will always depend on the specific project.



## EARTHQUAKES

The only load condition considered in the present thesis is the earthquake on the immersed tunnel. In this chapter, the basic nature of earthquakes is outlined, and the affection of the strong ground motion of tunnels is described.

Although earthquakes are not very frequent in the region of the world where this university is situated, they have throughout history caused the destruction of countless cities on nearly every continent. Earthquakes are the least understood of the natural hazard and in early days were looked upon as supernatural events. The totally unexpected – nearly instantaneous – devastation of a major earthquake has a unique psychological impact which demands serious consideration by society. (Dowrick 1987)

The destructiveness of earthquakes is most recently illustrated to the international community with the great consequences of the major earthquake of 12 May 2008 in the Sichuan province of China. The casualties count around 70 000, and five million people are left homeless. In Figure 4.1 some of the damage due to the disaster is shown.



**Figure 4.1:** A bank building in Beichuan after the May 2008 Sichuan earthquake. (Commons 2008)

## 4.1 Plate tectonics

An earthquake is a spasm of ground shaking caused by a sudden release of energy in the earth's lithosphere (*i.e.* the crust plus part of the upper mantle). The underlying causes of earthquakes are closely related to the global tectonic processes, which are continually producing mountain ranges and ocean trenches at the earth's surface. The major tectonic plates are depicted in Figure 4.2. (Clough & Penzien 1975, pp522-525) (Dowrick 1987, pp4-6)

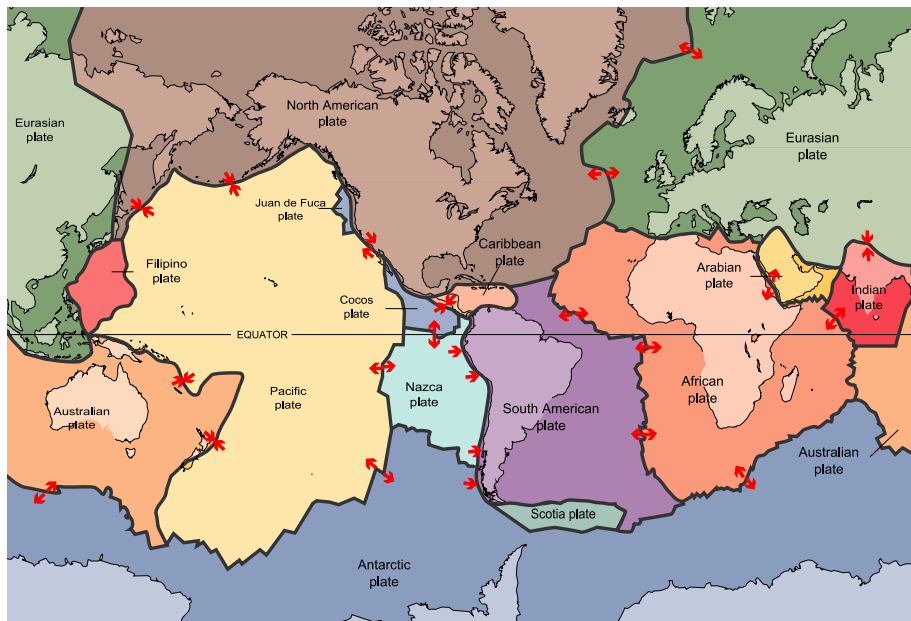


**Figure 4.2:** The major tectonic plates. The red arrows indicates the movement of the plates. (Commons 2006)

Almost all earthquakes occur at the interface between two plates. The movements of the tectonic plates, shown in Figure 4.2 with arrows, are caused by convection in the mantle, shown in Figure 4.3. Where plates spread from each other, a ridge is formed,

## Wave types

and where plates overlap a subduction zone is formed, where the heavier crust plate subducts under the lighter. This is depicted in Figure 4.3. It can be seen in Figure 4.2 that the ridges are mostly formed on the oceanic floor.

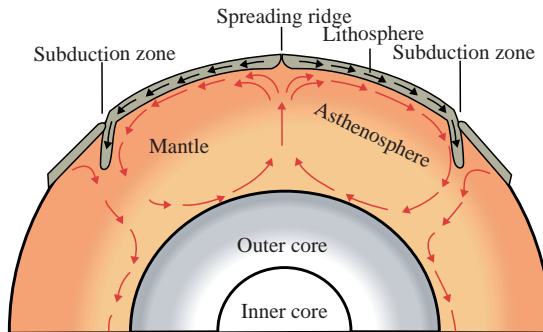


**Figure 4.3:** The parts of the earth with spreading ridges and subduction zones. After (Commons 2007).

If the movement of a plate is obstructed by the neighbouring plate, the friction energy will be saved up, in some cases for decades or even centuries, until the energy is released spasmodically as seismic deformation; an earthquake. The rupture plane is called a *fault*, and can in some cases be observed directly on the ground surface, especially in larger shallower earthquakes. (Dowrick 1987, p5) (Kramer 1996, p27)

## 4.2 Wave types

As the earthquake energy is released along the fault, it propagates through the soil as a number of waves, which have different characteristics. The nature of these waves are outlined in this section, which is based upon Andersen (2006, pp2-4). The four most commonly observed waves, P-waves, S-waves, R-waves, and L-waves are shortly presented.

The P-wave is denoted the *primary wave* since it is the first wave to arrive at an observation point. The particle motion is pure dilatation, or pressure. The P-wave is illustrated in Figure 4.4a.

The S-wave is denoted the *secondary wave* since it arrives after the P-wave, typically having a phase velocity of half the P-wave velocity. The particle motion for the S-wave happens as equivoluminal shear. The S-wave does not appear in a fluid, since no shear stress can be generated there. The S-wave is depicted in Figure 4.4b. A S-wave consists of two different components, the SV-wave and the SH-wave. The V and H abbreviates Vertical and Horizontal, and indicates the direction of the particle motion. The difference is illustrated in Figure 4.4b and Figure 4.5b. In the first of these subfigures the SV-wave is shown, whereas the latter shows the L-wave which acts like a SH-wave on the surface.

The P- and S-wave are jointly referred to as *body waves*, since they propagate through space. In opposition to this stands the *surface waves*, which count the R-wave (*Rayleigh wave*) and the L-wave (*Love wave*). These are depicted in Figure 4.5 on the following page. The Rayleigh wave moves the particles in ellipses just like ocean waves. How-

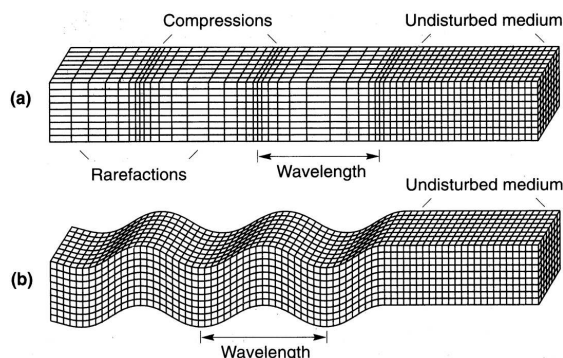


**Figure 4.4:** Deformation produced by body waves: (a) P-wave, and (b) SV-wave. The waves propagate from left towards right. (Kramer 1996, p19)

ever, the particle motion is retrograde near the surface, cf. Figure 4.5. Opposing to the P- and S-waves, the Rayleigh wave contains both pressure and shear components in the displacement field. The particle motion is greater in the vertical than in the horizontal direction, which is not clearly indicated in Figure 4.5.

The L-wave is, shortly explained, horizontally polarized shear waves (SH-waves) which are bound to the surface like the R-wave, thus creating horizontal horizontal movement of the earth during an earthquake.

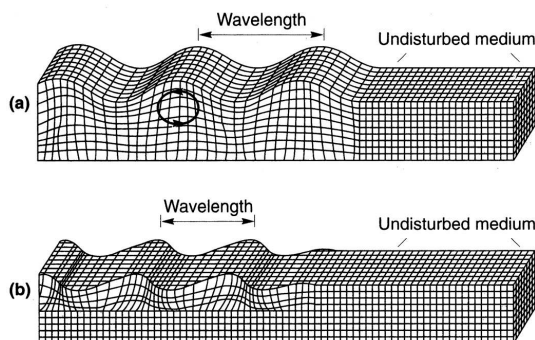


**Figure 4.5:** Deformation produced by surface waves: (a) Rayleigh wave, and (b) Love Wave. The waves propagate from left towards right. (Kramer 1996, p20)

### The present analyses

In a dynamic model, all the above stated types of waves should in principle be modelled and accounted for, as the earthquake motion propagates from the fault to the project site. In Figure 4.6 on the next page the propagation of the earthquake to the Thessaloniki tunnel is sketched. In the present thesis however, it has been chosen to focus only on SH-waves, to simplify the problem. It is deemed that the horizontal component of the ground motion is the more dangerous and this is mainly caused by S-waves, cf. Fardis *et al.* (2005, p21). Furthermore, it is stated by (Power *et al.* 1996) that S-waves are typically associated with peak particle accelerations and velocities, and the focus on SH-waves is widely used, *e.g.* by Anastasopoulos *et al.* (2007). Since

## Determination of design earthquake

the waves are refracted as they reach the surface due to decreasing soil stiffness, as it is sketched in Figure 4.6, the horizontal polarization is justified.

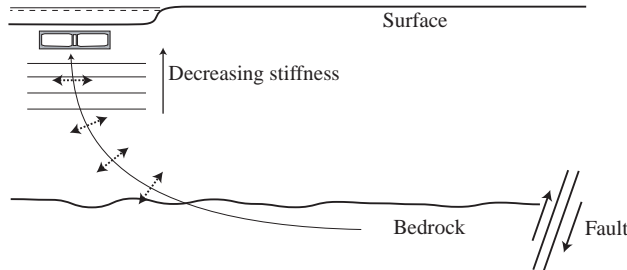


**Figure 4.6:** Propagation of the earthquake waves to the tunnel.

In Figure 4.6 it is sketched that the waves firstly propagate through the bedrock. This is valid since it is assumed that a significant distance exists between the fault and the project site. The damping in the alluvial soil is much greater than the damping in bedrock. Thus, all surface waves are disregarded, since it is assumed that they are damped away before reaching the project site. On the other hand, surface wave propagates two-dimensionally and body waves three-dimensionally, which makes geometrical damping more significant for body waves than for surface waves. Hence, geometrical damping and material damping are contradictory quantities, the impact of which should be analysed for a final design.

### 4.3 Determination of design earthquake

When determining the design earthquake many parameters must be evaluated, and many tools are at hand. In this section, some of these are presented.

This analysis is typical a job for skilled seismologists, but the final determination should be made in cooperation with the geotechnical and structural engineer, since the deformation mode of the structure may influence on what is characterized as the more dangerous earthquake motion.

#### 4.3.1 Size of earthquake

When categorizing earthquakes with a single parameter, the size of the earthquake is either characterized with the intensity or the magnitude.

##### Intensity

Intensity is a measure of the destructiveness of the earthquake, as evidenced by human reaction and observed damage. This is in other words a subjective measure, dependent on the eyes of the beholder. For historic earthquakes, this is the only measure available. Several scales are available, including the Modified Mercalli Scale (MM), the European Macroseismic Scale (EMS) and the Japan Meteorological Agency Scale (JMA).

Common for the scales is the representation of the intensity with Roman numerals. (PIANC 2001, pp129-130)

## Magnitude

Magnitude is an instrumental measure of the size of an earthquake. It is related directly to the energy released, which is independent of the place of observation. Again, several scales are available, based on the amplitude of seismograph records. The scales include the Richter local magnitude  $M_L$ , well known amongst laymen through the nine o'clock news. The moment magnitude  $M_W$  or surface magnitude  $M_S$  are, however, preferred by seismologists. The scales do not significantly differ for magnitudes up to 6. All magnitude scales have in common the representation of the magnitude with Arabic numerals. The maximum recorded magnitude is about  $M_W = 9.5$  (*e.g.* Chilean earthquake of 1960) (PIANC 2001, p130)

### 4.3.2 Seismic hazard analysis

To determine the design earthquake, a seismic hazard analysis can be carried out. The seismic hazards are the physical phenomena associated with an earthquake, which are likely to produce adverse effects on human activities. The hazards include *i.a.* ground failure and liquefaction, but mostly the ground motion is used as measure, since it is correlated to the other hazards.

Both deterministic and probabilistic seismic hazard analyses (DSHA and PSHA) can be performed. In the DSHA, the nearby potential earthquake sources are examined, and with the help of attenuation relationships or microzonation, the potential size of the earthquake at the project site is determined. The strongest earthquake is chosen, and a design to resist this earthquake is performed.

For a PSHA, all nearby seismic sources are incorporated in the design. The probabilistic distributions of each sources earthquake potential are incorporated, and a design is made based on a chosen reliability index  $\beta$ , *i.e.* the possibility that the design earthquake will be exceeded during a particular time period. For further references on seismic hazard analyses see, for example, (Kramer 1996, pp114-118).

## Liquefaction

Liquefaction is a most dangerous phenomenon, which is shortly outlined in the following. Under earthquake loading liquefaction can occur in areas with loose cohesionless soils. Also, liquefaction only occurs in saturated soil, and therefore is most commonly observed near rivers, bays and other bodies of water (Kramer 1996, p5). As the soil deposit is sheared back and forth, the pore water pressure may rise rapidly, even to the level of the total stresses, thus eliminating the effective stresses. If this occurs, the strength and the stiffness of the soil are lost altogether. In this condition large ground movements can occur. The liquefaction condition ends when the pore water overpressure has drained, thus restoring the effective stresses. In some cases a drain path

can evolve through the upper soil layers, spouting sand and water up as “volcanoes”. (PIANC 2001, p9)

The mechanisms of liquefaction are schematically shown in Figure 4.7. The damage mode of liquefaction has not been examined in the present thesis, since the subsoil in the project area does not contain any cohesionless soils, cf. Table 5.1 on page 28.

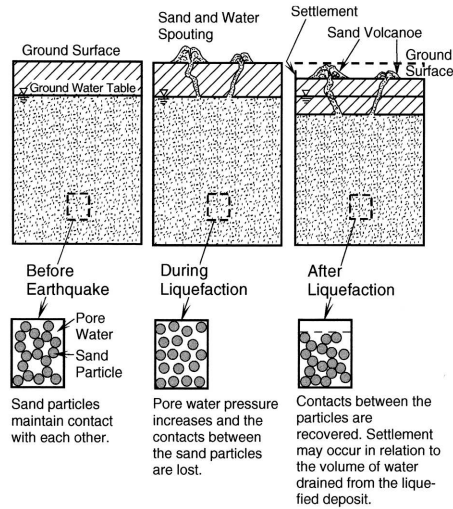


Figure 4.7: Mechanism of liquefaction. (PIANC 2001, p10)

### 4.3.3 Code spectra

Alternatively to seismic hazard analyses, the design earthquake can be determined with the use of a code. This is the most common approach to an aseismic design when dealing with ordinary structures *e.g.* like multi-storey buildings. Typically, the design seismic action will be given by a response spectrum, the shape and magnitude of which are altered according to the ground conditions and geographical region. Two examples of such code spectra are shown in Figure 4.8.

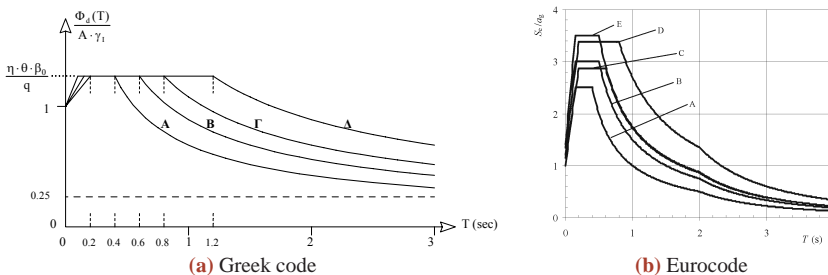
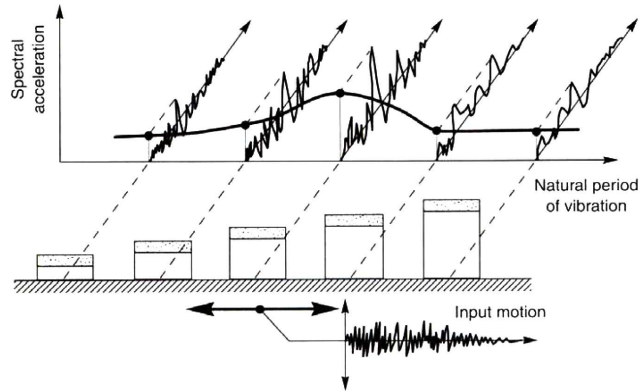


Figure 4.8: Examples of earthquake response spectra. The shown parameters are used to adjust the spectra to the local seismic conditions. (EAK 2000, p18) (EN 1998-1 2003, p25)

The calculation of a response spectrum is done with a single degree of freedom (SDOF) system, which is subjected to an earthquake. For each distinct frequency, the response

spectrum value is the maximal response for the SDOF system, which is tuned so that the eigenfrequency is the distinct frequency. The concept is illustrated in Figure 4.9, where the SDOFs with varying eigenfrequencies are shown between the input motion and the response spectrum.



**Figure 4.9:** The generation of a response spectrum. (Kramer 1996, p571)

Response spectra are directly applicable for the design of conventional buildings in the frequency domain, but time series are not directly provided from the spectra. To find appropriate time series, numerous time series must be analysed, and the time series with the best fit to the design response spectrum should be chosen. The motion amplitude can be scaled to make a better fit. In a design process, EN 1998-1 (2003) recommends the use of a minimum of three different time series recordings. In this thesis however, only a single time series has been used, since the application of more time series is trivial.

#### 4.3.4 The present thesis

In most cases the design earthquake is not for the structural or geotechnical consulting engineer to determine. Typically, the design earthquake is provided in the Special Conditions of Contract, *e.g.* in the form of a peak ground acceleration, velocity, and displacement, or as a response spectrum.

In the present thesis no analysis has been made to find an appropriate design earthquake, since the purpose of this thesis has been not to provide a design for the immersed tunnel but instead to evaluate the accuracy of the design models. In Section 5.5.1 the applied earthquake time series from the  $M_s = 6.2$  Aegion 1995 earthquake is presented. This has been chosen because it was at hand, and due to the geographical proximity of Thessaloniki and Aegion, shown in Figure 5.5 on page 33.

Further information on the detailed seismic environment of Thessaloniki is provided by *e.g.* Ptilakis *et al.* (2007) and Anastasiadis *et al.* (2001).

## 4.4 The influence of earthquakes on underground structures

For a structure placed above the ground surface, the most dangerous earthquake motion parameter is normally the acceleration on the surface. The acceleration is typically converted to an applied force using D'Alembert's principle, and the seismic design of the structure is verified (Nielsen 2004, p33).

Seismic design of underground structures is typically very different, since the inertia of the surrounding soil is large relative to the inertia of the structure. This means that the dominating parameter is the displacement in the surrounding soil. This has been verified by measurements made by Okamoto *et al.* (1973). Thus, the inertia of the underground structure itself becomes of minor importance. The focus in underground seismic design, therefore, is on the free-field deformation of the ground and its interaction with the structure, as recommended by (Hashash *et al.* 2001, p252).

## 4.5 Damage modes of tunnels

An immersed tunnel subjected to earthquake-induced strong ground motion will deform in a number of modes at the very same time. In Figure 4.10, the most significant of these modes are depicted. Figures 4.10a and 4.10b show compression in the axial and the cross axial direction, respectively. Figure 4.10c depicts bending of the tunnel, which can occur both horizontally and vertically, and Figure 4.10d shows shear deformation of the cross section, denoted as *racking*.

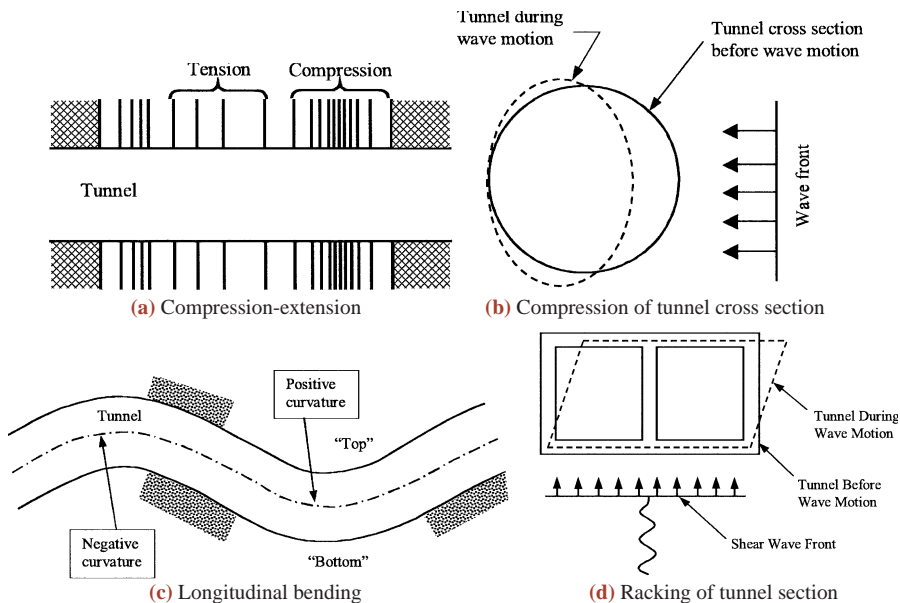


**Figure 4.10:** Deformation modes of tunnels due to seismic waves. After Owen & Scholl (1981).

For an immersed tunnel, the critical mode of earthquake induced vibration is the longitudinal oscillations, according to Anastasopoulos *et al.* (2007), since it may lead to

decompression of the joint gaskets. This will jeopardize the watertightness and, hence, the safety of the tunnel. Therefore, focus in this thesis is given to the longitudinal deformation of the gaskets, occurring mostly from mode (a) of Figure 4.10, but also from mode (c). Thus, potential deformation of the cross section of tunnel elements and gaskets is disregarded.

In Section 5.7 on page 38 it is discussed how damage to the tunnel is measured in this thesis.

## 4.6 Incoherence

For a structure such as a tunnel that extends over a considerable distance, different ground motions may occur beneath different parts of the structure. This local spatial variation of the ground motion is denoted *incoherence*, and it may exert a very important influence on the response of the structure (Kramer 1996, p100).

The incoherence can be caused by a number of factors, three of which are depicted in Figure 4.11. Figure 4.11a show the wave-passage effect, where an inclined wavefront causes the motion in locations 1, 2 and 3 to be shifted in time. Figure 4.11b show the extended source effect, where multiple faults generate earthquake waves which will reach the observation points at different times. Finally, the effect of soil heterogeneity is depicted in Figure 4.11c, where inhomogeneities in the soil cause reflection and refraction of the waves, thus altering the displacements in locations 1, 2 and 3.

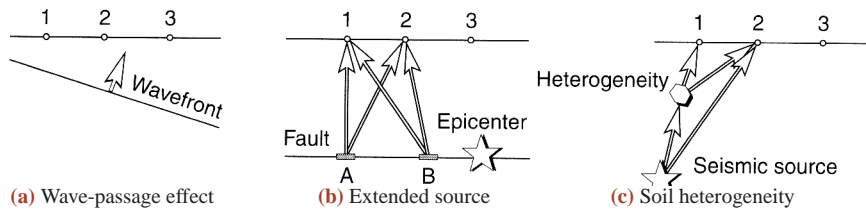


**Figure 4.11:** Incoherence. (Kramer 1996, p101)

In the present thesis, only the wave-passage effect is used as the cause of incoherence. While the two other effects could also have been incorporated without disproportionate costs, this is omitted to simplify the analyses.

The propagation velocity of the earthquake is in principle the velocity of the waves in the bedrock, stated in Table 5.2 on page 29. Since the three-dimensional wave propagation in the bedrock is not well accounted for, and since both the velocity of P- and S-waves will influence on the observed surface propagation velocity, it is chosen to use an *apparent velocity* which is based on empirical measurements. Typically, apparent wave passage velocities range between  $1000 \frac{\text{m}}{\text{s}}$  -  $2500 \frac{\text{m}}{\text{s}}$  according to Vrettos *et al.* (2007). The apparent velocity is further discussed in Section 5.5.2.

## DESIGN BASIS

This chapter encloses the basic informations about the projects required for the further analyses.

For the analyses, a lot of parameters have to be determined. These include *i.a.* the soil parameters, soil stratigraphy, earthquake parameters, as well as the physical geometry.

In a conventional static analysis, a characteristic value should be determined, *e.g.* as a five-percent quantile of the strength of a material. After application of *e.g.* partial safety factors, the provided design values should make sure that the design can be verified to be on the *safe side*. In a static analysis, it is mostly a trivial task to determine, whether or not a parameter is determined on the safe side. This, however, is not trivial in general for a dynamic analysis, and in particular for the analyses in the present thesis. It is *e.g.* not easy offhand to say, whether an increase in the shear stiffness in a soil layer will increase or decrease the displacement in the tunnel gaskets. This could *e.g.* depend on which eigenmodes of the tunnel are excited.

Hence, as it is not fruitful to determine characteristic and design values, in this chapter, best estimates of the “correct” mean value are searched for. Thereafter, in Part 3, the sensitivity of some of the parameters is analysed, *i.e.* it is analysed how the damage to the tunnel is affected by changes of a given parameter. This is done in order to examine whether the determination of a given parameter should be given great consideration, or if a reasonable estimate is sufficient for a final design.

### 5.1 Geometry of tunnel

The longitudinal section of the immersed tunnel is sketched in Figure 5.1. The immersed tunnel consists of eight tunnel elements, each approximately 153 m long (COWI 2007). The cross section is depicted in Figure 5.2 on the following page.

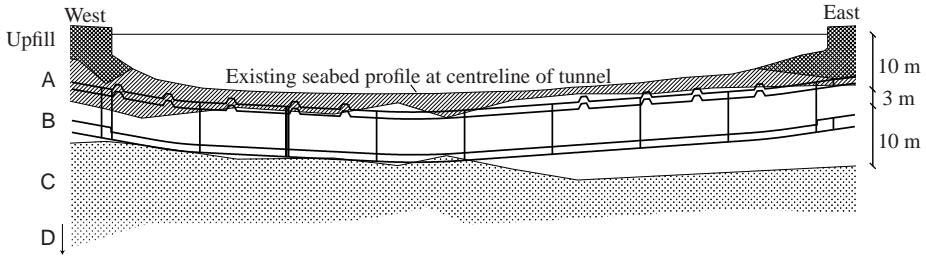


**Figure 5.1:** Longitudinal section of the tunnel. The letters indicate soil layers. After COWI (2007).

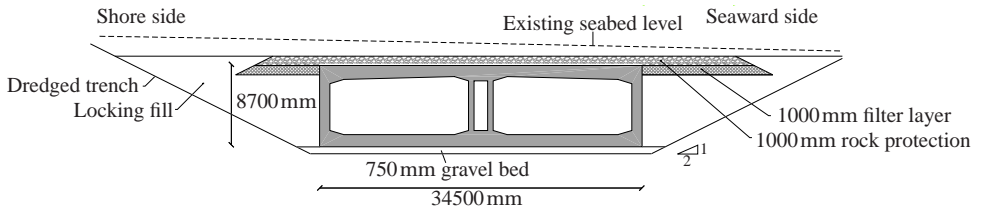


**Figure 5.2:** Typical cross section of the tunnel. After COWI (2007).

## 5.2 Geotechnical parameters

As indicated in Figure 5.1, the subsoil in the project area can be divided into four distinct layers. The fill layer is disregarded. In this section, the soil parameters associated with these layers are presented.

The four layers are listed in Table 5.1 together with the bulk weights. The thickness of the two topmost layers are indicated in Figure 5.1. The thickness of the red clay, layer C, is estimated to 100m to 150m. (COWI 2007)

**Table 5.1:** The layers of Figure 5.1. (COWI 2007)

Layer	Description	$\gamma \left[ \frac{\text{kN}}{\text{m}^3} \right]$
A	Loose sandy silty clay and silty clayey sand with occasional gravel	19
B	Medium dense silty clayey sand and firm sandy silty clay with some gravel	21
C	Firm red sandy silty clay with little gravel	21
D	Bedrock	-

In the microzonation report of Anastasiadis *et al.* (2001) dynamic soil parameters is presented. These include S- and P-wave velocities and quality factors for nine general soil layers present in the vicinity of Thessaloniki. The stratification and soil parameters are achieved as the result of a large-scale geophysical and geotechnical survey, where a detailed geotechnical map has been made. The geotechnical data comprised 440 boreholes with more than 4000 soil samples and 171 CPTs.

The correlation between the layers in the present interest and the layers of Anastasiadis *et al.* (2001) is presented in Table 5.2 on the facing page. The comparison has been made based on the geotechnical descriptions and bulk densities.

## Damping

**Table 5.2:** Quality factors  $Q_S$  and velocities  $c$  for P- and S-waves in the soil. The equivalent layer is the layer name cf. Anastasiadis *et al.* (2001). The values in brackets specify the expectation values. (Anastasiadis *et al.* 2001, p2620)

Layer	Equivalent layer	$c_S \left[ \frac{m}{s} \right]$	$c_P \left[ \frac{m}{s} \right]$	$Q_S [-]$
A	B2	200–300 (250)	1800	20-25 (20)
B	B1	300–400 (350)	1900	15-20 (20)
C	E	350–700 (600)	2000	6-30 (30)
D	G	1750–2200 (2000)	4500	180-200 (200)

### 5.3 Damping

In soil, energy is dissipated by various mechanisms. Due to their high complexity, these mechanisms can not be modelled explicitly. Therefore, some convenient mathematical formulation which lumps the various energy losses together – a damping mechanism – must be chosen. (Kramer 1996, p567) In this section, the damping mechanisms used in this project are outlined.

#### 5.3.1 Loss factor

A lot of different quantitative measures of damping exist. The relation between three common measures, the quality factor,  $Q$  (preferred by seismologists), the damping ratio,  $\xi$ , and the loss factor,  $\eta$ , are given as

$$Q = \frac{1}{2\xi}, \quad \eta = 2\xi \quad (5.1)$$

(Kramer 1996, p569).

In the following, the loss factor,  $\eta$ , will be used. For soil, the loss factor normally ranges between  $\eta = 0.03$  to  $\eta = 0.05$ . For the present project, the loss factors have been determined from the quality factors in Table 5.2, and are listed in Figure 5.4. For the tunnel, which is cast of concrete, a loss factor of  $\eta = 0.01$  is estimated. This is also assumed to correspond to the gaskets. The sensitivity of the loss factors are analysed in Section 11.4.1.

#### 5.3.2 Viscous damping

Viscous damping is commonly applied in structural dynamics, and models the behaviour of a dashpot. The damping is proportional to the velocity, as it can be seen in the equation of motion for a single-degree-of-freedom (SDOF) system, formulated in the time domain

$$k \cdot u + c \cdot \dot{u} + m \cdot \ddot{u} = f \quad (5.2)$$

where a dot ( $\dot{\phantom{x}}$ ) signifies differentiation with respect to time, and where  $k$ ,  $c$ ,  $m$ ,  $f$  and  $u$  are the stiffness, damping, and mass coefficients, the load, and the displacement, respectively.

In the frequency domain, it is assumed that the displacement is periodic. This entails that the displacement can be written as a linear combination of harmonic motions,

each of which can be expressed as  $u = e^{i\omega t}$ . Differentiation of this expression with respect to time,  $t$ , yields

$$u = e^{i\omega t}, \quad \dot{u} = i\omega e^{i\omega t} = i\omega u, \quad \ddot{u} = -\omega^2 e^{i\omega t} = -\omega^2 u \quad (5.3)$$

Insertion of these expressions into (5.2) provides

$$(k + i\omega c - \omega^2 m)u = f \quad (5.4)$$

which is the formulation of the equation of motion in the frequency domain. Now, it is chosen to let the damping coefficient be proportional by  $\beta$  to the stiffness coefficient

$$c = \beta k \quad (5.5)$$

This may be clear for a SDOF system, but it could also be applied for a multi-degree-of-freedom (MDOF) system, where the formulation is a special case of the Rayleigh damping method. Rayleigh damping entails that the damping matrix is written as a linear combination of both the stiffness and the mass matrices.

Now, (5.4) may be written as

$$(k(1 + i\omega\beta) - \omega^2 m)u = f \quad (5.6)$$

This leads to the definition of viscous damping as a modification of the stiffness

$$k_{\text{vis}}^*(\omega) = k(1 + i\omega\beta) \quad (5.7)$$

where the star (\*) indicates the modification to incorporate damping. This leaves the equation of motion to be

$$(k_{\text{vis}}^*(\omega) - \omega^2 m)u = f \quad (5.8)$$

Due to linearity, these equations, (5.7)-(5.8) can directly be formulated as matrix equations, to account for the modelling of a MDOF system.

### 5.3.3 Hysteretic damping

The hysteretic damping model is formulated with the loss factor.

$$k_{\text{hys}}^*(\omega) = k(1 + i\eta \text{sign}(\omega)) \quad (5.9)$$

(Andersen 2006, p54)

This damping formulation has been quite widespread in use, mainly due to the very simple formulation in the frequency domain. Hysteretic damping is frequency independent (only the sign function enters), which corresponds quite well to the behaviour of soil according to Andersen (2006, p54). Therefore, hysteretic damping is in general a better damping method for soil analysis than viscous damping.

It may, however, be shown that the hysteretic damping model is not causal, *i.e.* the use of hysteretic damping may imply that the response appears before the loading is applied. This effect is, however, insignificant for small loss factors, in the area of what is normal for soils.

### 5.3.4 Conversion

While the hysteretic damping, (5.9), is easily formulated and applied in the frequency domain, it can not be formulated in time domain; *i.e.* a formulation compatible with (5.2) can not be made.

Therefore, in this thesis, hysteretic damping will be used for the calculations in the frequency domain, while viscous damping is applied to the calculations in the time domain. Conversion between the two damping formulations should be performed in a way which yields the most equal output.

By comparison between (5.7) and (5.9), the relation is seen to be

$$k_{\text{hys}}^* = k_{\text{vis}}^* \Rightarrow i\eta \text{sign}(\omega) = i\omega\beta$$

$$\eta = |\omega|\beta \tag{5.10}$$

This equation, (5.10), entails that in order to correlate viscous and hysteretic damping, it is necessary to choose a frequency at which the damping will be equal. The frequency dependence of the two damping mechanisms are sketched in Figure 5.3a. The conversion frequency should be chosen as the dominant frequency of the system. The dominant frequency is in the present thesis chosen as the first damped eigenfrequency of the stratum,  $f = 1.09\text{ Hz}$ . In Figure 5.3b it can be seen that this frequency dominates the stratum response to the earthquake.

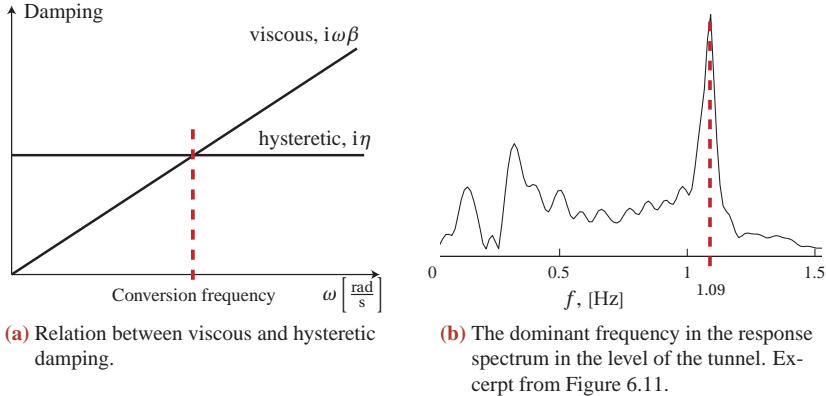


**Figure 5.3:** Viscous and hysteretic damping.

The relation between the circular frequency,  $\omega \left[ \frac{\text{rad}}{\text{s}} \right]$ , and the frequency,  $f \left[ \text{s}^{-1} \right]$ , both used in Figure 5.3, is

$$\omega = 2\pi f \tag{5.11}$$

In Section 11.4.2 it is shown, how the use of either viscous or hysteretic damping affects the soil response.

## 5.4 Design cross section

The actual geometry, as described in Section 5.1 and depicted in Figure 5.1, does not comply with the simple geometry needed for the domain transformation method de-

scribed in Section 6.2. Thus, a simplification is needed. The irregular layer interfaces have been reduced to horizontal interfaces located in some mean depth, rounded off to an integer value. Furthermore, the cross section at the middle of the tunnel is analysed, *i.e.* the water depth is around 10m. Finally, the dynamic parameters are taken as the mean values given in Table 5.2. The design section is shown in Figure 5.4.

These assumptions are deemed as realistic for a simple calculation in a real-world consulting firm. In Chapter 11 it is analysed how the simplifications may change the physics of the problem.

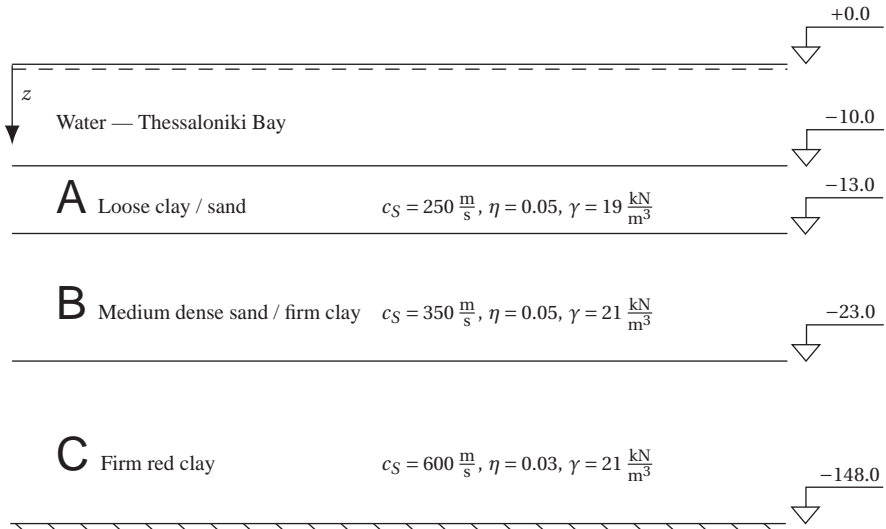


**Figure 5.4:** Sketch of design section for the domain transformation method. The bulk densities  $\gamma$  are stated in Table 5.1. The velocities  $c$  and loss factors  $\eta$  are based upon Table 5.2 on page 29. The loss factors are determined as the reciprocal value of the expectation value of the quality factors  $Q$  cf. (5.1) on page 29.

For many ground conditions, the stiffness of the soil – and thus also the shear wave velocity – will increase with the depth, cf. Anastasopoulos *et al.* (2007, p1070). This could probably also apply for layer C cf. Figure 5.4, but since the goal of the present thesis is to analyse the presented calculation models and not to provide a final design of the immersed tunnel, this is omitted for the sake of simplicity and transparency.

For the dynamic calculations of the soil response, the water level of Figure 5.4 has not been incorporated in the model, since it will not affect the dynamic behaviour of the soil.

The S-wave velocities in Figure 5.4 should be altered to incorporate damping in accordance with (A.2) and (A.4) on page 130. For layer A, with the gravitational acceleration set to  $g = 10 \frac{m}{s^2}$ , this is done as

$$\begin{aligned} \mu' &= c_S^2 \cdot \rho = 118.75 \text{ MPa} \\ \mu &= \mu' \cdot (1 + i \text{sign}(\omega) \eta) = (118.75 + 5.94i) \text{ MPa} \\ c_S^* &= \sqrt{\frac{\mu}{\rho}} = (250.1 + 6.2i) \frac{m}{s} \end{aligned} \tag{5.12}$$

where a star (\*) indicates that damping has been incorporated through the complex representation.

## 5.5 Input motion

In this section, the input motion corresponding to the bedrock is outlined. In Chapter 6 it is described how the response on the surface and at the level of the tunnel is calculated.

### 5.5.1 Time series

In Section 4.3 on page 21 the different methods of determining an appropriate design earthquake are outlined. However, in the present thesis a given time series is simply chosen, since the purpose of this thesis is not to provide a design for the immersed tunnel but instead to evaluate the accuracy of the design models. This generic approach has made a specific determination of the design earthquake outside the scope of this thesis.

An acceleration time series from the  $M_s = 6.2$  Aegion 1995 earthquake has been delivered by COWI (1995). This time series has been chosen because it was at hand, and due to the geographical proximity of Thessaloniki and Aegion, shown in Figure 5.5.



**Figure 5.5:** Location of Aegion.

The time series is the horizontal accelerations sampled at a rate of 100Hz in an outcropping bedrock. The acceleration time series is plotted in Figure 5.6 on the next page.

As described in Section 4.4, the important earthquake motion parameter for an underground structure is the displacements. These are easily obtained through double integration of Figure 5.6, and are plotted in Figure 5.7 on the following page. It may be seen that the displacement time series does not end at the starting displacement,  $u = 0$ . Thus, a permanent displacement has occurred. This is not compatible with frequency domain calculations, where the motion must be periodical. Therefore the displacement time series has been altered slightly, as it is indicated in Figure 5.7.

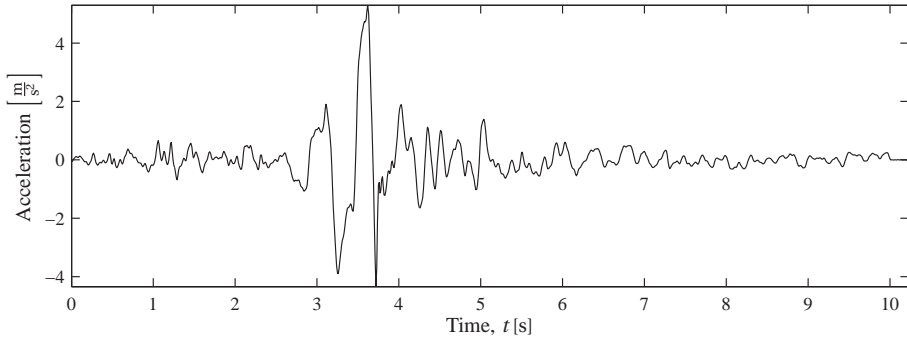


**Figure 5.6:** Acceleration time series. Measured earthquake record from the 1995 Aegion event.

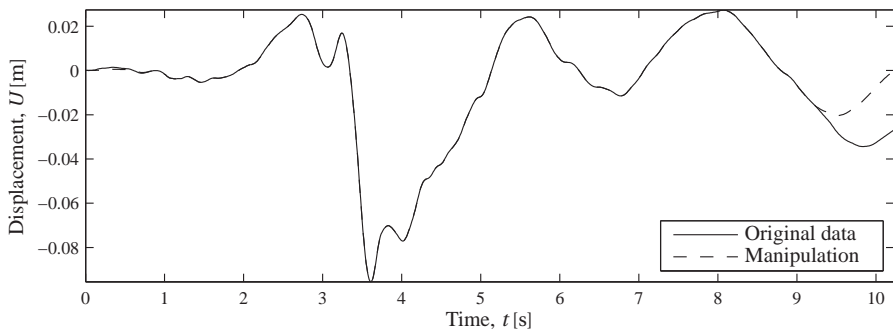


**Figure 5.7:** Displacement series from 1995 Aegion event. Obtained through double integration of Figure 5.6.

Some of the analyses in this thesis are performed in the frequency domain. With a Fourier transformation the displacement amplitude spectrum can be obtained from the time series, Figure 5.7. It is plotted in Figure 5.8.

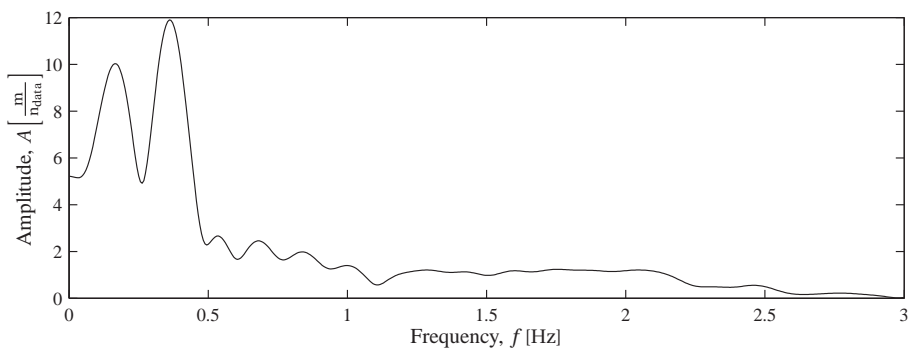


**Figure 5.8:** Single-sided displacement amplitude spectrum, obtained through Fourier transformation of Figure 5.7. To obtain a smoother spectrum and a periodic signal, the time series has been padded with additional zeroes, thus yielding a higher resolution of the Fourier transformation. This is further explained in Section 6.5.2.

## 5.5.2 Apparent velocity

As it is outlined in Section 4.6, the incoherence of the earthquake motion is of very significant importance for the imposed damage to the tunnel. The apparent velocity describes the velocity of the propagating wavefront, and typically fall in the range between  $1000 \frac{\text{m}}{\text{s}}$  -  $2500 \frac{\text{m}}{\text{s}}$ , cf. Section 4.6. For the analyses of the present thesis, the apparent propagation velocity is set to  $1500 \frac{\text{m}}{\text{s}}$ , since this is the choice of Vrettos *et al.* (2007), which precise deals with the Thessaloniki immersed tunnel. In Section 12.1 the consequences of this choice are analysed through a sensitivity analysis.

## 5.5.3 Direction of propagation

The wavefront is depicted in Figure 5.9. It propagates with the apparent velocity, and the direction of the propagation is defined with the angle  $\theta$ . Due to the great uncertainty associated with the determination of the design earthquake, including the direction of propagation,  $\theta$  should be chosen so that the tunnel damage is maximized.

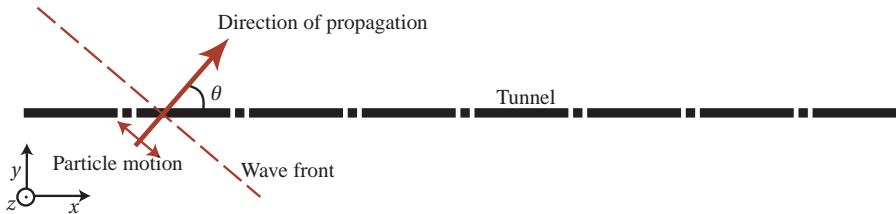


**Figure 5.9:** Definition of the direction angle  $\theta$ .

In the analyses in this thesis, as a point of reference the direction of propagation is set to  $\theta = 45^\circ$ . The reason for this is that an oblique direction contains both tunnel axial and cross axial particle motion, as it is illustrated in Figure 5.9. Thus, both compression/extension and longitudinal bending of the tunnel is excited, corresponding to Figure 4.10a and 4.10c on page 25.

In Section 12.2, the damage to the tunnel is calculated for other direction angles, thus showing the impact of the choice of angle.

## 5.6 Stiffness of gaskets

The gaskets joints, which couples the tunnel elements, exhibit highly non-linear behaviour when deformation in the axial as well in the cross axial direction are applied. In this section the behaviour is discussed, and linear approximations are made.

### 5.6.1 Longitudinal stiffness

In the present thesis, the Gina gasket profiles has been chosen to type ETS-180-220, which *i.a.* has been chosen for analysis for the Busan Geoje Fixed Link in South Korea (Daewoo 2004). In the longitudinal (axial) direction, the non-linear work curve of the gasket is shown in Figure 5.10. The behaviour of the gaskets during loading is of great

importance when analysing the system, since the watertightness of the entire structure is dependent on the compression of the gaskets.

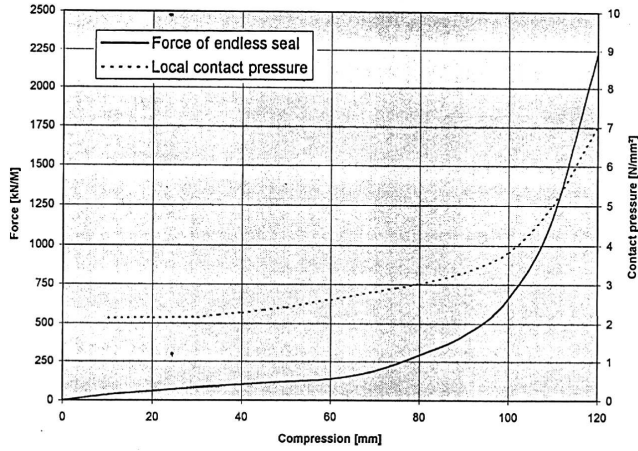


Figure 5.10: Force/compression graph for Gina gasket, type ETS-180-220. (Daewoo 2004)

### Initial compression

As described in Section 3.1, the Gina gaskets are compressed during the installation phase of the immersed tunnel elements. The initial compressive force on the gaskets is determined from the water depth of the tunnel centre, approximately  $d = 16\text{ m}$  cf. Section 5.1, and the area of the cross section,  $A_{\text{full}} = 300.2\text{ m}^2$  cf. Appendix D. This force is distributed on the total length of the circumference of the Gina gasket,  $L_{\text{gasket}} = 84.4\text{ m}$  cf. Appendix D, thus yielding a distributed force on the Gina gasket,  $F_{\text{init}}$ , of

$$\begin{aligned}
 F_{\text{init}} &= \frac{\gamma_{\text{water}} \cdot d \cdot A_{\text{full}}}{L_{\text{gasket}}} \\
 &= \frac{10 \frac{\text{kN}}{\text{m}^3} \cdot 16\text{ m} \cdot 300.2\text{ m}^2}{84.4\text{ m}} \\
 &= 569 \frac{\text{kN}}{\text{m}}
 \end{aligned} \tag{5.13}$$

The compressive strain can then be read off Figure 5.10 to approximately  $\epsilon_{\text{init}} = 96\text{ mm}$ .

### Linear approximation

Although the behaviour of the Gina gaskets is highly non-linear, a linear approximation is needed since the present thesis only applies linear analyses, cf. Section 1.3. A possible choice is to take the initial compression as the point of reference, and define the stiffness of the Gina profiles as the tangent stiffness in this point, as shown in Figure 5.11 on the next page. The change in the tangent stiffness, however, is relatively significant in this area. The consequences of the approximation are analysed in Section 13.1.

## Shear stiffness

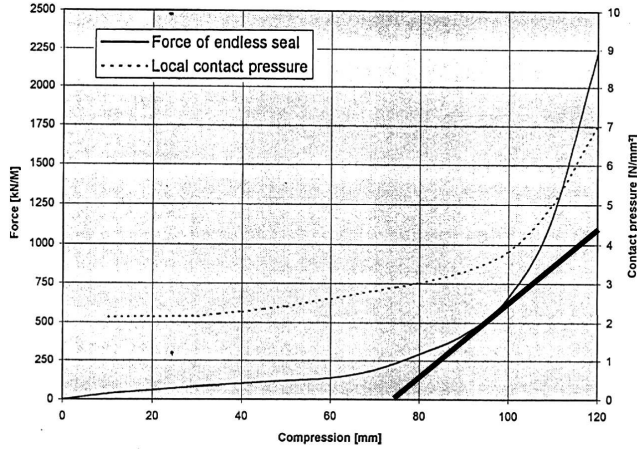


**Figure 5.11:** Figure 5.10 modified with a line with an inclination of 24MN/m<sup>2</sup>.

### 5.6.2 Shear stiffness

The shear stiffness of the gaskets is the resistance against transverse and vertical deformation for the coupling between two adjacent tunnel elements. Two different cases govern the shear behaviour of the gasket: for small shear displacements, the shear stiffness of the coupling stems from the shear stiffness of the Gina profile itself. For greater shear displacements, the stiffness of the coupling stems from shear keys of the tunnel.

#### Gasket rubber

The shear stiffness of a Gina profile itself depends on the compressive force on the gasket. The higher the compressive force, the higher the shear stiffness. This is *i.a.* due to the expansion of the gasket cross section when load is applied. (Tonnesen 2008)

A simple approximation of the shear stiffness can be obtained by assuming that the gasket is made of a homogeneous, isotropic and non-compressible material. This corresponds well to the behaviour of rubber. With these assumptions, the shear stiffness modulus,  $G$ , can be calculated based on a known Young's modulus  $E$  and Poisson's ratio  $\nu = 0.5$  with *e.g.* (A.2) to

$$G = \frac{E}{2(1 + \nu)} = \frac{E}{3} \quad (5.14)$$

#### Shear keys

If the shear displacements become sufficiently larger, *i.e.* of an order magnitude of approximately 5 mm (Tonnesen 2008), the shear keys of the tunnel elements become active. An illustrative sketch of these shear keys is provided in Figure 5.12 on the following page. It can be seen that the shear keys provide resistance to shearing when the shear allowance is exceeded, while still allowing deformations in the tunnel axial direction.

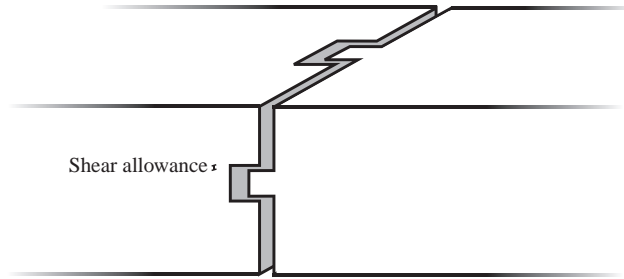


**Figure 5.12:** Shear keys.

The magnitude of the shear stiffness of the shear keys are deemed to be equal to the one of concrete. How many shear keys there will be in the final structure is unknown.

### Linear approximation

Due to the Gina profile and the shear keys, the resulting work curve of coupling between the two adjacent tunnel elements will look something like what is sketched in Figure 5.13.

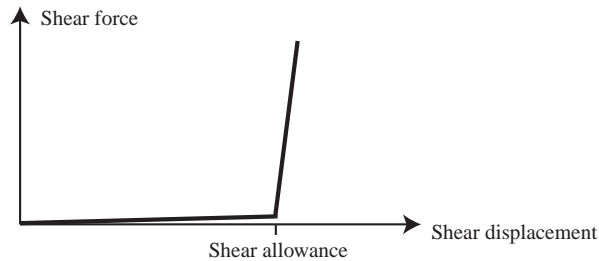


**Figure 5.13:** Work curve of Gina gasket under shear.

As it is easily seen, a linear approximation of Figure 5.13 can not be made with much degree of realism intact. Therefore, it is simply defined to use the first branch of the work curve as the stiffness in the general analyses, *i.e.* the shear stiffness of the gaskets are calculated from the shear stiffness of the profile itself, from (5.14). In Chapter 13 it is shown that the choice of gasket shear stiffness has very little influence on the final output of the models.

## 5.7 Damage criterion

The goal of the present analyses is to determine to which extent the immersed tunnel suffers damage from the strong ground motion generated by the earthquake. To measure this damage several damage modes can be observed, as described in Section 4.5.

It is deemed that the earthquake most potentially will damage the joints between the tunnel elements, as it is stated by Anastasopoulos *et al.* (2007). Thus, the main focus of this report will be on the damage mode where the gaskets loses the initial

compressive strain, hereby endangering the watertightness of the tunnel. This loss of compression is generated by relative displacement of two adjacent tunnel elements, as sketched in Figure 5.14. If the initial compression of the gaskets, 96mm according to Section 5.6.1 on page 35, diminishes towards zero, the watertightness of the structure is lost.

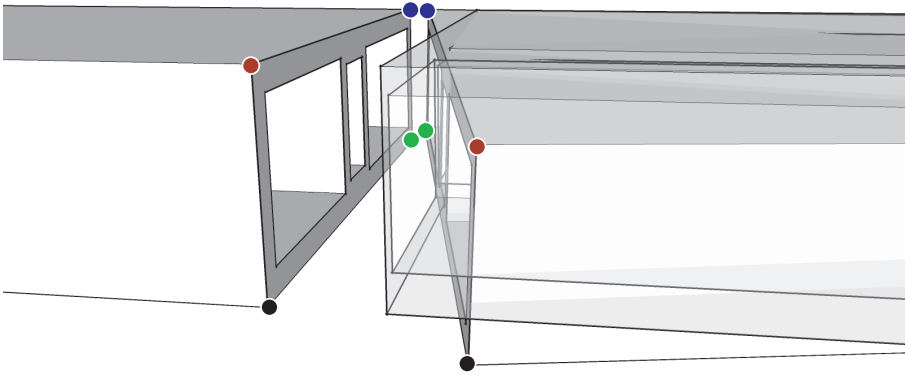


**Figure 5.14:** Sketch of two tunnel element ends. For the right tunnel element, the deformed and undeformed (transparent) states are shown, with a considerable (exaggerated) relative displacement and rotation. The Gina gasket is not shown. The colors indicate which corners that are related, when calculating the gasket damage.

The deformation of the gaskets is, in the Winkler model and the continuum model, calculated in the four corners of each gasket, since the maximum and minimum displacement will be in the corners. These corners are depicted in Figure 5.14. Damage to a gasket is defined as the absolute distance between two matching corners. As a consequence of this definition of damage, other deformation modes, *e.g.* racking deformation cf. Figure 4.10d, shear displacement of a gasket or tensile stresses in the tunnel concrete, may not be analysed.

If the final design should show too much opening in the gaskets the design should be altered. This could *e.g.* include a different gasket type, longitudinal displacement keys or division of the tunnel into more elements. This would allow more deformation, limit the deformation or distribute the deformation, respectively.



PART II

**METHODS OF ANALYSES**



## WAVE PROPAGATION THROUGH SOIL

The input to the analysis of the immersed tunnel is a time series of strong ground motion at different levels of the subsoil. As it is described in Section 5.5.1, the displacement time series from the earthquake records applies only to the level of the bedrock. In this chapter, it is outlined how the time-varying displacements can be calculated above the bedrock, including in the level at the tunnel and on the surface.

The steps of the calculation are illustrated in Figure 6.1. The transformation of the earthquake motion is performed in the frequency domain, and the transformation between the time and the frequency domain is obtained with Fourier transformations. The more demanding part of the calculation is to establish the frequency response function,  $H(\omega)$ , which couples the input and output spectra.

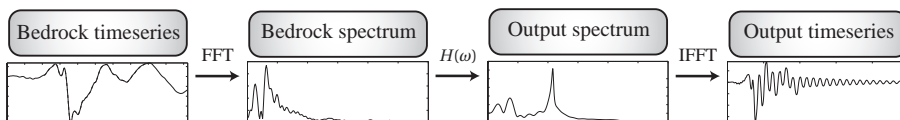


**Figure 6.1:** The calculation procedure from a time series at bedrock to an output time series at a chosen level. FFT stands for Fourier transformation with the Fast Fourier Transformation algorithm, and IFFT stands consequently for the Inverse FFT algorithm.  $H(\omega)$  is the frequency response function.

In the present chapter, firstly, a generalized version of a geometry is given. The geometry is limited to a *stratum*, a horizontally layered soil. The geometry, and thus also the computation, is entirely one-dimensional; the only dimension regarded being the depth. Subsequently, two methods are presented: the semi-analytical *Domain Transformation Method* (DTM) and an application of the *Finite Element Method* (FEM).

The calculations in the frequency domain are performed by calculating the response for many discrete frequencies, and constructing the frequency response function by

use of the principle of superposition. This entails that only linear material models can be used, as it is also discussed in Section 1.3.

## 6.1 Generalized geometry

A soil, modelled as a stratum, subjected to a forced horizontal displacement at bedrock level is analysed. Only vertically propagating SH-waves are modelled, as it is discussed in Section 4.2.

A stratum with  $J$  soil layers is examined. A cartesian system of coordinates are inserted in the top of the stratum, and below the stratum bedrock is modelled as a rigid interface. A definition sketch of the observed domain is shown in Figure 6.2.

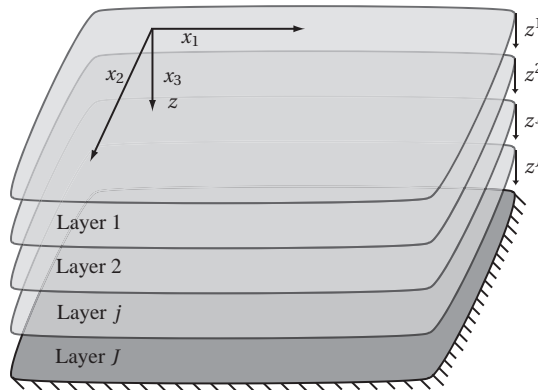


**Figure 6.2:** General geometry used for the domain transformation and the finite element methods. The planes illustrate the interfaces which separate the soil layers.

The reduction of a real, three-dimensional geometry to a one-dimensional stratum provides access to a very simple way of calculating the response, in means of the DTM, which analytical calculates the response; the only numerics involved are the discretization of the frequency range. If two- or three-dimensional wave propagation were to be taken into consideration, only numerical methods should be considered.

### Constitutive model

The soil layers are modelled as homogeneous, isotropic, linear viscoelastic materials. The reasons for this are as follows:

- **Homogeneity**

Inside one layer the assumption of homogeneity should be evaluated on the basis of the dimensions of the soil particles and the wavelength of the wave. Since the wavelength is considered to be several orders of magnitude larger than the particles, homogeneity is justified.

- **Isotropy**

In reality most alluvial soils will display slight orthotropic behaviour, but since no detailed data are available (and most rarely are) the assumption of isotropy is adopted. This will have no effect in the present case, since only a vertically

propagating SH-wave is analysed, which entails that the only stiffness parameter of importance is the horizontal shear stiffness.

- **Linear viscoelasticity**

Soil is in general a non-linear elasto-plastic material, but linear elasticity is adopted since the non-linear case presents too large a computational workload. In the most cases, the relatively small strains induced by the earthquake makes the linearization acceptable. According to Krätzig & Niemann (1996), soil subjected to shear strains up to  $\gamma = 10^{-4}$  may be analysed as a viscoelastic material.

The prefix *visco-* indicates that damping is applied to the material model. Various damping mechanisms are discussed in Section 5.3, according to which the applied damping mechanism for the present analyses should be hysteretic damping, since the analyses are carried out in the frequency domain.

## 6.2 The domain transformation method

In Appendix A, the DTM is derived. The method establishes a direct analytical relation between the harmonic varying displacement at bedrock and an arbitrary other layer at a certain frequency, expressed in (A.22) as

$$U_n^{j0} = H_n^{j0}(\omega) \cdot \bar{U}_n \tag{6.1}$$

where  $U_n^{j0}$  and  $\bar{U}_n$  are the displacements in the  $j$ 'th layer and the bedrock, respectively, while  $H_n^{j0}(\omega)$  is the frequency dependent response function for the  $j$ 'th layer. The calculated frequency response function is exact for the chosen material model and soil geometry.

With the DTM, the geometry given in Figure 5.4 on page 32 is elaborated. For frequencies ranging from 0–20Hz, the frequency response function is depicted in Figure 6.3. It can be observed that significant amplification, e.g.  $H(1.09\text{Hz}) = 43$ , is occurring at several damped eigenmodes.

It should be noted that the frequency response function is a complex number which includes both the magnitude and the phase shift of the response. Hence, what is plotted on the ordinate axis in Figure 6.3 is the amplitude of the frequency response function.

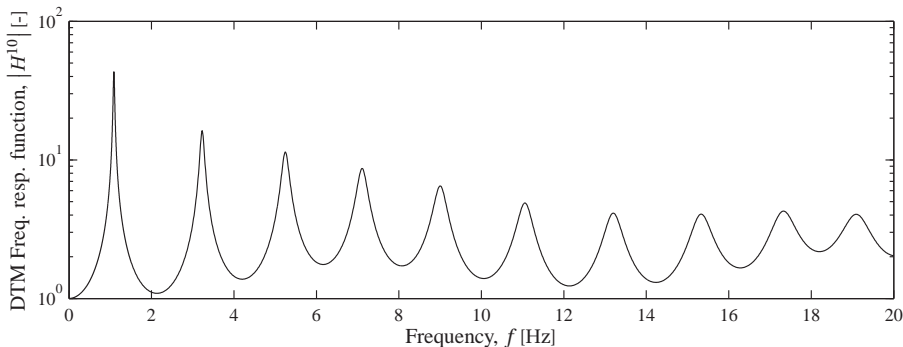


**Figure 6.3:** The amplitude of the frequency response function  $H^{10}$  for the top of the topmost layer, calculated with the DTM. The geometry follows from Figure 5.4.

### 6.3 The finite element method

As a verification of the applicability of the DTM, a finite element approach is made to the same problem. The method is derived in Appendix B. In stead of a direct analytical relation between the displacements in a chosen layer interface and the bedrock, as in the DTM, the stratum is now discretized into a number of soil elements, as it is sketched in Figure 6.4.

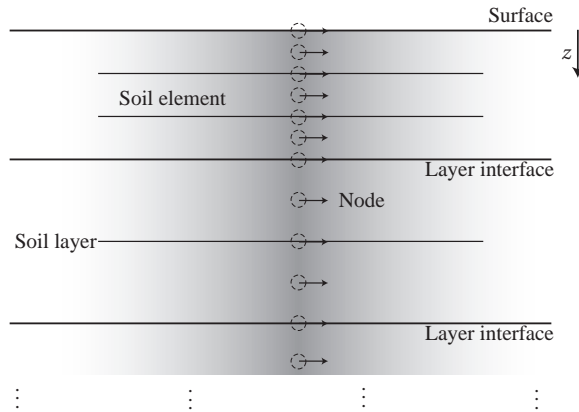


**Figure 6.4:** The finite element method.

#### 6.3.1 Elements

It is chosen to use second-order elements for the analysis, *i.e.* elements whose deformations are described by a second-order polynomial. Second-order elements will provide a much better approximation to soil deformation due to a propagating wave, than will linear elements. As discussed by Semblat & Broist (2000), much greater accuracy may be obtained at a lower computational cost. The shape functions of a second-order soil element are depicted in Figure 6.5.

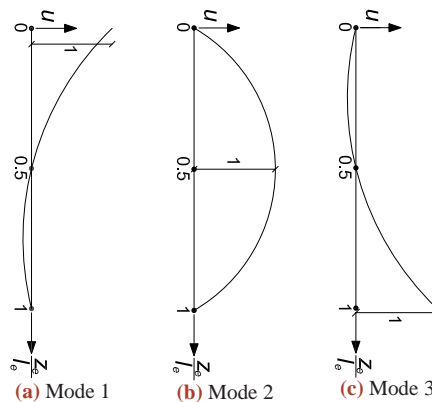


**Figure 6.5:** Shape functions for a second-order soil element. (Jensen & Jørgensen 2006)

### 6.3.2 Frequency response

In Figure 6.6 the frequency response function is plotted for the same frequency range as Figure 6.3 on page 45. It can be seen that the two methods are capable of producing very similar output from the same input; only a minor divergence can be observed around  $f = 20$  Hz. This is considered as a verification of the calculation methods.

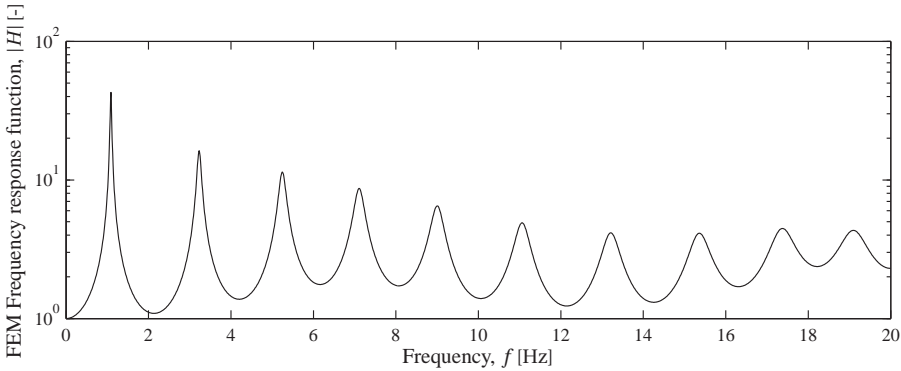


**Figure 6.6:** The amplitude of the frequency response function  $H$  for the top of the topmost layer, calculated with the FEM, with 10 elements in each soil layer. The geometry follows from Figure 5.4.

### 6.3.3 Convergence

The frequency response function depicted in Figure 6.6 has been calculated with 10 elements in each soil layer, *i.e.* a total of 30 elements. While the domain transformation method is exact for each frequency, the accuracy of the finite element method depends on the discretization of the domain.

The convergence of the finite element method is plotted in Figure 6.7 for six chosen frequencies. It can be observed that the number of elements needed to obtain convergence raises together with the frequency. The reason for this should be obvious, since complexity of the soil deformation profile also raises together with the frequency, and thus, more elements are needed to reproduce the deformation mode.

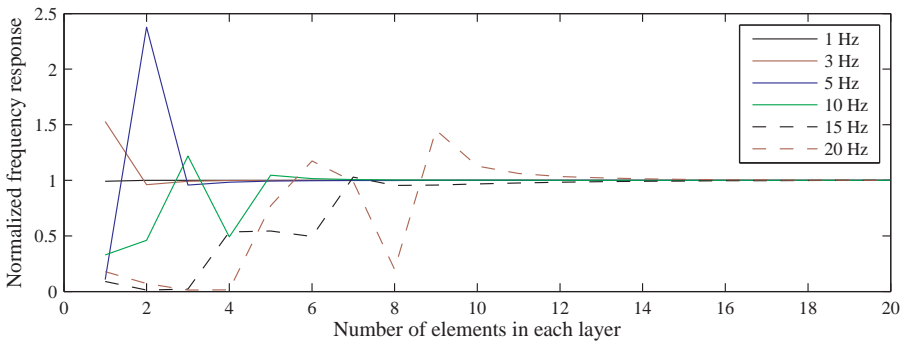


**Figure 6.7:** Convergence of the frequency response for the finite element method.

In Figure 6.7, it can further be seen that with a discretization of around 15 elements per layer, the response to displacements forced at 20Hz can be accurately calculated. This relatively small number of elements needed, is due to the use of second-order elements, which are able to reproduce the sinus-like soil deformation, cf. Figure 6.9a, well.

### 6.3.4 Choice of calculation method

As explained in the present and the preceding section, the DTM and FEM yields comparable results. The domain transformation method, however, is much more computational efficient, since no excess discretization of the domain is needed. Therefore, the domain transformation method will be used henceforward in this thesis.

## 6.4 Frequency response

The frequency response function varies down through the stratum. For the top of the layers the functions are plotted in Figure 6.8.

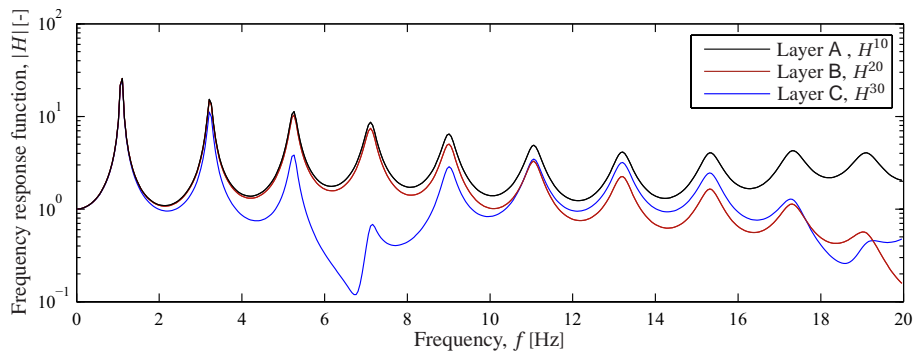


**Figure 6.8:** The frequency response function  $H$  for the top of the three layers in Figure 5.4. The black line is identical to Figure 6.3.

Most noteworthy in Figure 6.8 is probably the suppression of the response for the top of layer C between frequencies from 6 to 9Hz. In this region the mode of the soil makes the interface between layer B and C experience very little displacement, *i.e.* a node is formed. In Figure 6.9 on the next page the response at two time steps is plotted for three frequencies, and it can be seen that for a frequency of  $f = 6.7$  Hz, there is very little response at the interface between layer B and C. Hence, what offhand could look like a possible computational error, here does has physical meaning.

## Earthquake response

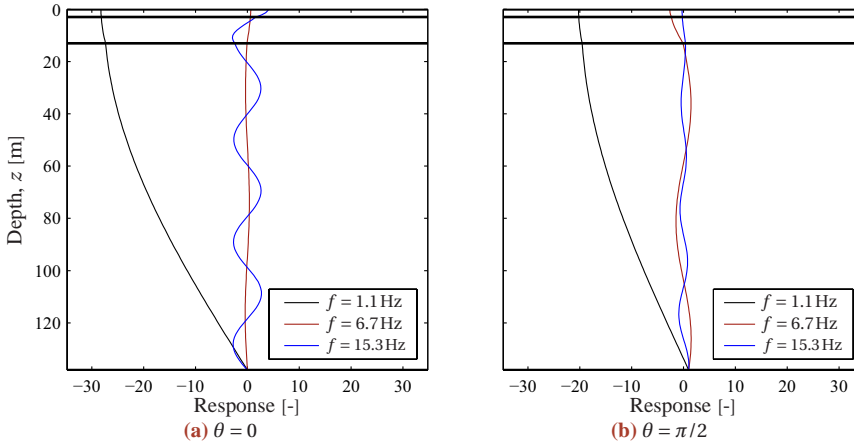


**Figure 6.9:** Response through soil for three frequencies. The harmonic motion is generated by a sine function, dependent on the amplitude and phase shift of the motion. Hence, the response at bedrock,  $z = 138\text{m}$ , in (a) is  $A \cdot \sin(\theta + \psi) = 1 \cdot \sin(0) = 0$ . The horizontal lines illustrate the layer interfaces. An animated version of the figure is provided on the attached DVD.

## 6.5 Earthquake response

The frequency response function, however, is only interesting when compared to the strong ground motion generated by an earthquake. Figure 6.10 gathers the earthquake ground motion spectrum and the frequency response function from Figure 5.8 and Figure 6.3, respectively. It can be seen that the first eigenmode of the stratum is located outside the dominant frequencies of the earthquake displacement spectrum. This indicates that only relatively little resonance will occur in the stratum.

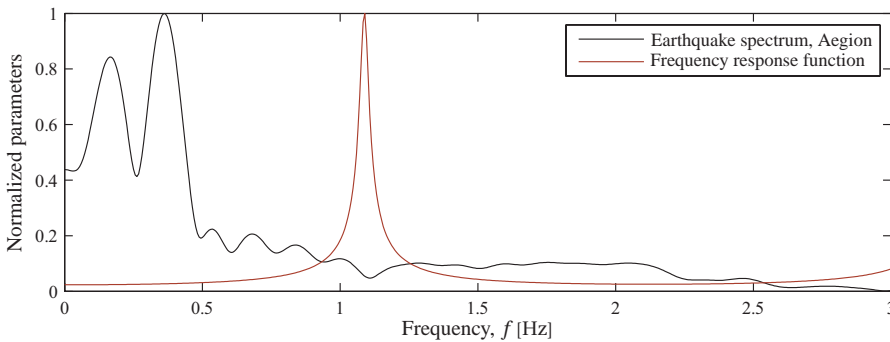


**Figure 6.10:** Comparison between the graphs of Figure 5.8 and Figure 6.3. The graphs have been normalized with respect to the maximum value.

### 6.5.1 Frequency domain

The order of the calculation follows from Figure 6.1 on page 43. The response of the soil to the earthquake motion is calculated in the frequency domain according to (6.1). The resulting output spectrum is depicted in Figure 6.11 on the following page,

together with the similar spectrum for the mean tunnel level, at 4.85 m depth. It can be seen that there are no significant differences on the spectra.

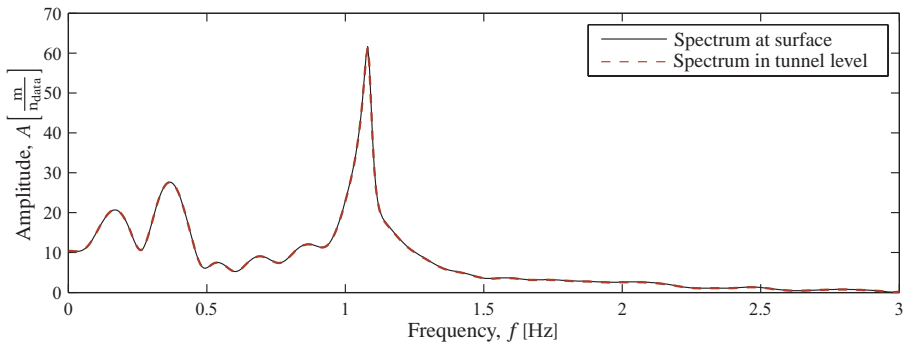


**Figure 6.11:** Response spectra. The spectrum for the surface is obtained through multiplication of the two graphs of Figure 6.10.

## 6.5.2 Time domain

Through an inverse Fourier transformation the response in the time domain can be calculated, cf. Figure 6.1. This is depicted in Figure 6.12. As in Figure 6.11, it can be seen that there is no significant difference on the response at the surface and at the level of the tunnel.

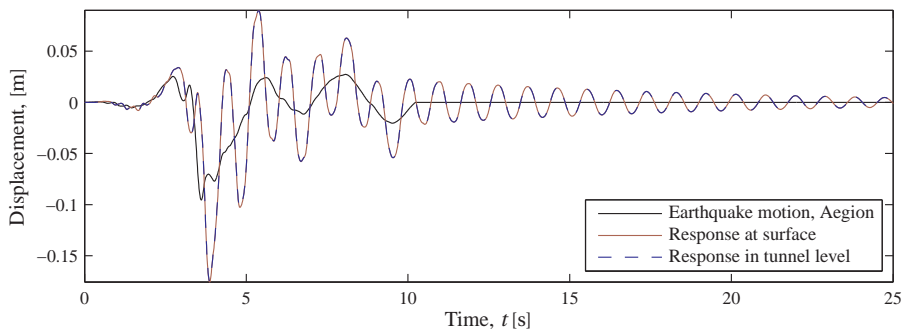


**Figure 6.12:** Strong ground motion and response in upper layer in time domain. The tunnel level is at 4.85 m depth.

It should be noted that even though the analysis of the wave propagation has been carried out in the frequency domain, it yields a result in the time domain which looks very physical plausible. This could to some be a little surprising, since the underlying assumption for a frequency-domain analysis is that the motion is periodically – something which definitely is not fulfilled in the present case, as can clearly be seen in Figure 6.12.

To obtain a reasonable level of accuracy, it is necessary to pad the original time series with zeroes, as it is shown in Figure 6.13b. This imitates a periodic motion, which could be be illustrated as in Figure 6.13c.

### Time domain

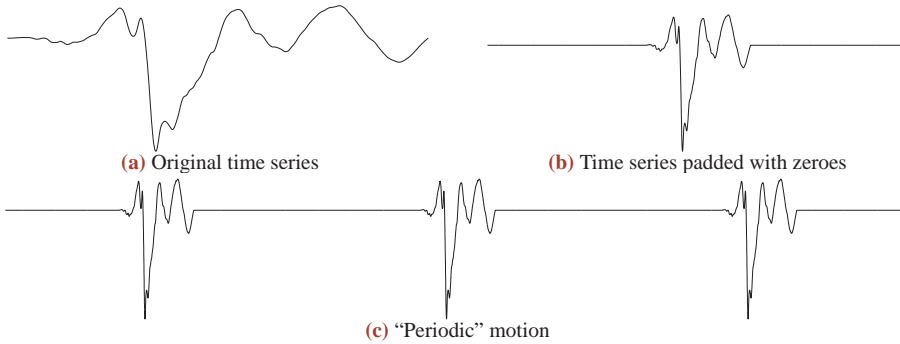


**Figure 6.13:** Padding of the time signal with zeroes before the Fourier Transformation to obtain a “periodic” motion.

Four time series with different amount of padding are plotted in Figure 6.14, from which the necessity of the padding should be obviously. If an insufficient size of padding is used, it can be observed that the output time series will take values different from zero, *before* the input time series begins, as it is clearly seen in Figure 6.14b. Furthermore, if no padding is applied (Figure 6.14a), it is not possible to calculate the response after the earthquake time series has ended, because no more information is available. In the further analyses, a padding of 150s has been applied, which yields the output of Figure 6.12.

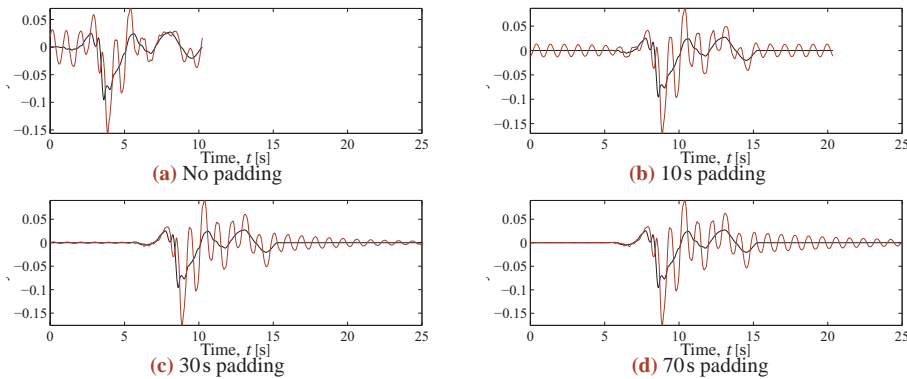


**Figure 6.14:** The effect on the output time series of different paddings. The black line is the input time series, the red line is the output time series.



## CLOSED FORM SOLUTION

As a first-order estimate of the deformation of the tunnel, a simple, closed-form solution is adopted. The great advantage of the closed-form solution is the minimal input. This makes it very easy to obtain an estimate on the order of magnitude of the structure's anticipated deformation. This can be used for initial design considerations as well as for design verification.

The closed form solution assumes that the deformation of the tunnel is equal to the so-called *free-field* deformation. Free-field deformations are the ground strains caused by the earthquake, when the tunnel is disregarded, *i.e.* all soil-structure interaction is ignored. Whether the tunnel deformation is over- or underestimated depends on the stiffness of the tunnel relative to the stiffness of the soil. (Hashash *et al.* 2001, p262)

The free wave field is assumed to consist of the same amplitudes at all locations, differing only with a time shift. The input motion is not a time series, but only the maximal acceleration and velocity of the earthquake. This should be calculated at the level of the tunnel, cf. Chapter 6.

### 7.1 Axial strain

It may be shown that the axial strain,  $\varepsilon_{\text{axial}}$ , due to a propagating S-wave with apparent velocity  $C_S$ , may, as stated by Power *et al.* (1996), be calculated as

$$\varepsilon_{\text{axial}} = \frac{v_S}{C_S} \sin \phi \cos \phi + r \frac{a_S}{C_S^2} \cos^3 \phi \quad (7.1)$$

where  $v_S$  and  $a_S$  are the peak particle velocity and acceleration, respectively,  $r$  is the half width of the tunnel and  $\phi$  is the angle of incidence of the wave with respect to the tunnel axis.

(7.1) is derived from the normal strain and the curvature of the free-field deformation, given in Hashash *et al.* (2001, 264). These are combined with simple beam theory to obtain (7.1). The first term in (7.1) represents the peak axial strain due to soil strain in the axial direction, while the second term is the axial strains due to bending of the tunnel.

## 7.2 Deformation at gaskets

While the axial strain computed by (7.1) assumes a uniform tunnel cross section, the real tunnel consists of elements connected by gaskets. As a crude approximation it is assumed that the computed axial strain occurs simultaneously over an entire beam element. Furthermore, the tunnel is assumed to be infinitely stiff, which should be fair when the tunnel is compared to the gaskets. This means that the strain over an entire beam element can be lumped in the gaskets. Thus, the maximal axial deformation at a gasket,  $\Delta u$ , can be calculated from the element length  $l_e = 153 \text{ m}$

$$\Delta u = \varepsilon_{\text{axial}} \cdot l_e \quad (7.2)$$

## 7.3 Input

The peak particle velocity and acceleration enters in (7.1), and should be calculated in the level of the tunnel. The conversion from displacements to velocities and accelerations is performed in the frequency domain, since a double differentiation of a discrete time series in the time domain will generate much numerical noise, so that the output will be contaminated severely.

Since the motion is assumed to be periodical, differentiation in the time domain is simply performed by multiplying the signal with  $i\omega$ , *i.e.* double differentiation is obtained by multiplication with  $-\omega^2$ . This is similar to the calculations performed in Section 5.3.2 on page 29. The displacement spectrum at the level of the tunnel is depicted in Figure 6.11 on page 50.

The time series for the velocity is plotted in Figure 7.1, and the time series for the acceleration is plotted in Figure 7.2.

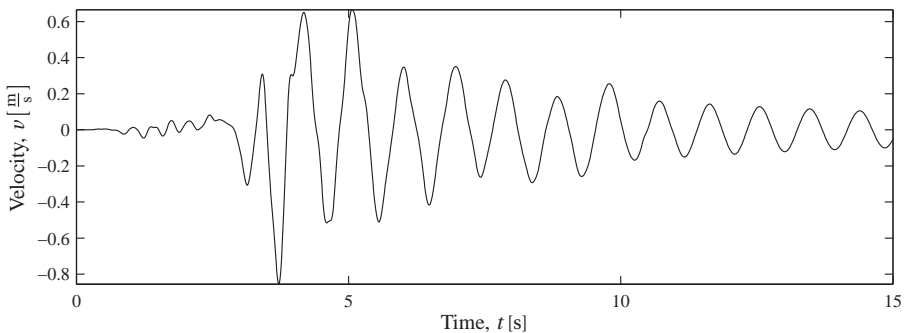


**Figure 7.1:** Velocity time series for the tunnel level.  $v_{\min} = -0.86 \frac{\text{m}}{\text{s}}$ ,  $v_{\max} = 0.67 \frac{\text{m}}{\text{s}}$ .

## Input

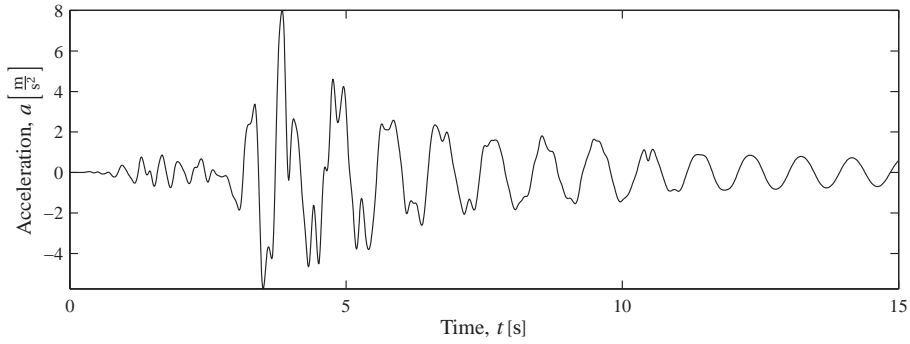


**Figure 7.2:** Acceleration time series for the tunnel level.  $a_{\min} = -5.74 \frac{m}{s^2}$ ,  $a_{\max} = 8.01 \frac{m}{s^2}$ .

The results from the closed form solution are calculated together with the results from the Winkler model and the continuum model in Chapter 10.



## WINKLER MODEL

A widely used model, when analysing immersed tunnels subjected to earthquake loading, is the Winkler model. This is used *e.g.* by Vrettos *et al.* (2007) and Anastasopoulos *et al.* (2007), and has been used for the design of several immersed tunnels (Kiyomiya 1995, p469).

In the Winkler spring model, the soil is represented with independent springs interacting with the tunnel which is considered as a beam (Dowrick 1987, p243). This is illustrated in Figure 8.1, where the longitudinal, transverse and vertical springs are shown. The Winkler model has been implemented in a Finite Element program coded in MATLAB .

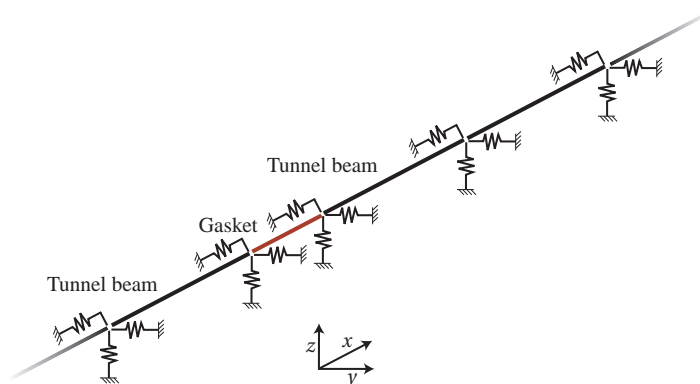


**Figure 8.1:** Sketch of the Winkler model. A gasket (red line) is shown in greater detail in Figure 8.11.

In the present application of the Winkler model, the tunnel elements are modelled with beam finite elements with appropriate cross-sectional parameters, while the Gina gaskets are modelled with multiple springs. The modelling and behaviour of the gaskets

are discussed further in Chapter 13.

The present application of a Winkler foundation for the beam has been performed with simple spring finite elements. This entails that the distribution of the springs is discretized to a finite number, according to the degrees of freedom for the tunnel beams. It is also possible to formulate special finite elements which model a continuum distribution of springs. The discretized and continuous foundations are illustrated in Figure 8.2.



**Figure 8.2:** Winkler foundation.

The simple discrete soil spring distribution has been chosen since it is deemed that with an appropriate discretization, the simple modelling will be sufficiently accurate. The internal stress in the tunnel beam will be affected by the discretization, but the stresses are unimportant for the present analysis. The need for an appropriate discretization can be realised by a study of Figure 8.3, where it can be seen that the discretization should be determined with respect to the frequency and the propagation velocity of the earthquake. Convergence analyses have been carried out in Section 8.2.4 to ensure a sufficient discretization.

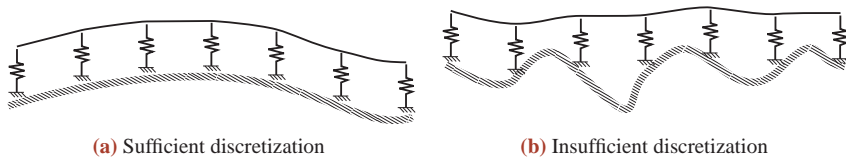


**Figure 8.3:** The Winkler model with discretized soil springs, subjected to (a) low frequency motion and (b) high frequency motion. The hatched lines at the bottom are the input displacement field.

## 8.1 Model assumptions

The Winkler model is by no means an exact representation of the physical problem. Amongst the assumptions made are:

- The springs on the tunnel are totally decoupled, *i.e.* no retroaction is possible.
- The deformation of the tunnel is limited to that of a Bernoulli-Euler Beam, *i.e.* no shear deformation is possible.
- The gaskets are approximated with linear springs.
- The propagation of the waves from bedrock to the tunnel is assumed to be one-dimensional.

These assumptions will be analysed through this report by means of a continuum model, which is described in Chapter 9.

Furthermore, both the Winkler and the continuum model is restricted to some general assumptions which are:

- The analysis is entirely linear, as it is discussed in Section 1.3.
  - The material models are all linear elastic
  - The possible development of a gap between the soil and the tunnel is not analysed.
  - The stiffness's of the Gina gaskets are assumed to be linear.
- The influence of the pre-stressing of the tunnel, discussed in Section 10.4, is neglected.

## 8.2 Modelling

The model has been coded in MATLAB on the basis of an existing linear FE program for static analysis, by Stærdahl *et al.* (2007). The program has been enhanced with new finite elements and with the ability to perform dynamic calculations. The changes in the program are described in Appendix C. The program files are enclosed on the attached DVD. In Figure 8.4 a screen dump of the simple output interface is shown.

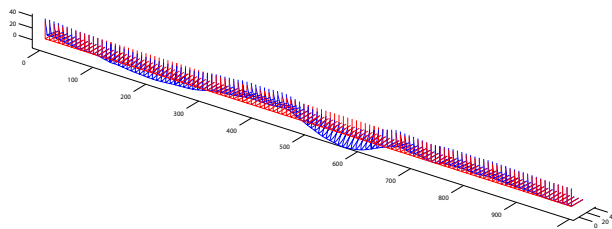


**Figure 8.4:** A screendump of the MATLAB model. The soil springs are illustrated with lines, just like the tunnel beam elements. An animated version of the figure is provided on the enclosed DVD.

In the present section, it is described, how stiffness's of the soil springs and the gaskets are determined. The material properties are described in Chapter 5.

### 8.2.1 Soil spring stiffness

The soil springs model the soil-structure interaction. An infinite soil spring stiffness,  $k = \infty$ , would imply that the tunnel was restricted to the free-field deformations of the soil, while a zero soil spring stiffness,  $k = 0$ , would imply that no contact existed between the soil and the tunnel.

The spring stiffness's of the soil springs shown in Figure 8.1 are calculated with the Finite Element code ABAQUS. A model has been built in the same way as explained in Chapter 9, however, the tunnel has been modelled as a rigid body, since it is only the stiffness of the soil which should be determined. The mesh is shown in Figure 8.5. ABAQUS has been chosen for the analysis to make the results obtained with the Winkler model comparable to the results from the ABAQUS continuum model.

The equivalent soil stiffness's are determined by applying loads to the appropriated faces of the tunnel, in a static analysis. From the corresponding deformation of the

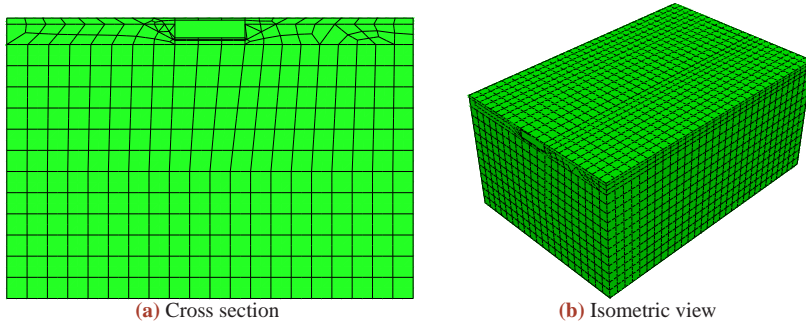


**Figure 8.5:** The meshed domain for the soil spring calculations.

tunnel, the soil stiffness can be determined. Since the performed analysis is entirely linear, the work curve is straight. Thus, only a single load-deformation relation is needed to determine the stiffness for a spring.

### Transverse and vertical soil springs

The boundary conditions for the determination of the transverse and vertical soil spring stiffness's are: *encastre* (fully fixed) on the sides and the bottom, and no deformation in the  $x$ -axial direction on the ends. The definition of the surface terminology of the model is given in Figure 8.6. These boundary conditions yield a state of plain strain in the model.

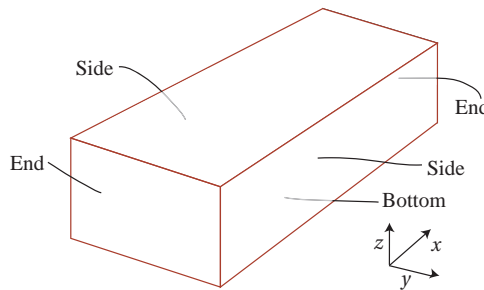


**Figure 8.6:** Terminology definition for the ABAQUS analysis.

The deformation modes are depicted in Figure 8.7 and the calculated soil stiffness's are given in Table 8.1 on page 62.

Since the transverse and vertical soil springs are determined by plane strain analyses, it is possible to verify the calculated stiffness's directly in a two-dimensional analyses. This has been done in PLAXIS, a commercial finite element code for soil and rock analysis. A model equivalent to the ABAQUS continuum model has been established. The domain, meshed with 15-node elements, is shown in Figure 8.8a. Transverse and vertical loads have been applied and the corresponding deformation figures are depicted in Figure 8.8b and 8.8c.

The stiffness's calculated with ABAQUS and PLAXIS are listed in Table 8.1, given as spring stiffness's per metre in the longitudinal tunnel direction. It can be seen that only minor differences between the calculated stiffness's exist. These differences are

## Transverse and vertical soil springs

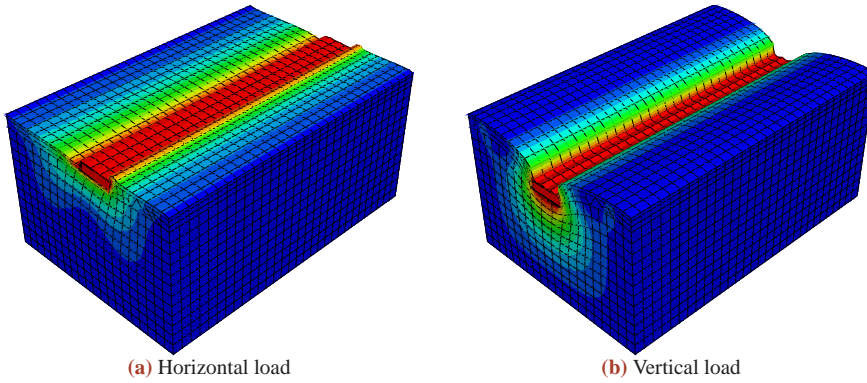


**Figure 8.7:** Deformation modes for the transverse and vertical soil spring analyses in ABAQUS. The intensity (from blue to red) of the colour illustrates the magnitude of the displacement.

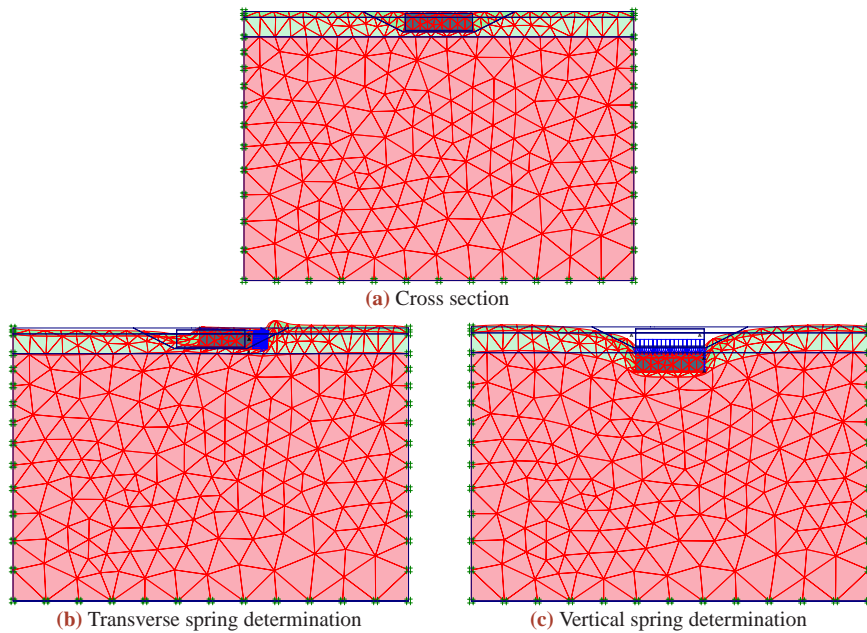


**Figure 8.8:** The PLAXIS plain strain model for calculation of the transverse and the vertical soil springs. The results are given in Table 8.1.

purely due to differences in the discretization. Thus, the calculated soil stiffness's are verified. In the further calculations, the stiffness's calculated with ABAQUS are used, since the Winkler model will be compared to the ABAQUS continuum model.

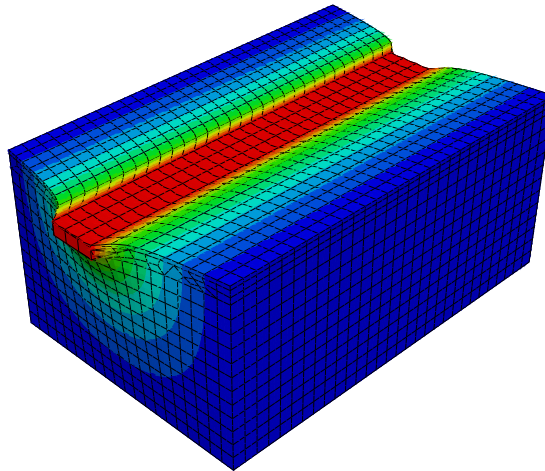
**Table 8.1:** The calculated soil stiffness's from ABAQUS and PLAXIS.

Direction	Spring stiffness $k$ [ $\frac{N}{m \cdot m}$ ]	
	ABAQUS	PLAXIS
Transverse	$1.492 \cdot 10^9$	$1.477 \cdot 10^9$
Vertical	$2.668 \cdot 10^9$	$2.712 \cdot 10^9$

### Longitudinal soil springs

For the calculation of the longitudinal soil springs, the boundary conditions are changed. The objective is to model the deformation of an infinitely long tunnel, *i.e.* a unit stiffness per metre in the tunnel axial direction. The bottom and the sides are still subjected to *encastre*, but on the ends, only deformation in the  $x$ -axial direction is allowed, cf. Figure 8.6. These boundary conditions, together with a load on the tunnel end, introduces a state of anti-plane strain in the domain, *i.e.* only deformation in the  $x$ -axial direction is present.

In Figure 8.9 the deformation mode is shown. It has been verified that no significant displacements occur in the direction of the  $y$ - and  $z$ -axes. The soil spring stiffness is calculated in the same way as the in-plane springs, from the deformation due to an applied load, to  $0.746 \cdot 10^9 \frac{N}{m \cdot m}$ .

**Figure 8.9:** The ABAQUS mesh and displacement for the longitudinal soil spring stiffness.

To verify the calculation, *e.g.* an axisymmetric model could be build, in a program which allows deformation with the azimuth angle  $\theta$ . If the radius  $R$  in the model is much greater than the width  $W$  of the tunnel, the curvature of the tunnel approaches zero and an “infinite” tunnel is approximated. Thus, for great values of  $\frac{R}{W}$ , the axisymmetric model provides a good approximation of the anti-plane strain problem. The principles of the model are sketched in Figure 8.10. The model has not been investigated further.

The calculated soil spring stiffness's, which will be used for the Winkler model, are summarized in Table 8.2.

## Gasket stiffness

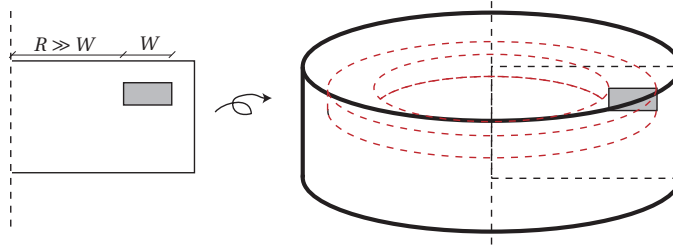


**Figure 8.10:** A possible axisymmetric model to calculate the longitudinal stiffness.

**Table 8.2:** The calculated soil stiffness's.

Direction	Spring stiffness $k$ [ $\frac{N}{m \cdot m}$ ]
Horizontal	$1.492 \cdot 10^9$
Vertical	$2.668 \cdot 10^9$
Longitudinal	$0.746 \cdot 10^9$

### 8.2.2 Gasket stiffness

The gaskets are modelled with multiple springs, as it is illustrated in Figure 8.11. A single longitudinal spring models the axial stiffness, while two shear springs model the stiffness in the transverse and vertical direction.

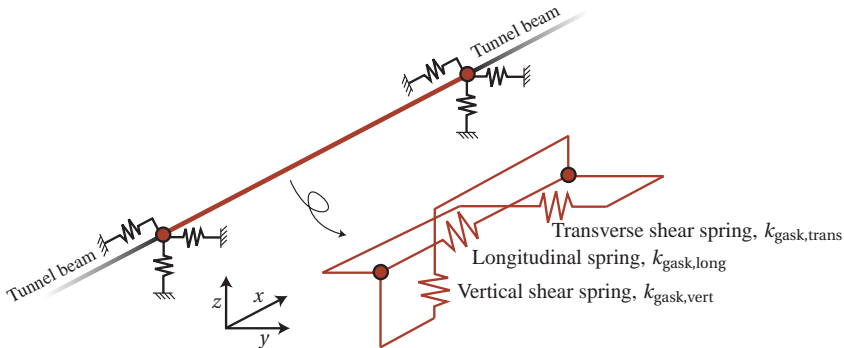


**Figure 8.11:** Modelling of gasket. Excerpt from Figure 8.1.

The equivalent longitudinal spring stiffness,  $k_{gask,long}$ , can be found from the linearized gasket stiffness chosen in Section 5.6.1 on page 35. The gasket circumference is in Appendix D stated as 84.4m, whereby the spring stiffness can be calculated to

$$\begin{aligned}
 k_{gask,long} &= 24 \frac{MN}{m^2} \cdot 84.4 \text{ m} \\
 &= 2.05 \cdot 10^9 \frac{N}{m}
 \end{aligned}
 \tag{8.1}$$

The shear stiffness of the gaskets is discussed in Section 5.6.2. It follows from (5.14) that the shear stiffness's  $k_{gask,trans}$  and  $k_{gask,vert}$  are determined as

$$\begin{aligned}
 k_{gask,trans} = k_{gask,vert} &= \frac{k_{gask,long}}{3} \\
 &= 0.68 \cdot 10^9 \frac{N}{m}
 \end{aligned}
 \tag{8.2}$$

### 8.2.3 Damping

The damping of the tunnel and the gaskets is estimated to a loss factor of  $\eta = 0.01$ , according to Section 5.3.1. In the time domain, viscous damping is applied. The dominant frequency is set to the first eigenfrequency of the soil,  $f = 1.09$  Hz, according to Figure 5.3b on page 31.

The relation between the element damping matrices and the element stiffness matrices,  $\beta$ , is found according to (5.10) and (5.11) on page 31 to

$$\begin{aligned} 0.01 &= 2\pi \cdot 1.09 \text{ Hz} \cdot \beta \\ \beta &= 1.46 \cdot 10^{-3} \end{aligned} \quad (8.3)$$

In the same way, the damping for the soil springs are found. It is chosen to use the loss factor of the upper soil layers,  $\eta = 0.05$ , cf. Figure 5.4, which for viscous damping approximates to  $\beta = 7.30 \cdot 10^{-3}$ .

### 8.2.4 Discretization

The tunnel elements are discretized into a smaller number of finite element beams. Since the soil springs are connected to the tunnel at the ends of each beam element, the number of beams also determines the discretization of the soil-structure interaction. To determine the discretization needed, a convergence analysis has been carried out. The result is shown in Figure 8.12. On the ordinate axis the normalized tunnel damage, defined in Section 5.7, is plotted. It can be seen that sufficient accuracy is obtained with around 20 beam elements per tunnel element, which has been used in the analyses.

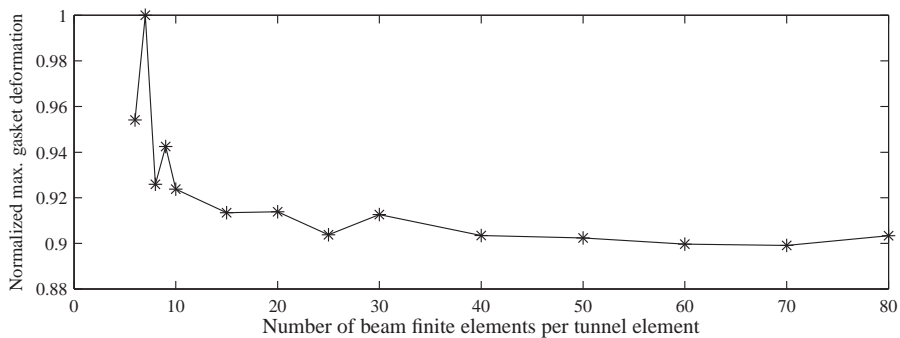


**Figure 8.12:** Convergence of the Winkler model.

## 8.3 Input motion

The input strong motion is the earthquake time series calculated with the domain transformation method which is accounted for in Section 6.2. The time series at the level of the tunnel is depicted in Figure 6.12 on page 50. The calculated time series is applied

to the outer ends of the soil springs, shifted in time to model the incoherence of the propagating wave, caused by the apparent velocity.

## 8.4 Output

The output of the analysis should be the damage of the gaskets, according to Section 5.7. Offhand, the output from the Winkler model is the displacement in the degrees of freedom, *i.e.* translations and rotations at the tunnel ends. Translation and rotation of two adjacent tunnel elements are sketched in Figure 5.14. The translation and rotation of the tunnel ends can be transferred to the absolute three-dimensional location of the gasket corners, from which the deformation in the gasket corners can be found.

Firstly, the three-dimensional coordinate of every corner point (shown in Figure 5.14) is calculated. Then, the gasket deformation can simply be calculated as the change in the absolute distance between two matching corners. A sketch of a tunnel end, with the corner nodes and the degrees of freedom depicted, is presented in Figure 8.13.

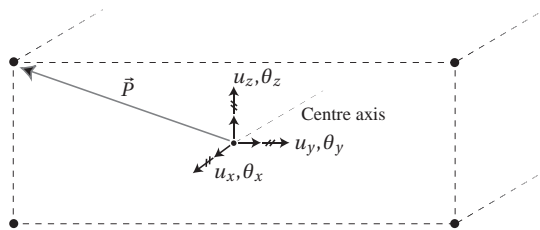


**Figure 8.13:** The degrees of freedom at the end of a tunnel element.  $\vec{P}$  is the direction vector to a corner node.

### 8.4.1 Translations

The translations from the degrees of freedom,  $u_x$ ,  $u_y$  and  $u_z$ , are simply added to the original coordinates of the corners.

### 8.4.2 Rotations

The rotational degrees of freedom,  $\theta_x$ ,  $\theta_y$  and  $\theta_z$ , yields an resulting displacement of each of the corner nodes which should be taken into consideration. To calculate this displacement, the direction vector of a corner,  $\vec{P}$ , is introduced. It is depicted in Figure 8.13. This vector is rotated according to the degrees of freedom, thus calculating the new corner coordinate. The calculation of the rotation is described more closely in Appendix E.



## CONTINUUM MODEL

As an alternative to the Winkler model, a full continuum model has been established in the commercial FE program ABAQUS. In this chapter, the modelling is described.

The ABAQUS CAE-files and output databases are enclosed on the attached DVD.

### 9.1 Parts and meshes

The model is built of three parts: Tunnel elements, gaskets and the soil. Instances of these parts are gathered in an assembly.

All parts of the model are built of continuum elements, of the types C3D20R (brick) and C3D15 (wedge). The brick elements are used for the major part of the domain, and the wedge elements are used to fill minor regions. The elements are shown in Figure 9.1. The elements are quadratic (second-order) elements, which are suitable for modelling of wave propagation, as it is also discussed in Section 6.3.1 on page 46.

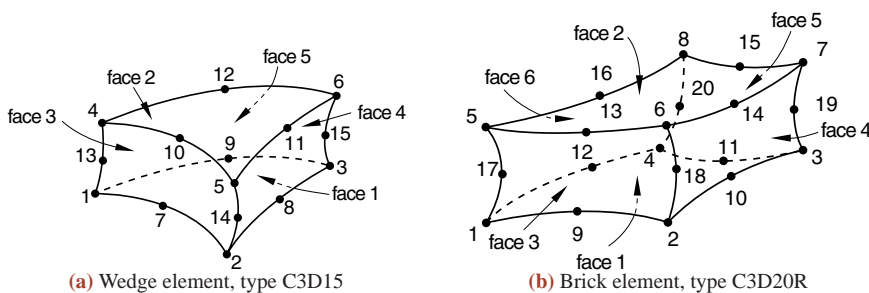


**Figure 9.1:** Elements used in the ABAQUS analysis. (Simulia 2007)

The most important assumptions made during the modelling of the continuum model

are stated in Section 8.1. The assumptions are common to the Winkler and the continuum model.

### 9.1.1 Tunnel

The eight tunnel elements are all identical. A tunnel part is shown in Figure 9.2

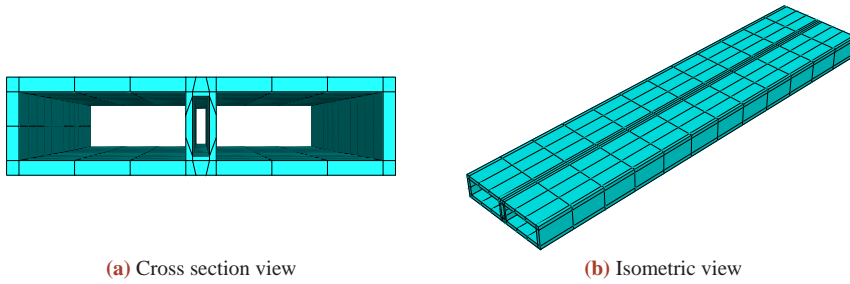


**Figure 9.2:** The meshed tunnel element part.

### 9.1.2 Gaskets

The Gina gaskets connect the tunnel elements. A Gina gasket part is shown in Figure 9.3. It should be noted that the mesh of the gasket is generated such that it conforms well to the mesh of the tunnel elements. This makes the assembly more accurate, as it is discussed in Section 9.4.

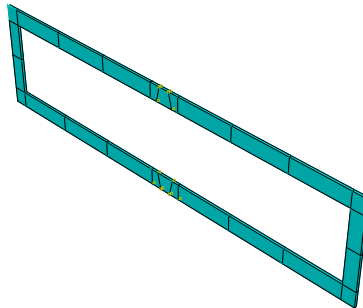


**Figure 9.3:** The meshed Gina gasket.

The gasket is modelled 0.20m deep, and the elements are provided with a material orientation, to make the use an orthotropic material model possible.

The gaskets are modelled with ordinary continuum finite elements. It has also been investigated, if the special gasket elements provided in ABAQUS would provided a better modelling. These elements, however, entails a very realistic modelling of the gasket behaviour, since they require the initial compression of the gaskets, obtained during the tunnel installation phase, to be a part of the modelling. Even if this would result in a more accurate, non-linear, modelling, it would not correspond with the modelling of the Winkler model, thus introducing another possible factor of divergence between

the models. These factors are already deemed to be plenty in number, as it is outlined in Section 8.1.

### 9.1.3 Soil

The soil is modelled as a single part, divided into the three layers. A hole to contain the tunnel is included. The dredged trench is modelled, and the parameters of the backfilling are set equal to the parameters of soil A, cf. Table 5.2 on page 29, as no better data for the backfilling exist. The order of magnitude for the parameters of soil A correspond well to *e.g.* soaked sand, cf. Andersen (2006, p3).

The soil part is shown in Figure 9.4

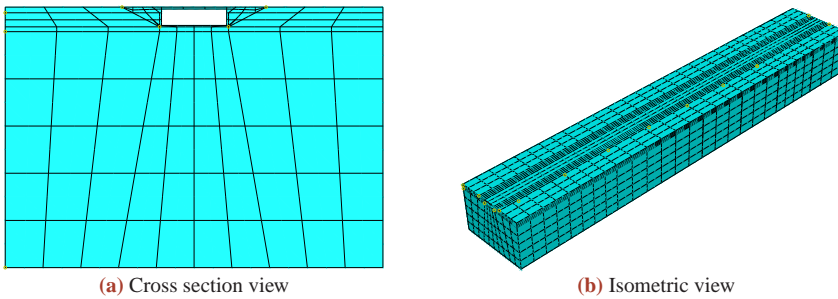


**Figure 9.4:** The meshed soil part.

### 9.1.4 Discretization considerations

The mere name of the finite element method implies that a discretization has to be made. The accuracy of any finite element model is pinned to the choice of a suitable meshing of the domain and to an accurate time integration algorithm.

#### Mesh coarsness

The coarsness of the mesh has been chosen as a balancing between the calculation time of the model and the accuracy of the obtained solution.

The size of the elements should be compared to the wave length of the propagating waves, which depends on the frequency of the waves and the propagation velocity. The slowest wave velocity is the S-wave velocity cf. Table 5.2. For soil layer C, which has the largest elements and comprises the majority of the domain, the S-wave velocity is  $600 \frac{\text{m}}{\text{s}}$ .

The frequency of the incident waves of importance is maximum 2.0 Hz, cf. Figure 6.11 on page 50. Thus, the minimum wave length  $l_{\min}$  can be calculated as

$$l_{\min} = \frac{600 \frac{\text{m}}{\text{s}}}{2.0 \text{ s}^{-1}} = 300 \text{ m} \quad (9.1)$$

The longest side of an element in the meshed model is approximately 38.5 m. Thus, no less than seven second-order elements are available anywhere in the model to model

each wave component. This is deemed to be sufficient to obtain a proper accuracy of the calculation.

### Time integration

When performing the time integration, the size of the time step should be given considerations in order to obtain an accurate solution. The time step used for the analyses is  $\Delta t = 0.01$  s, which is equal to the sampling rate of the earthquake time series.

The time integration in ABAQUS performed with the dynamic, implicit scheme. The method is called the Hilber-Hughes-Taylor operator, and the method is unconditionally stable for linear systems; meaning that there is no mathematical limit on the size of the time increment that can be used (Simulia 2007). Thus, the solution will not “explode” when the time step is increased.

The correspondence between the time step, the element size and the wave speed should also be observed. If *e.g.* the element size is too small when compared to the other parameters, it might happen that a wave will pass through an element, without being noticed by the element. The correlation is formulated in the *Courant condition*

$$\frac{c \Delta t}{h} = C, \quad C \leq 1 \quad (9.2)$$

(Andersen 2006, 72) where  $c$  and  $h$  represent a characteristic set of wave propagation speed and element size, and  $C$  is the *Courant number*.

It follows from (9.2) that if the greatest wave speed is around  $c = 2000 \frac{\text{m}}{\text{s}}$ , and the time step is  $\Delta t = 0.01$  s, the smallest element should be around 20 m. This is obeyed by the majority of the elements in the domain. The exception is the places where the geometry directs a finer discretization, *e.g.* in soil layer A which is only 3 m in thickness. In Section 9.6.3 it is analysed, how changes in the time step affects the calculated displacements inside the domain.

### Computation time

With the chosen discretization, a transient analysis of the first 15 s of earthquake loading and response takes about four hours to complete. The computation is performed on the Department of Civil Engineering’s computer cluster, and runs serial on a single computational node. The programmed input files which executes a calculation on the cluster are enclosed on the attached DVD.

## 9.2 Material modelling

In this section, the material data needed for the model is presented. The continuum elements are modelled with homogeneous, isotropic, linear elastic materials, as it is also the assumption for the domain transformation method, which forms the input for the Winkler model, cf. Section 6.1. The material data needed for such materials for a dynamic analysis are the Young’s modulus  $E$ , Poisson’s ratio  $\nu$  and the density  $\rho$ . The

exception is the Gina gaskets which are modelled with orthotropic elements, making it possible to control the behaviour of the gasket more accurately.

### 9.2.1 Soil

The densities for the soil layers are given in Table 5.1 on page 28. The Young's modulus and the Poisson's ratio can be found from the inverse relationships of (A.2)

$$E = \frac{\mu(3\lambda + 2\mu)}{\lambda + \mu}, \quad \nu = \frac{\lambda}{2(\lambda + \mu)} \quad (9.3)$$

(Andersen 2006, p8)

The Lamé constants  $\lambda$  and  $\mu$  can be determined from the P- and S-wave velocities  $c_P$  and  $c_S$ , which are given in Table 5.2 on page 29. The relations are: ((A.4) is reprinted for convenience)

$$\begin{aligned} c_P &= \sqrt{\frac{\lambda + 2\mu}{\rho}}, & c_S &= \sqrt{\frac{\mu}{\rho}} \\ \Rightarrow \mu &= c_S^2 \cdot \rho, & \lambda &= c_P^2 \cdot \rho - 2\mu \end{aligned} \quad (9.4)$$

(St John & Zahrah 1987, p171)

The resulting soil data are presented in Table 9.1 on page 73.

### 9.2.2 Tunnel

The tunnel elements are cast of reinforced concrete. The Young's modulus for initial compression, which is of the present interest, can be determined from a deemed ultimate strength of  $f_{ck} = 50$ MPa to  $E_0 = 40$ GPa, according to DS411 (1999, p24). The Poisson's ratio is estimated to  $\nu = 0.15$ .

### 9.2.3 Gasket

The modelling of the Gina gasket is performed such that it corresponds well to the Gina gaskets of the Winkler model, illustrated in Figure 8.11 on page 63. Thus, a continuum equivalence to linear springs is desired. While this may not be the most accurate representation of the actual physical problem, it is comprehensible and should behave similar to the Winkler model. The gasket modelling of the Winkler model and the continuum model are depicted in Figure 9.5 on the following page.

The desired behaviour of the Gina profiles can be modelled with an orthotropic material, whose material stiffness matrix,  $\mathbf{D}$ , is computed as

$$\mathbf{D} = \begin{bmatrix} 1/E_1 & -\nu_{21}/E_2 & -\nu_{31}/E_3 & 0 & 0 & 0 \\ -\nu_{12}/E_1 & 1/E_2 & -\nu_{32}/E_3 & 0 & 0 & 0 \\ -\nu_{13}/E_1 & -\nu_{23}/E_2 & 1/E_3 & 0 & 0 & 0 \\ 0 & 0 & 0 & 1/G_{12} & 0 & 0 \\ 0 & 0 & 0 & 0 & 1/G_{13} & 0 \\ 0 & 0 & 0 & 0 & 0 & 1/G_{23} \end{bmatrix} \quad (9.5)$$

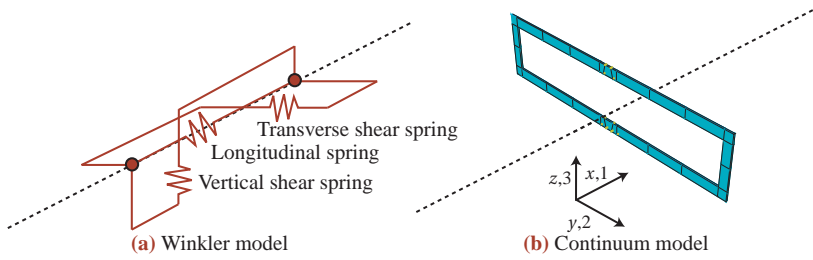


**Figure 9.5:** Gasket modelling in the Winkler and the continuum model. Excerpts from Figure 8.11 and Figure 9.3.

(Simulia 2007)

The constants appearing in (9.5) on the previous page can be determined from the desired behaviour of the gaskets. The indices are defined by the coordinate system in Figure 9.5, where it is also seen that the gasket should be decoupled between the transverse, vertical and longitudinal deformation. This is accomplished by setting the Poisson's ratios  $\nu_{ij} = 0$ . Thus, the material stiffness matrix is symmetric, which in any case always should hold by setting  $\nu_{12} = \nu_{21} E_1 / E_2$  etc.

The stiffness in the longitudinal direction,  $E_1$ , is determined on the basis of the gasket stiffness found in (8.1) on page 63. The area of the gasket in Figure 9.3 is  $103.12 \text{ m}^2$  and the thickness is  $0.2 \text{ m}$ , thus yielding the equivalent computational stiffness as

$$\begin{aligned}
 E_1 &= \frac{2.05 \cdot 10^9 \frac{\text{N}}{\text{m}} \cdot 0.2 \text{ m}}{103.12 \text{ m}^2} \\
 &= 3.98 \cdot 10^6 \frac{\text{N}}{\text{m}^2}
 \end{aligned}
 \tag{9.6}$$

The transverse and vertical stiffness's,  $E_2$  and  $E_3$ , respectively, are not important, since the corresponding faces of the gaskets do not interact with any other faces, and the Poisson's ratios are set to zero. With the same arguments, the shear stiffness in the axial direction,  $G_{23}$ , is not important either.

The shear stiffness of the gaskets is treated in Section 5.6.2. According to (5.14), the shear stiffness's of the gaskets in the transverse and vertical direction,  $G_{12}$  and  $G_{13}$ , respectively, can be determined as

$$\begin{aligned}
 G_{12} = G_{13} &= \frac{E_1}{3} \\
 &= 1.33 \cdot 10^6 \frac{\text{N}}{\text{m}^2}
 \end{aligned}
 \tag{9.7}$$

This calculation assumes Poisson's ratio  $\nu = 0.5$ , which is true for an incompressible material which is a good approximation for rubber. Above, Poisson's ratio was set to zero, but this is only to make decoupling possible in ABAQUS. The two values of Poisson's ratio therefore are absolutely unrelated.

### 9.2.4 Damping

The damping mechanism is viscous damping, cf. Section 5.3. The relation between the element damping matrices and the element stiffness matrices are determined simi-

larly to (8.3) on page 64. The consequence of the application of viscous damping over hysteretic damping is analysed in Section 11.4.2.

### 9.2.5 Summary

The material data are summarized in Table 9.1. The data of the gasket are listed in Section 9.2.3.

**Table 9.1:** Material data for the ABAQUS model.

Material	Density $\rho \left[ \frac{\text{kg}}{\text{m}^3} \right]$	Young's modulus $E \text{ [Pa]}$	Poisson's ratio $\nu [-]$	Damping $\beta [-]$
Soil layer A	1900	$0.35 \cdot 10^9$	0.49	$7.30 \cdot 10^{-3}$
Soil layer B	2100	$0.76 \cdot 10^9$	0.48	$7.30 \cdot 10^{-3}$
Soil layer C	2100	$2.19 \cdot 10^9$	0.45	$4.38 \cdot 10^{-3}$
Reinforced Concrete	2500	$40 \cdot 10^9$	0.15	$1.46 \cdot 10^{-3}$

### 9.3 Earthquake loading

The strong ground motion generated by the earthquake is applied in the model as forced displacements. Different ways of applying the displacements to the domain can be chosen. Some of the methods are sketched in Figure 9.6.

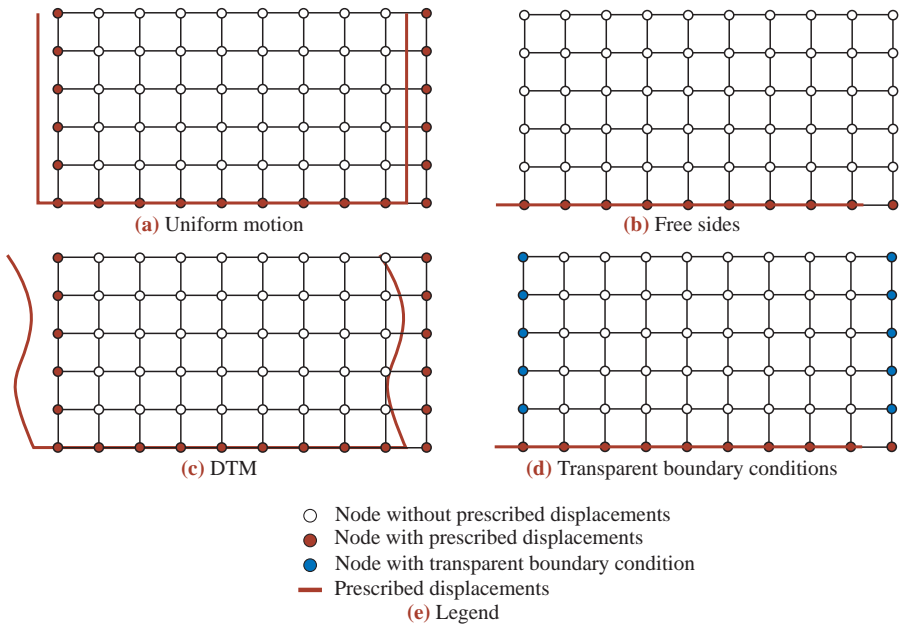


**Figure 9.6:** Possible boundary conditions for a cross section of the soil domain. For simplicity, only transverse deformations are shown.

In Figure 9.6a, the input time series is applied to all nodes on the outer surfaces. However, it is known that this would prescribe incorrect free-field displacements on the side, since the free-field deformations are calculated in Chapter 6.

Another possibility is shown in (b), where the earthquake displacement time series is applied only to the bottom surface. While this approach at first may appear feasible, it totally disregards the stiffness and the mass of the soil outside the modelled domain, thus providing a too flexible model.

Therefore, the boundary conditions of (c) are applied to the continuum model. On the sides of the domain, the deformation is prescribed according to the displacements in the specific level, calculated with the domain transformation method as described in Section 6.2. Thus, the far-field displacements are prescribed fully by the free-field deformations, while the near-tunnel field are left to the continuum model to calculate.

Another possible way of modelling the boundary conditions appropriate could be with *transparent boundary conditions* (TBCs), depicted in (d). TBCs do not prescribe any motion as standard Dirichlet or Neumann conditions (*e.g.* displacements or stresses, respectively) but are formulated such that they absorb the outgoing energy of the waves, thereby preventing reflection. TBCs are normally formulated for waves in a specific direction, but multi-directional formulations have been provided by *e.g.* Higdon (1992). However, TBCs do not provide full transmission for domains with free surfaces, as discussed by Andersen *et al.* (2007, p47). To absorb the surface waves, *e.g.* Rayleigh waves, Bamberger *et al.* (1990) has suggested the use of buffer zones, so-called “ears” which are applied to the model close to the free surface and applies fictitious damping.

Instead of TBCs, *infinite elements* could be applied. This type of artificial boundary conditions is directly available in ABAQUS, however not in the CAE-interface, and are only fully transmitting in a specific direction (Simulia 2007). Yet another possibility for the formulation of a wave-radiating domain could be an application of the boundary element (BE) method, which in its formulation have an inherent ability to radiate waves. BEs could be coupled with FEs, as it is discussed by *e.g.* Andersen *et al.* (2007, p54-56).

While the concept of transparent boundary conditions seems commendable, the application can be quite tortuous, especially if another formulation than infinite elements should be implemented in the ABAQUS code. However, the use of wave-transmitting boundaries would be essential if *e.g.* the near-field was prescribed and the far-field unknown, as it is the case for the wave motion from *e.g.* pile driving. In the present thesis, since the far-field displacements are prescribed and the near-field the area of interest, the concept of (c) has been employed.

The incoherence of the wave, due to the apparent velocity, is accounted for with a time shift for each node, dependent on the three-dimensional distance from the node to the wave front.

The automated generation of a specific time series for each and every boundary node is not possible in the CAD-like ABAQUS CAE interface. Therefore, a user subroutine, *disp*, has been implemented. The subroutine has been written in FORTRAN and is enclosed on the attached DVD.

## 9.4 Assembly

The above mentioned parts are put together in an assembly, a section of which is shown in Figure 9.7.

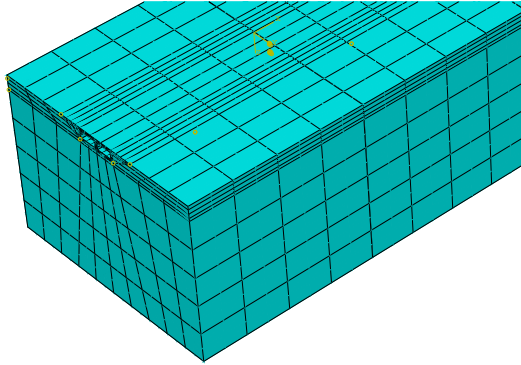


**Figure 9.7:** The assembly.

### 9.4.1 Ties

The surfaces are connected with surface-to-surface *ties*, which share the nodes of adjacent surfaces. This reduces the size of the system matrices, eliminating the degrees of freedom at the node of the slave surfaces.

This modelling has been used, since it is deemed that there will be no significant slip between the tunnel and the soil, nor will there be any longitudinal shear displacement. If this should be the case, a more appropriate modelling can be obtained by use of surface-to-surface contact interactions. These are, however, non-linear in nature.

With the use of ties the same fundamental problem with nominal tensile stresses in the soil, discussed in Section 1.3, arises. However, due to the oscillations around the state of equilibrium, the use of ties in the present context is justified.

### 9.4.2 Master and slave surfaces

To establish a tie between two surfaces, a master surface and a slave surface should be defined. During the solving of the matrix system, the ties then exclude the degrees of freedom at the nodes of the slave surfaces. Instead, the degrees of freedom at nodes on the master surface are used, thus reducing the size of the matrices.

In general, two surfaces connected with ties can not be expected to have nodes with the very same coordinates. The link between a node on the slave and master surface is therefore computed for each slave node, such that each slave node connects with the nodes of the master surface, which is nearer to the slave node. This is shown in Figure 9.8 on the following page, where slave surface node *c* connects to node 402 on the master surface. If the projection point of the slave node on the master surface does not lie directly onto a master surface node, the degrees of freedom are interpolated according to the shape function of the master surface. Hence, the degrees

of freedom e.g. for slave surface node a are calculated from the degrees of freedom of master surface nodes 202, 203, 302 and 303.

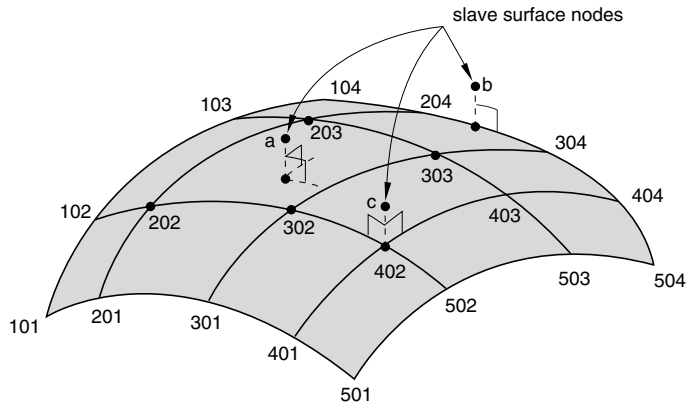


**Figure 9.8:** A tie constraint between slave nodes and a master surface. (Simulia 2007)

In the special case of the tie between the tunnel and the Gina gasket, it does not make any difference, which surface is the master or the slave, since the meshed are identical. However, in most cases the choice of master and slave surfaces requires some consideration. The slave surface mesh should, in general, be finer than that of the master surface; thus making sure that a connection will exist between all nodes of the two surfaces.

In the present model, the ties between the soil and the tunnel elements are modelled with the tunnel as slave surface. For the ties of the gaskets and the tunnel elements, the tunnel elements therefore are the master surfaces. This is necessary, since no node can belong to two slave surfaces.

## 9.5 Output

The required output is specified in Section 5.7 on page 38. The continuum model serves the purpose of analysing the model assumptions connected to the Winkler model. Therefore, the output of the continuum model should be made comparable to the output of the Winkler model, described in Section 8.4.

### 9.5.1 Deformation at corners

Since the corners of the gaskets are nodes in the continuum model, the displacements can be extracted and the deformation at the corners can be calculated directly.

### 9.5.2 Degrees of freedom equivalent to Winkler model

To compare the continuum model to the Winkler model when no gaskets are modelled, as it is done in Section 10.2.5, it is necessary to be able to equate the three-

## Translational DOF

dimensional displacement field from ABAQUS to the Winkler model, as it is illustrated in Figure 9.9.

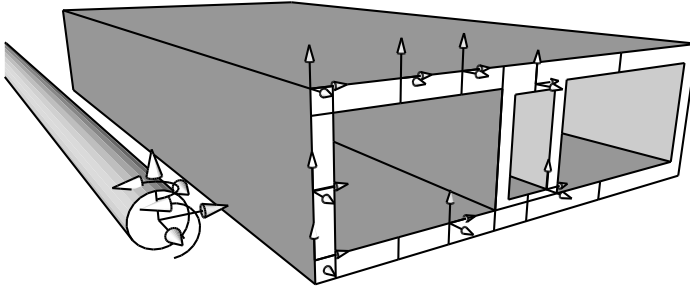


**Figure 9.9:** Sketch of the problem: the conversion from the continuum model (right) to the beam model (left). The arrows illustrate the degrees of freedom.

The reduction of the continuum model to six degrees of freedom (DOF) in an equivalent beam involves a lot of choices, and no perfect solution exists. Furthermore, all internal modes of deformation, *e.g.* warping or racking (cf. Section 4.5), in the continuum model are disregarded.

Firstly, it is chosen to use the corner nodes and the quadrilateral they form as the basis for the calculation, thus disregarding all other nodes. The calculation is implemented in the postprocessing program, coded in MATLAB and enclosed on the attached DVD.

### Translational DOF

The translational degrees of freedom are easily calculated as the simple mean value of the displacement for the four corners.

### Rotational DOF

The rotational degrees of freedom can not be defined unambiguously from the displacement in the four corner, since only three nodes are necessary to define a plane in the three-dimensional space. Since only small rotations are present, it is chosen to define the rotation about an axis as the rotation of the direction vector between two centre points, as it is sketched in Figure 9.10 on the next page for the rotation about the  $y$ -axis. In the depicted example, only the coordinates in the  $xz$ -plane are used for the calculation of  $\theta_y$ .

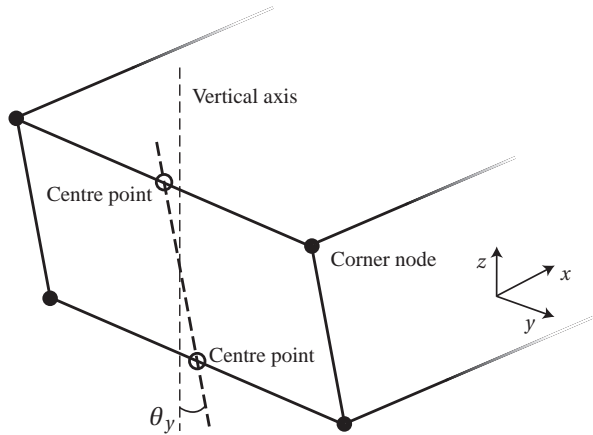


**Figure 9.10:** Rotational DOF from corner nodes.

## 9.6 Verification of models

In this section, the continuum model is used for verification of the DTM. It is also verified that the free-field waves applied in the Winkler model can be reproduced by the continuum model. Finally, the size of the time step is analysed.

### 9.6.1 Boundary conditions

Firstly, it is verified that the applied boundary conditions, the time series calculated with the DTM, is correct and corresponds to the material properties entered in ABAQUS. This is tested by applying the earthquake motion to a layered soil domain without the tunnel, depicted in Figure 9.11.

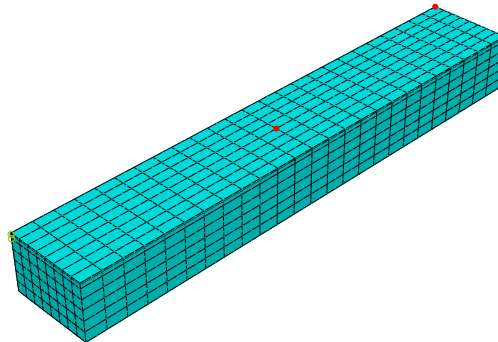


**Figure 9.11:** The layered soil domain without tunnel. The dots show the nodes for which the timeseries is plotted in Figure 9.13.

The Aegion time series is applied to the soil domain in Figure 9.11 without any delay due to apparent velocity. The displacements on the sides of the domain are calculated with DTM, using hysteretic damping.

A screen dump of the deformation is shown in Figure 9.12 on the next page, and two time series are plotted in Figure 9.13. It should be noted that very little difference

## Boundaries calculated with viscous damping

exists between the displacement at the outer surface, which is forced, and the displacement inside the domain, which is calculated in abaqus. This verifies both the DTM and the continuum model.

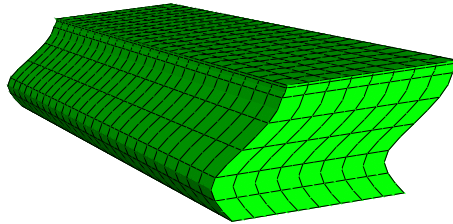


**Figure 9.12:** The soil domain during the execution of the time series. Note that the deformation is uniform over the cross section. An animated version of the figure is provided on the enclosed DVD.

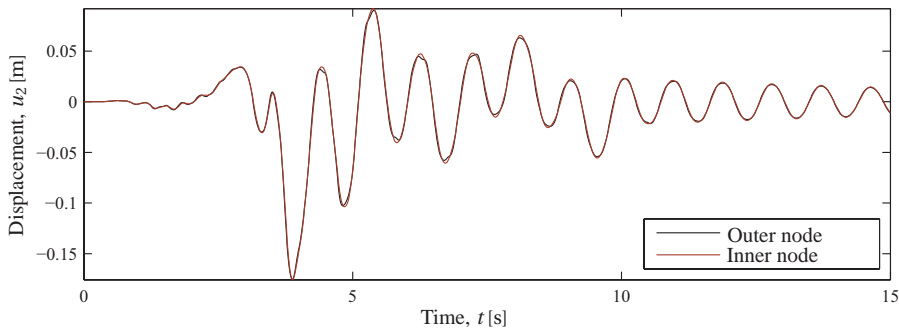


**Figure 9.13:** Displacement time series for the two nodes set off in Figure 9.11. Input from DTM with hysteretic damping.

## Boundaries calculated with viscous damping

Even though the time series plotted in Figure 9.13 seem to be very alike, small differences exist. This is more clearly seen at places with high acceleration. This effect is due to the different damping models used for the calculation of the input forced displacements and in the continuum model itself. While the domain transformation method uses hysteretic damping in the frequency domain, the time domain calculation in ABAQUS utilizes viscous, proportional damping. The differences are further described in Section 5.3.

To illustrate the consequence of the use of different damping methods, new time series have been generated with the domain transformation method, now using viscous damping, even though this damping method corresponds less well to the behaviour of soil. The corresponding time series for the two nodes shown in Figure 9.11 are plotted in Figure 9.14 on the following page.

To see the difference between Figure 9.13 and Figure 9.14 more clearly, close-ups are plotted in Figure 9.15 on the next page. Here it is clearly seen that if the same damping model is used for the boundary conditions and for the continuum model itself, a much more accurate reproduction is possible. However, since hysteretic damping still is

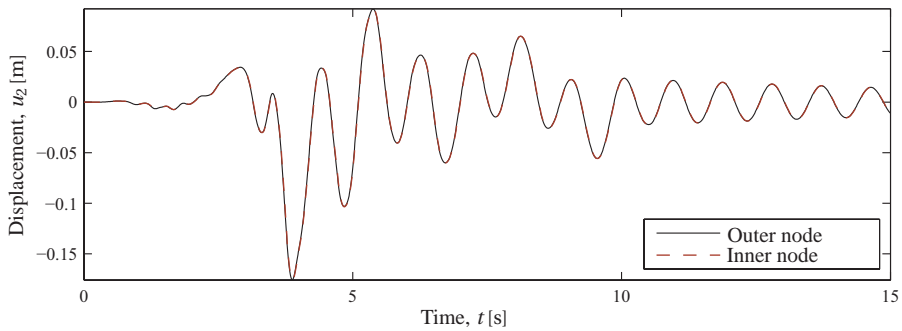


**Figure 9.14:** Displacement time series for the two nodes set off in Figure 9.11. Input from DTM with viscous damping.

regarded a better model of the behaviour of soil, but simply not available in the time domain, hysteretic damping will remain to be used for the calculations with the DTM henceforth.

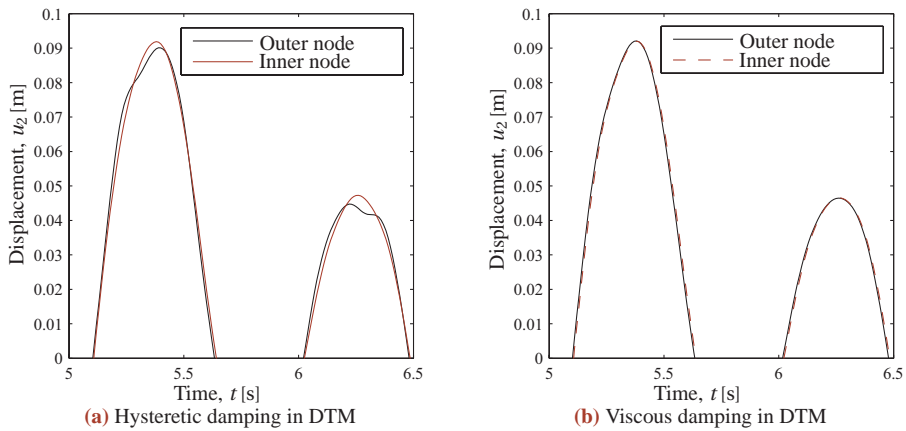


**Figure 9.15:** Close-up of Figure 9.13 and Figure 9.14.

Furthermore, the same difference between the soil response calculated with hysteretic and viscous damping has been observed in Section 11.4.2 on page 108, as a clear verification of the results presented in Figure 9.15 and a verification of the coding of the continuum model.

### Incompatible boundaries

It may not be obvious that significant difference could exist between forced displacements at the outer surface of the domain and the calculated displacements inside the domain. The importance of compatibility between the stiffness and mass of the model and the forced displacements can however easily be illustrated, *e.g.* by using the original Aegion time series for all forced displacements, exactly as it is sketched in Figure 9.6a on page 73. A calculation with these boundary condition yields the displacements plotted in Figure 9.16. It is clearly seen that the incompatibility between the

continuum model and the boundary conditions provides great difference between excitation and response.

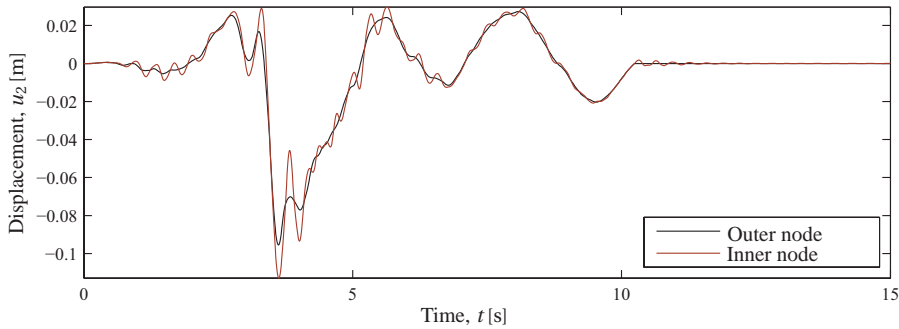


**Figure 9.16:** Displacement time series for the two nodes set off in Figure 9.11. Input at all boundary surfaces is the original earthquake time series, as sketched in Figure 9.6a, *i.e.* the prescribed motion is incompatible with the soil in the domain.

## 9.6.2 Representation of free-field soil deformation

The Winkler model assumes that the wave propagation is one-dimensional, meaning that the response on a given point on the soil surface can be calculated directly from the displacement time series in the bedrock directly below the point. This is illustrated in Figure 9.17a. However, it seems reasonable that the waves in some cases could propagate in two or three dimensions, making the calculation of the surface response more complicated. The principle of multi-dimensional wave propagation is sketched in 9.17b.

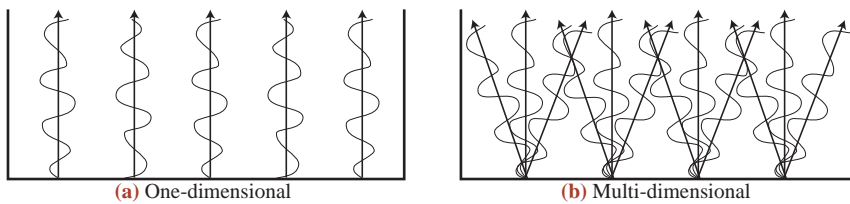


**Figure 9.17:** Wave propagation.

To examine, how the model performs when an apparent velocity is present, the calculations of Figure 9.12 and Figure 9.13 are performed again, but with an apparent velocity of  $1500 \frac{\text{m}}{\text{s}}$ . The angle of incidence, defined in Section 5.5.2, is set to  $0^\circ$ . The deformed soil body is depicted in Figure 9.18.

Similar to Section 9.6.1, the displacement time series is plotted for two surface nodes. It can be seen that the time series are very much alike, except for the time shift, caused by the apparent velocity. Some minor differences are present, but not significant, and could be due to the different damping models, discussed in Section 9.6.1. This indicates that for the present analysis, *i.e.* for a *SH*-wave shifted with a *apparent velocity* in a *stratum*, the assumption of one-dimensional wave propagation seems OK.

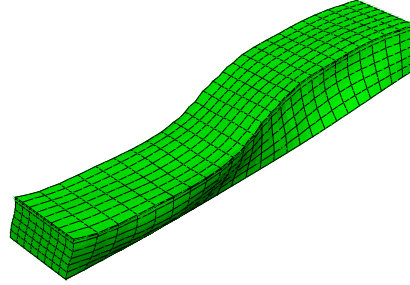


**Figure 9.18:** The deformed soil domain for  $t = 6$  s. Apparent velocity:  $1500 \frac{\text{m}}{\text{s}}$ , angle:  $0^\circ$ . An animated version of the figure is provided on the enclosed DVD.

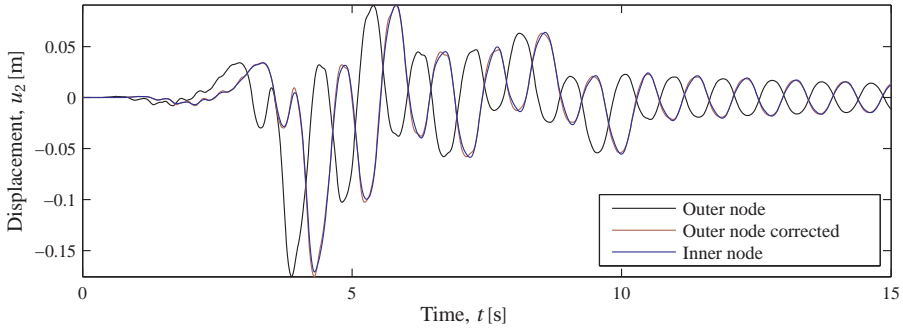


**Figure 9.19:** Displacement time series for the two nodes set off in Figure 9.11 when an apparent velocity of  $1500 \frac{\text{m}}{\text{s}}$  is applied. The red line is the outer node corrected for the time shift caused by apparent velocity. Input from DTM with hysteretic damping.

### 9.6.3 Time step

The discretization of time should be sufficiently fine to ensure that all important waves can be modelled, while still keeping computation time at a reasonable level, as it is discussed in Section 9.1.4.

To quantify the importance of the time step, the analysis of Section 9.6.2 is performed again, but with different time steps. As measure of the error made as consequence of the discretization, the data plot of Figure 9.19 is used. Correction for the apparent velocity has been made and the outer and inner node displacements are analysed, corresponding to the red and the blue line of Figure 9.19. The computational error,  $e$ , for a given time step is computed as the root-mean-square (RMS) value of the difference between each data point.

$$e = \sqrt{\frac{\sum_{j=1}^n (u_{\text{outer},j} - u_{\text{inner},j})^2}{n}} \quad (9.8)$$

where  $n$  is the number of data points. For four different time steps, the RMS error is plotted in Figure 9.20.

No clear indications of a reduced RMS error for finer time steps can be observed. This is interpreted as an indication that convergence with respect to the time step is already obtained. This is supported by the minor size of the error, approximately 2 mm.

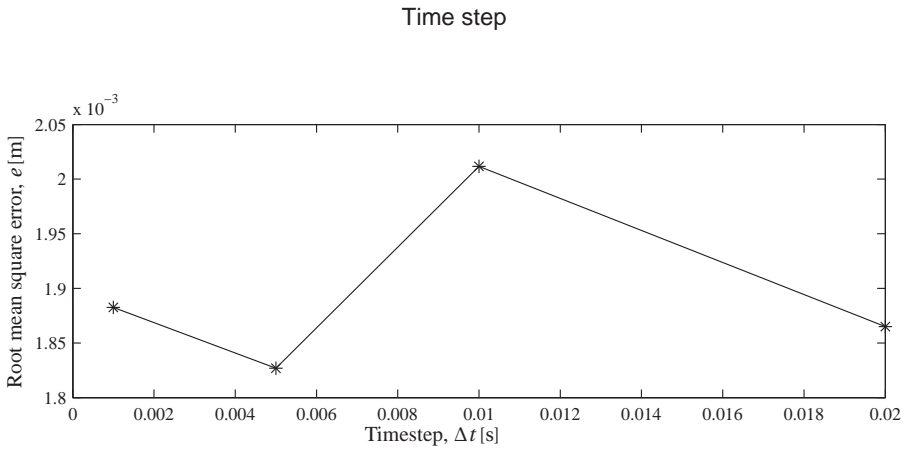


**Figure 9.20:** Influence of time step in the continuum model of the soil domain.

Even though the time step  $\Delta t = 0.01$  s provides the highest value of the error in Figure 9.20, it is chosen for the further analyses none the less, since convergence is obtained and since it provides a reasonable calculation time, cf Section 9.1.4. Furthermore, the sampling frequency of the input earthquake time series is 100Hz, corresponding to the chosen time step. Thus, every data point in the input time series is used for the analysis. This would not be the case if time steps greater than  $\Delta t = 0.01$  s were applied.



PART **III**

**ANALYSES OF METHODS AND  
PARAMETERS**



## COMPARISON OF MODELS

In this chapter, the available models are held up against each other. The closed form solution, the Winkler model and the continuum model are elaborated, and the differences between them are quantified and analysed.

### 10.1 Initial results from design basis

Firstly, the damage to the tunnel is calculated with the three different methods presented in this thesis. The basis for the calculations is the parameters discussed and presented in Chapter 5; *i.a.* an apparent velocity of  $1500 \frac{\text{m}}{\text{s}}$  and an angle of propagation of  $45^\circ$ .

As it is described in Section 5.7, the focus of the analysis will be on the opening and compression of the gaskets. Therefore, the maximal opening and compression of all gaskets are calculated. This will be the important parameters for a design of the immersed tunnel.

It can however, when comparing models, to some extent be bewildering to deal with maximal values, since the place of occurrence for the maximal value may vary. Therefore, to prepare for understanding of the model behaviour, a time series for a specific gasket corner is also presented. The chosen corner is depicted in Figure 10.1 on the following page. It is the corner of the centre gasket with the highest  $y$  and  $z$ -coordinate.

#### 10.1.1 Closed form solution

For the closed form solution, the gasket deformation is estimated with the help of (7.1) and (7.2) on page 54. The input motion data is given in Figure 7.1 and Figure 7.2 on page 55.

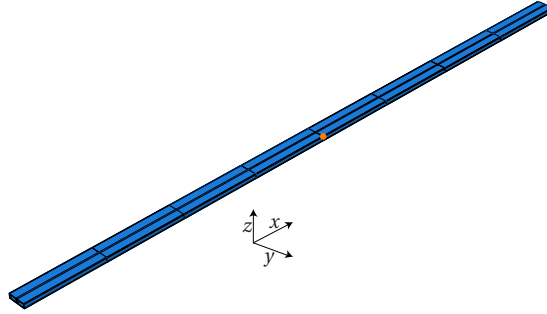


**Figure 10.1:** The gasket corner chosen for comparative output, emphasized with an orange dot.

The upper value of the deformation of a gasket,  $\Delta u$ , is calculated with the maximum absolute value of the velocity and acceleration. This is what typically will be applied in a real-world initial estimate.

$$\begin{aligned} \Delta u &= l_e \cdot \frac{v_S}{C_S} \sin \phi \cos \phi + r \frac{a_S}{C_S^2} \cos^3 \phi \\ &= 153 \text{ m} \cdot \frac{0.86 \frac{\text{m}}{\text{s}}}{1500 \frac{\text{m}}{\text{s}}} \cdot \sin 45^\circ \cdot \cos 45^\circ + \frac{34.5 \text{ m}}{2} \cdot \frac{8.01 \frac{\text{m}}{\text{s}^2}}{(1500 \frac{\text{m}}{\text{s}})^2} \cdot \cos^3 45^\circ \quad (10.1) \\ &= 47.2 \cdot 10^{-3} \text{ m} \end{aligned}$$

Due to the very simple approximation of the tunnel, the calculated gasket deformation of 47 mm does not correspond to any specific node. Likewise, since the closed form solution assumes a simple harmonic motion, the calculated deformation is both the opening and compression of the gasket.

### 10.1.2 Winkler model

The Winkler model is outlined in Chapter 8 and in the following, the results are given.

In Figure 10.2, the boundaries for the gasket deformation are depicted as function of time. Positive deformation is opening of the gasket; negative deformation is compression of the gasket. The maximum calculated opening of a gasket corner is 25.9 mm, while the maximum calculated compression of a gasket corner is  $-32.5$  mm.

For the gasket corner shown in Figure 10.1, the deformation time series is shown in Figure 10.3 on the next page. The maximum opening and compression of the corner is 24.6 mm and  $-30.6$  mm, respectively.

### 10.1.3 Continuum model

The continuum model is presented in Chapter 9. The deformed domain is depicted in Figure 10.4.

In Figure 10.5, the boundaries for the gasket deformation are depicted as function of time. The maximum calculated opening of a gasket corner is 2.49 mm, while the maximum calculated compression of a gasket corner is  $-2.35$  mm.

## Comparison

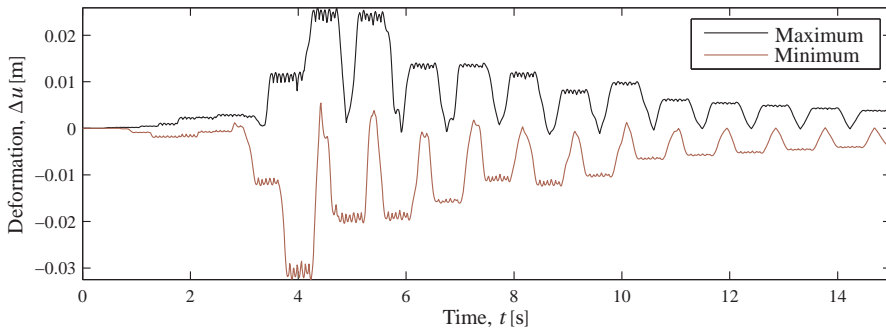


**Figure 10.2:** The Winkler model. Boundaries for the gasket corner deformation.

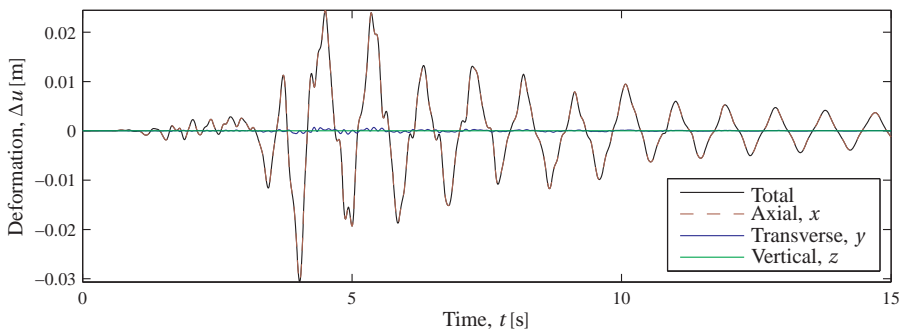


**Figure 10.3:** The Winkler model. Deformation time series for the gasket corner in Figure 10.1.

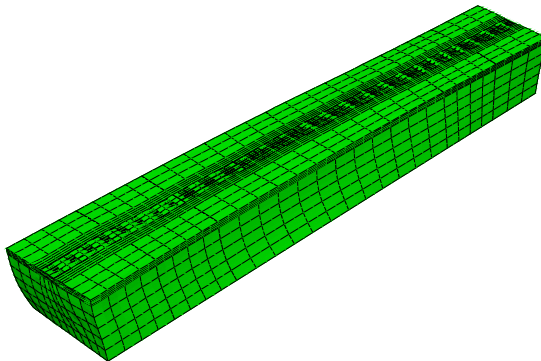


**Figure 10.4:** The deformed domain. An animated version of the figure is provided on the enclosed DVD.

For the gasket corner shown in Figure 10.1, the deformation time series is shown in Figure 10.6 on the following page. The maximum opening and compression of the corner is 2.25 mm and  $-2.11$  mm, respectively.

### 10.1.4 Comparison

In Table 10.1 on the next page, the calculated deformations for the standard parameters are listed. Firstly, it is clearly seen that the three models yield very different results.

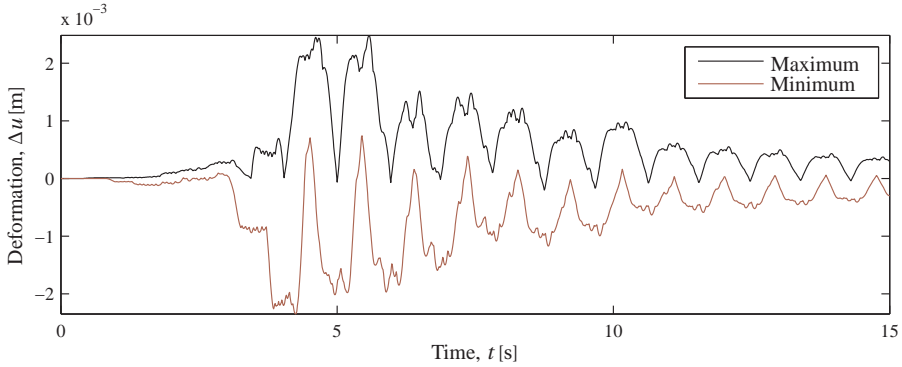


**Figure 10.5:** The continuum model. Boundaries for the gasket corner deformation.

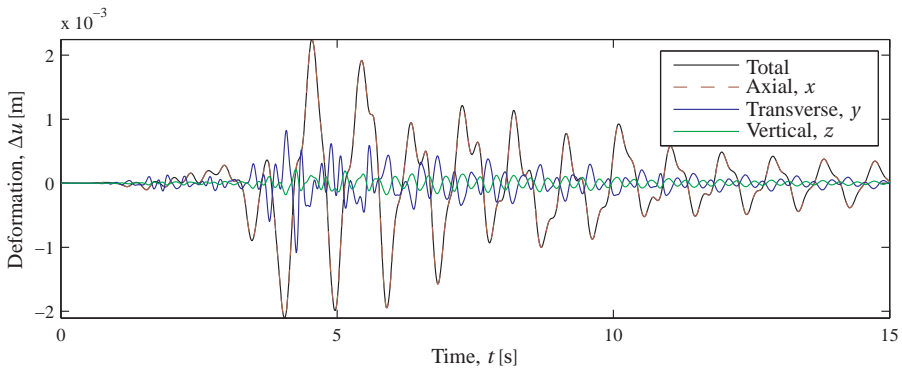


**Figure 10.6:** The continuum model. Deformation time series for the gasket corner in Figure 10.1.

The closed form solution provides nearly twice the deformation of the Winkler model, which furthermore calculates deformations of more than 10 times the deformation of the continuum model.

**Table 10.1:** The calculated gasket deformations. All deformations are in mm.

Model	Max. gasket opening	Max. gasket compression	Max. opening chosen corner	Max. compression chosen corner
Closed form solution	47.2	-47.2	47.2	-47.2
Winkler model	25.9	-32.5	24.6	-30.6
Continuum model	2.5	-2.4	2.3	-2.1

It should come as no surprise that the closed form solution provides the highest value of the gasket deformation. With this method many assumptions has been made, some of them on the very safe side. For instance, when the inertia of the system is considered, it may seem unreasonable on the safe side to use the extreme values of the velocity and acceleration as input to the closed form solution. To obtain a more accurate estimate, it could be tried to deem “equivalent” values of the input parameters  $v_s$  and  $a_s$  from Figure 7.1 and Figure 7.2 on page 55. Neither does it seem reasonable to multiply the calculated maximal strain with the tunnel length to obtain a deformation at the gasket, as it is stated in (7.2). However, it is not possible to deem a more

accurate method without further calculations.

When the simple character of the closed form solution is contemplated in relation with the complex nature of the problem, it should not cause surprise that the results differ from the more detailed calculations. In fact, the difference from the closed form solution to the Winkler model may seem minor.

In the further discussion and analysis, the primary focus will be on the difference between the Winkler model and the continuum model. The more detailed modelling of the continuum model could be expected to provide a different result, but that the gasket deformations differ with an order of magnitude may be characterized astounding.

## 10.2 The Winkler model vs. the continuum model

The great difference between the gasket deformations calculated with the Winkler model and the continuum model, shown in Table 10.1, is analysed in the following section.

### 10.2.1 Crude errors

Firstly, it should be verified that no crude errors have been made in the modelling. To this end, the displacement time series in a single node are plotted, to verify that the displacements inside the models are comparable for the Winkler model and the continuum model. The selected node is located in the gasket corner shown in Figure 10.1. In Figure 10.7, this gasket is depicted, and the selected node is shown. The node is located on *Side 1* of the gasket, defined as the the side with the lower  $x$ -coordinate.

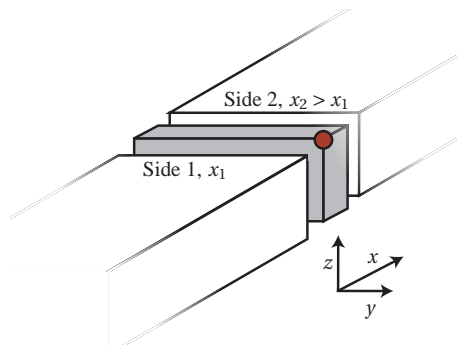


**Figure 10.7:** Definitions of sides of the gaskets. The dot marks the node plotted in Figure 10.8.

In Figure 10.8 on the next page, the displacements in the degrees of freedom of the selected node are plotted for the Winkler and the continuum model. It can be seen that the displacements are very much alike. This entails that the earthquake displacements of the Winkler model and the continuum model make the gasket corner translate in much the same way; with the *same order of magnitude*. Thus, it is rendered probable that no crude errors related to the wave propagation to the tunnel have been made in the modelling.

Furthermore, in Figure 10.8 the displacements in the vertical degree of freedom should be observed. In the Winkler model, Figure 10.8a, no displacements occur, while minor displacements are present in the continuum model, Figure 10.8b. This difference is due to the wave propagation modelled with the continuum model. The input displacements does not have any vertical component (since a SH-wave is assumed), and in the Winkler model this is directly transferred to the tunnel, while the waves in the continuum model are propagated with respect to the three-dimensional domain.

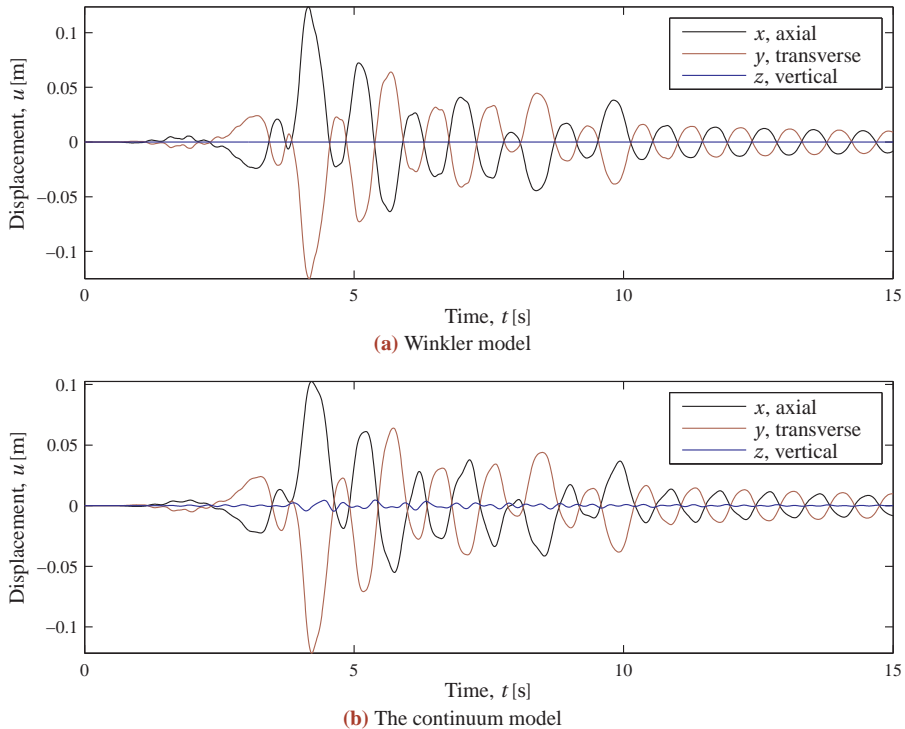


**Figure 10.8:** Displacements in the degrees of freedom at the corner shown in Figure 10.1.

## 10.2.2 Three-dimensional wave propagation

In the Winkler model the wave propagation is assumed to be one-dimensional, whereas the waves in the continuum model have the ability to propagate three-dimensionally. The consequence of this is analysed in Section 9.6.2, where it is shown that in the present case, this effect does not yield any significant importance in the results.

## 10.2.3 Deformation in gasket

Apparently, the orders of magnitude of the displacements correspond well to each other in the Winkler and the continuum model, but the deformations in the gaskets differ with an order of magnitude. Therefore, the deformation in the gasket depicted in Figure 10.1 and Figure 10.7 is analysed further.

The deformation in the corner of the gasket has been plotted in Figure 10.3 and Figure 10.6. When the deformations in the respective directions are contemplated, it can be seen that in both models, the deformation in the axial direction dominates most heavily. Some transverse deformation is calculated in the continuum model, but the total three-dimensional deformation depends almost exclusively on the axial deformation. This was also to be expected, since deformations perpendicular to the tunnel axis – due to the geometry – does not contribute very much to the change in distance between the corner nodes.

### Transverse and vertical deformation

In Figure 10.9, the transverse and vertical deformations of Figure 10.3 and Figure 10.6 are plotted together. It can be seen that all though the calculated displacements in no way are the same, the orders of magnitude correspond well to each other. Hence, the major difference between the Winkler and the continuum model apparently is to be found in the axial deformation.

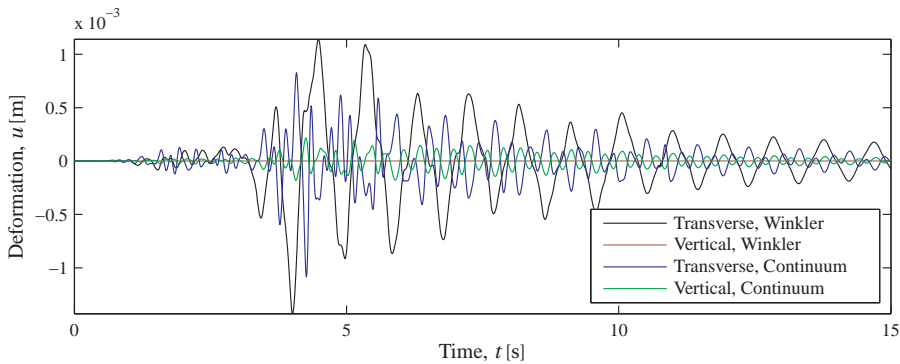


**Figure 10.9:** Transverse and vertical gasket deformations of Figure 10.3 and Figure 10.6.

### Translations and rotations in gasket centre

To examine which tunnel deformation mode causes the axial gasket deformation in the two models, the gasket deformation is now expressed in terms of the degrees of freedom for the tunnel beam, *i.e.* rotations and translations in the gasket centre. For the Winkler model, the degrees of freedom are given as the direct output, while they must be calculated for the continuum model. The problem is sketched in Figure 9.9 on page 77, and the calculation is outlined in Section 9.5.2.

The deformations are calculated as the difference in the displacements of the degrees of freedom between side 1 and side 2 of the gasket, cf. Figure 10.7. The translational degrees of freedom are plotted in Figure 10.10 on the next page, while the rotational degrees of freedom are plotted in Figure 10.11 on page 95. For the rotational degrees of freedom, the rotations are converted into displacements in the tunnel axial direction. Hence, the rotation about the  $x$ -axis, so-called *roll*, is not plotted, since this does not provide  $x$ -axial displacement.

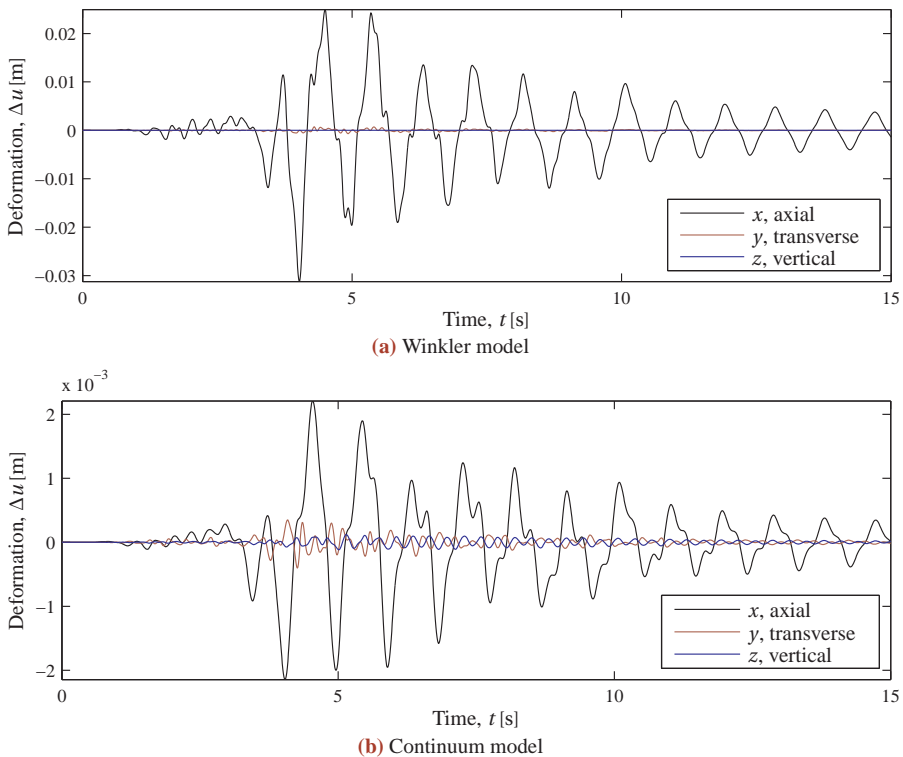


**Figure 10.10:** Translational deformation for the gasket centre.

By studies of Figure 10.10 and Figure 10.11, it is again seen that the  $x$ -axial translational degree of freedom provides nearly all the deformation of the gasket. This is common to the two models. Furthermore, in both models the rotation about the vertical axis yields only approximately 10% of the axial deformation. Thus, only axial deformation and *not* bending of the tunnel governs the gasket damage during the present earthquake.

### Gasket approximation

The Gina gasket in the Winkler model is represented with three springs, as it is sketched in Figure 8.11 on page 63. Hence, no rotational stiffness is present in the Winkler model. Still, the bending deformation comprises under 10% of the gasket deformation, whereby it can be concluded that the modelling of the Gina gasket with a single spring should be sufficient, since a more sophisticated modelling solely will increase the rotational stiffness.

#### 10.2.4 Importance of retroaction

In the preceding, it has been shown that the major difference between the Winkler model and the continuum model should be sought for in the axial deformations. One of the major principal differences between the models is that the soil springs in the

## Importance of retroaction

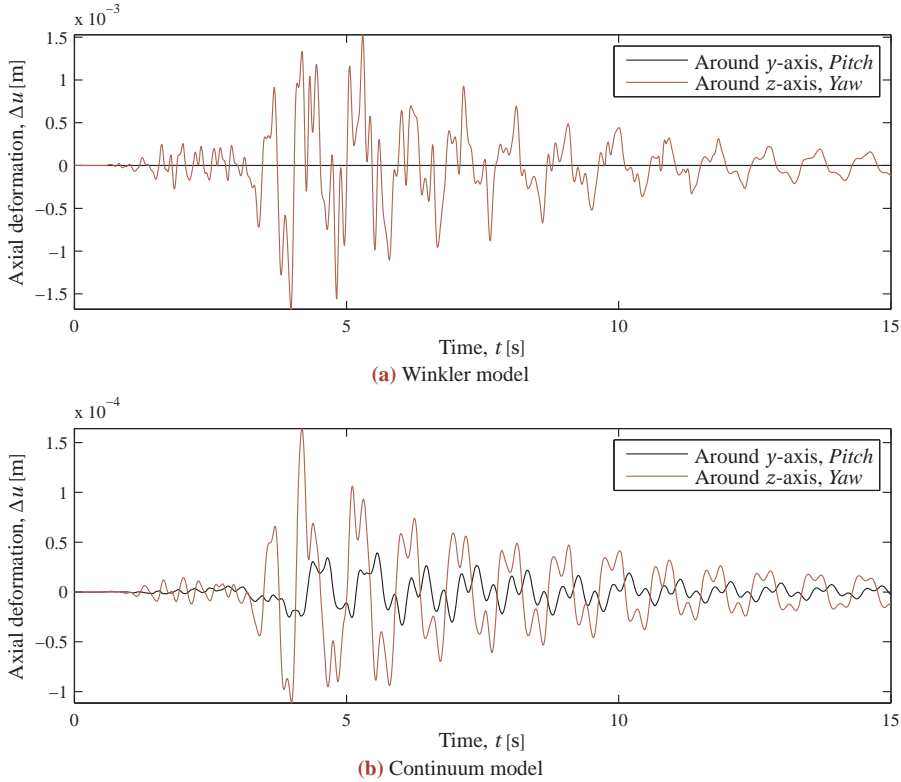


**Figure 10.11:** Axial deformation due to rotations in the gasket centre.

Winkler model are decoupled, *i.e.* that the only connection between two adjacent soil springs is the tunnel.

The two models are sketched in Figure 10.12, where it can be seen that the only thing which couples two adjacent springs is the shear stiffness of the tunnel. This opposes to the continuum model, where the soil elements around the tunnel are coupled, making retroaction possible, *i.e.* waves can be reflected from the tunnel back to the soil elements, and the soil-structure interaction is dependent on the adjacent strain state.

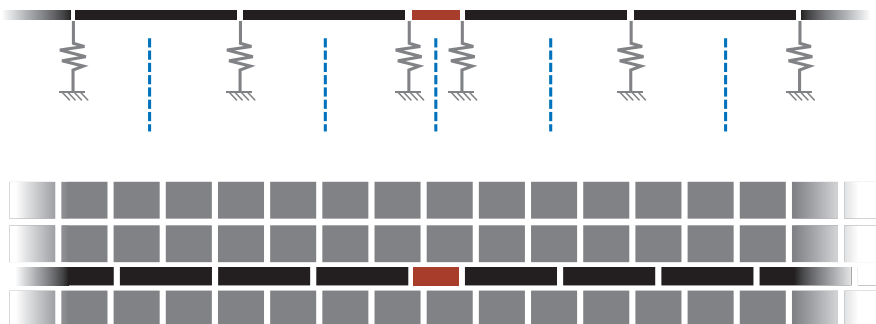


**Figure 10.12:** The Winkler model (topmost) and the continuum model. The gaskets are coloured red, the tunnel black, and the soil grey. The blue dotted lines indicate that no retroaction is possible in the Winkler model.

This difference between the two models is not easy to eradicate. It should be clear that the continuum model in this respect is the better estimate of the physical problem. To incorporate retroaction in the Winkler model, a soil element with appropriate parameters could be connected to the tunnel, as it is sketched in Figure 10.13. The soil element should model the soil behaviour, and its parameters could include both various stiffness's, damping and mass. This should be able to provide a better model representation. However, the determination of the soil element parameters is far from trivial, and it has not been investigated further in the present thesis.

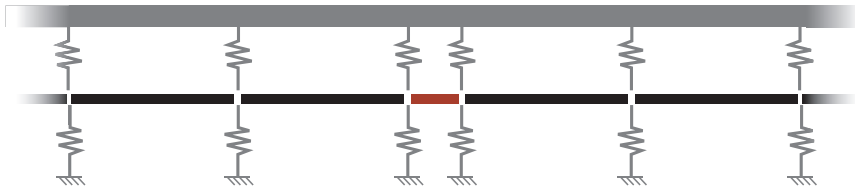


**Figure 10.13:** The Winkler model of Figure 10.12 fitted with a soil element to account for retroaction. The input displacements should still be applied to the lower springs. Only vertical soil springs are depicted.

Instead, the consequence of removing the retroaction possibility in the continuum model has been analysed. This should illustrate the sense of retroaction modelling. In the preceding, the deformations analysed are in the gaskets and therefore, the retroaction possibility has been removed over the gaskets. Since the tunnel elements are very stiff compared to the gaskets, it is also deemed that the effect of removing the retroaction possibility will be greatest there.

### Separation planes

To take away the possibility of retroaction, separation soil planes have been implemented in the continuum model in the gasket planes, as it is sketched in Figure 10.14. The elements in the separation planes are modelled without stiffness and mass, thus removing all ability to transfer any force or displacement. Hence, the continuum model imitates the behaviour of the Winkler model, as it is sketched in Figure 10.12. However, the element surfaces outlined with a green line in Figure 10.14 will be modelled with a “free” surface, thus making the soil too flexible. This should be remembered when interpreting the results of the analysis.



**Figure 10.14:** Insertion of a separation plane into the continuum model of Figure 10.12. The blue soil elements have no stiffness or mass, and the green line indicates elements with a “free” surface.

## Spring planes

The deformed domain is depicted in Figure 10.15, where the separation layers clearly can be observed.

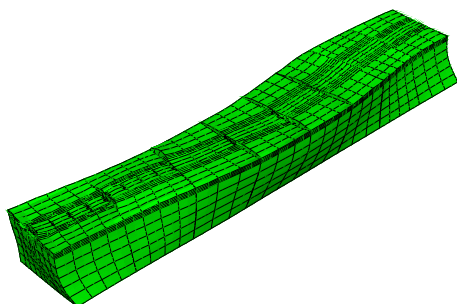


**Figure 10.15:** Deformed domain for an analysis with separation planes. An animated version of the figure is provided on the enclosed DVD.

The deformation for the chosen gasket corner (Figure 10.1) is plotted in Figure 10.16. It can be seen that the deformations have been dramatically increased when compared to Figure 10.6. The total deformation has been increased approximately 30 times, and even more for the vertical deformation. Due to the “free” surfaces in the gasket cross sections, the gasket deformation now is more than twice the deformation calculated in the Winkler model.

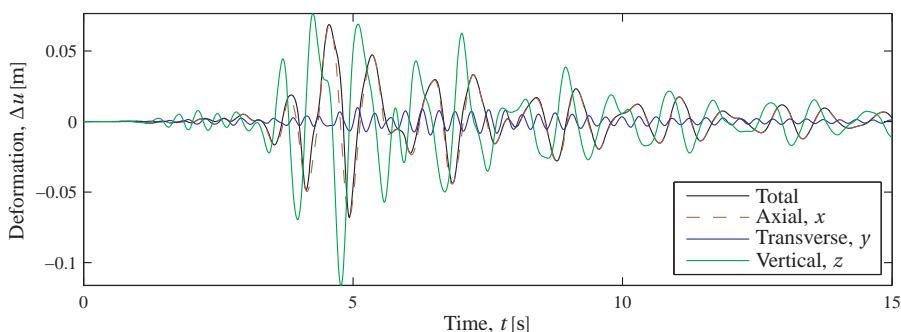


**Figure 10.16:** Deformation time series for the gasket corner in Figure 10.1. The continuum model with separation planes. The maximum opening and compression of the corner is 68.7 mm and -68.2 mm, respectively.

## Spring planes

Apparently, the connection of the soil over the gaskets is of very high importance. To further investigate the phenomenon, a different approach for modelling of the separation planes is made. In Figure 10.17 on the following page, four different modellings are sketched. Subfigure (a) shows the modelling without separation planes and (d) illustrates the already performed analysis with no stiffness in the separation planes.

To analyse whether it is the normal stiffness or the shear stiffness which is of importance in the separation layers, (b) can be used as modelling, disregarding only the shear stiffness. Furthermore, to investigate the importance of the normal stiffness in the tunnel-axial direction, the horizontal springs are omitted in (c).

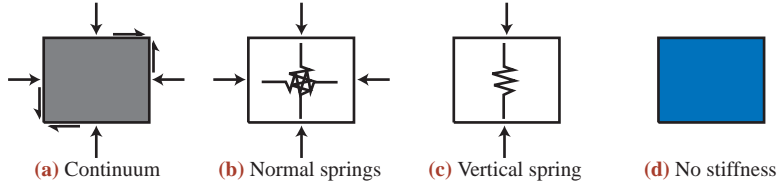
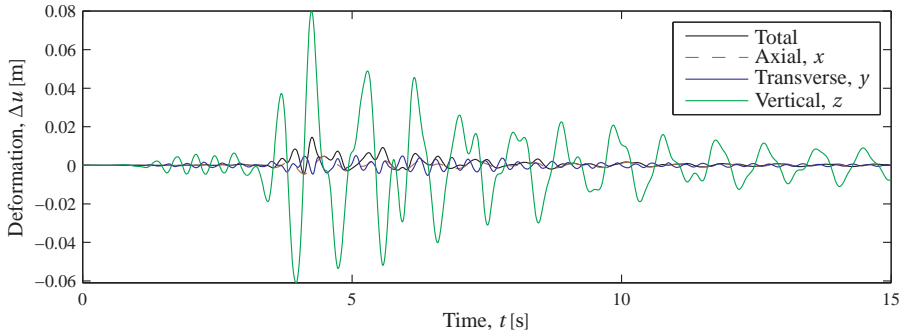
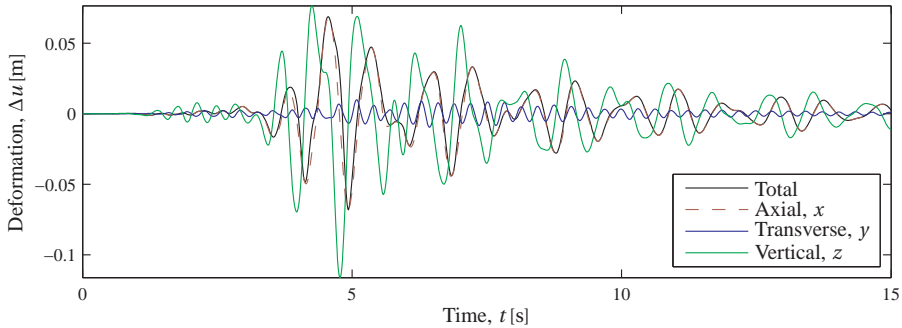


**Figure 10.17:** Different ways of modelling the separation plane elements. The arrows outside the elements illustrate the stresses which can be applied to the elements.

The analysis of the two new separation plane models yields the results plotted in Figure 10.18. In Figure 10.18b, the absence of shear stiffness in the separation plane has increased the total opening from 2 mm to 14 mm. The vertical deformation has increased much more, since very little stiffness in this direction is in the model. As the axial spring in the separation plane is removed, the deformation raises to the level of the separation plane without stiffness. This can be seen in Figure 10.18b, which in every aspect is nearly identical to Figure 10.16



**(a)** Normal spring separation planes, cf. Figure 10.17b. The maximum opening and compression of the corner is 14.4 mm and  $-4.5$  mm, respectively.



**(b)** Vertical spring separation planes, cf. Figure 10.17c. The maximum opening and compression of the corner is 68.7 mm and  $-68.2$  mm, respectively.

**Figure 10.18:** Deformation time series for the gasket corner in Figure 10.1.

It is clearly seen that the more important property for the separation layer is the stiffness in the tunnel-axial ( $x$ -axial) direction. If the stiffness disappears, the model’s ability to take retroaction into account disappear fully, and this increases the gasket deformation dramatically.

On the basis of the performed analysis, it is deemed that the presence of  $x$ -axial stiff-

ness in the soil next to the gaskets is the single most important reason for the major difference between the results from the Winkler and the continuum model.

But still, the results with the modellings of Figure 10.17 are not very close to the results obtain with the Winkler model. The reason for this is that the introduction of a “separation layer” also entails introduction of a “free” surface, as it is discussed in the above and depicted in Figure 10.14. Nevertheless the performed analysis very significantly spots the importance of incorporating the possibility of retroaction into the calculation models.

### 10.2.5 Modelling without gaskets

Apparently, the presented Winkler model does not perform well with the immersed tunnel of the present thesis, since it fails to model the single most important factor in the soil-structure interaction: the retroaction in the tunnel-axial direction.

However, Winkler models are widely applied. The major flaw in the present application is deemed to be the segmentation of the immersed tunnel; *i.e.* the cross section is not uniform, since the very flexible gaskets separate the tunnel elements. Thus, the minor errors are lumped in the gaskets, making the result unusable.

To test the Winkler model’s performance for a uniform cross section, the gaskets in the models have been removed and replaced by concrete finite elements, thus making the immersed tunnel consist of only one single tunnel element. The deformation in the point shown in Figure 10.1 is still used for the calculation, and the time series are shown in Figure 10.19 on the following page.

It can be seen that the deformation time series are very alike for the Winkler and the continuum model if the gaskets are removed. Thus, the Winkler model is a good model for dynamic analysis of underground elongated structures, if the cross section is uniform. The gaskets of the immersed tunnel makes the model overly conservative in the gasket deformation calculations.

The similarity of the plots in Figure 10.19 also verifies the model coding of both the Winkler model and the continuum model.

Even though the Winkler model in this chapter has been shown to yield results very different from the continuum model with respect to the deformation of the gaskets, the model will still be used together with the continuum model in the following. This is done in order to examine, whether the much simpler Winkler model could be workable for parameter studies.

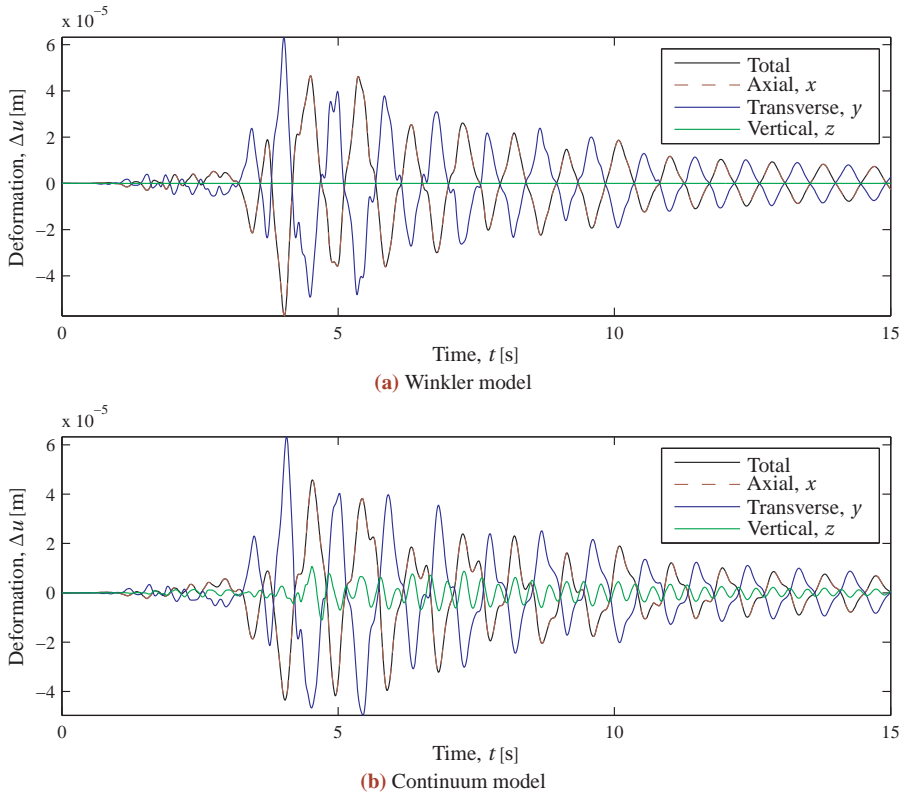


**Figure 10.19:** Deformation time series for the point in Figure 10.1. The gaskets are replaced by concrete finite elements.

### 10.3 Winkler soil springs

The determination of the soil springs in the Winkler model is described in Section 8.2.1. The soil spring stiffness's are determined on the basis of an elastic model, thus making the results comparable to the continuum model. If a different material model was applied (*e.g.* to account for non-linear behaviour), if the stratification of the project site was different, or simply if the material stiffness parameter should be determined to something different, the soil spring stiffness's could vary.

To account for the influence of the magnitude of the soil spring stiffness's, a sensitivity analysis have been performed. The soil spring stiffness's have been scaled with different common factors and the resultant maximal gasket deformation has been calculated. For stiffness scales from 0.1 to 10, the result is plotted in Figure 10.20 on the next page.

It can be seen that for moderate variations of the soil spring stiffness's,  $\pm 50\%$ , the gasket deformation only varies with around  $\pm 15\%$ . Thus, the soil spring stiffness's can be determined with some scatter without comprising the accuracy of the Winkler model. However, if changes in the soil spring stiffness should be due to changes in the general soil stiffness, and hence changes in the wave velocity in the soil, the free-field soil response will change significantly cf. Section 11.3 on page 106.

## Prestress in tunnel

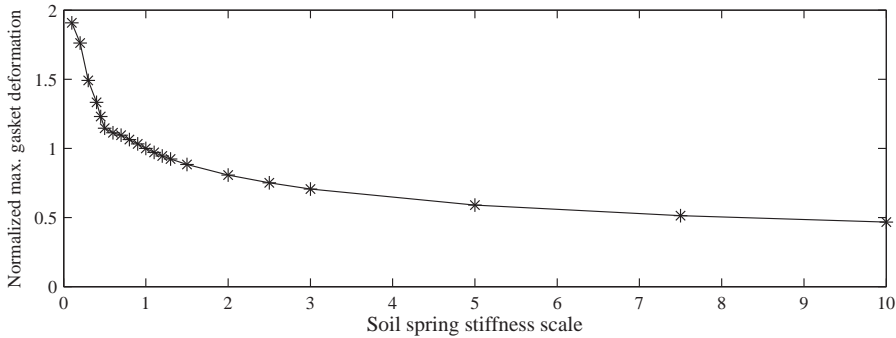


**Figure 10.20:** The frequency response function for other depths of layer C.

In Figure 10.20 it can further be observed that the gasket deformation decreases monotonous with increasing soil spring stiffness. This was also to be expected, since an increasing soil spring stiffness will make the tunnel follow the prescribed displacements more closely, and the deformation will decrease towards a minimum specified by the apparent velocity.

## 10.4 Prestress in tunnel

As described in Section 5.6.1, the tunnel elements are prestressed during the installation phase. The purpose of the prestress is to compress the Gina gaskets, but the induced stresses in the system could also affect the stiffness of the tunnel elements, as it is known from an ordinary beam-column problem. An axial compressive stress will reduce the bending stiffness against cross axial load.

The prestressing force cannot be neglected offhand, since the total force is of magnitude 48 000kN, cf. (5.13). However, in the present chapter it is repeatedly shown that the axial compression of the immersed tunnel is far more significant than bending. Thus, it is deemed that prestress in the tunnel will have negligible influence on the tunnel damage. To support is assumption, a sensitivity analysis has been carried out.

The bending stiffness have been scaled by a varying factor, by scaling of the cross sectional second moments of area,  $I_y$  and  $I_z$ . In Figure 10.21 on the next page the maximum deformation has been plotted for the reference gasket corner.

It can be seen that the gasket deformation is very insensitive to variations in the bending stiffness of the tunnel elements – only a slight decrease in the deformation occurs from increasing bending stiffness. This can be explained by two characteristics of the system, which has also been verified in the above: 1) the axial deformation is of much greater importance than bending of the tunnel, and 2) since the gasket stiffness is much less than the tunnel stiffness – even if the the bending stiffness of the tunnel is scaled – the free-field soil displacements are lumped in the gaskets.

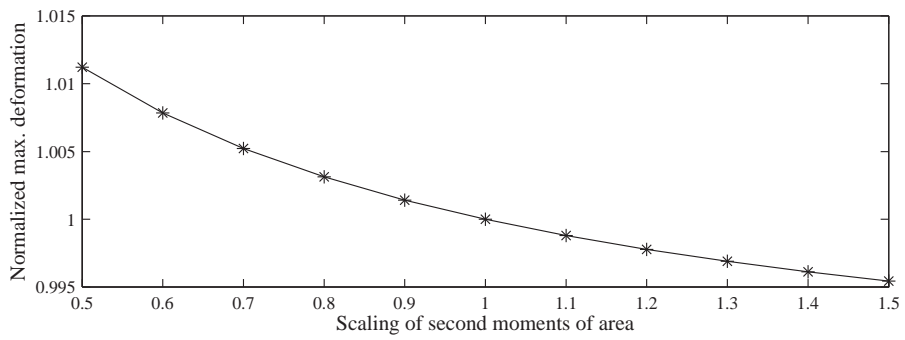


**Figure 10.21:** Sensitivity of the tunnel element bending stiffness. Normalized deformation in the gasket corner in Figure 10.1.

## SOIL PARAMETERS AND STRATIFICATION

In Chapter 5 the soil stratification and the soil parameters for the project are presented, and in Section 6.5 the response at the level of the tunnel is calculated by means of the domain transformation method. In this chapter the sensitivity of the soil response with respect to changes in the stratification and in the soil parameters is analysed.

The purpose of the sensitivity analyses are to indicate, how much time and money should be spend in the determination of the stratification and soil parameters. If the soil response is insensitive to changes in *e.g.* the layer thickness, only minimal soil investigation is needed. On the other hand, if great sensitivity is present, it may be favourable to invest time and money in detailed soil investigations.

### 11.1 Method of analysis

In the following analyses of this chapter, the sensitivity parameter is chosen as the maximum absolute soil response from the time series at the level of the tunnel, calculated with the domain transformation method. For the reference response calculated with the parameters given in Chapter 5, this value is 175 mm cf. Figure 6.12 on page 50. The data of the plots in this chapter have been normalized with this value. For comparison, the maximum absolute displacement of the earthquake time series is 95.5 mm cf. Figure 5.7.

The choice of this sensitivity parameter is made because it is well correlated to the deformation in the gasket, which is the final design parameter cf. Section 5.7 on page 38. Therefore, there is no need to perform excessive calculations to determine the final gasket deformation for these sensitivity analyses. The correlation has been verified in Section 12.3, where it has been shown that because the models are linear, the gasket deformations are directly proportional to the free-field soil response.

Even though the maximum absolute displacement may not be a perfect representation of a time series – since all other soil response data is not used for the sensitivity analyses – it can be seen by comparison of *e.g.* Figure 6.12 on page 50 and Figure 10.5 on page 90 that the maximum gasket deformation occurs as the immediate reaction to the maximum soil response. Thus, the maximum absolute displacement may with good accuracy be used as indirect indication of the tunnel damage.

If the layer interfaces are not horizontal and the stratification similar at the entire project site, incoherence may arise cf. 4.11c on page 26. This type of incoherence has not been analysed in the present thesis, as it is stated in Section 4.6. Since the analyses of the wave propagation is purely one-dimensional it would not make much sense to make detailed studies with these methods, as the wave propagation will be three-dimensional for varying stratification.

The exact sensitivities calculated will vary for different earthquakes with varying frequency spectra. However, the following analyses should nevertheless provide clear indications of the important factors.

## 11.2 Impact of layer depths

The stratification may not be very well determined in the deeper subsoil, since deep borings are very expensive.

In Figure 5.1 on page 28 the stratification for the longitudinal section is depicted. It can be seen that the layer thicknesses vary over the tunnel. In Section 5.4 it is shown how mean thicknesses have been chosen as the design basis for the entire domain. Thus, the geographic variations are not included in this thesis. In this section, the consequences of different thicknesses for the soil layers have been analysed.

### 11.2.1 Thickness of layer A

The maximum displacement at the level of the tunnel as function of the thickness of layer A is plotted in Figure 11.1. Only minor sensitivity is present, since it can be seen that if *e.g.* the layer vanishes, the displacement amplitude increases by around 1%.

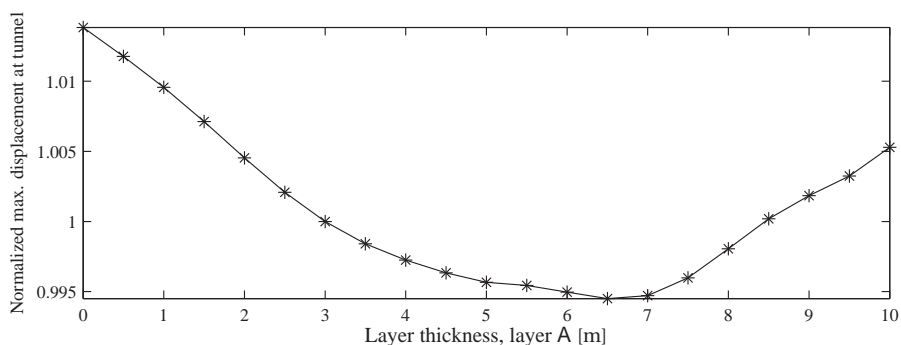


**Figure 11.1:** Influence of the thickness of layer A.

### 11.2.2 Thickness of layer B

The sensitivity of the displacements with regard to the thickness of layer B is plotted in Figure 11.2. The deformation may be increased with up to 7%, should the layer vanish.

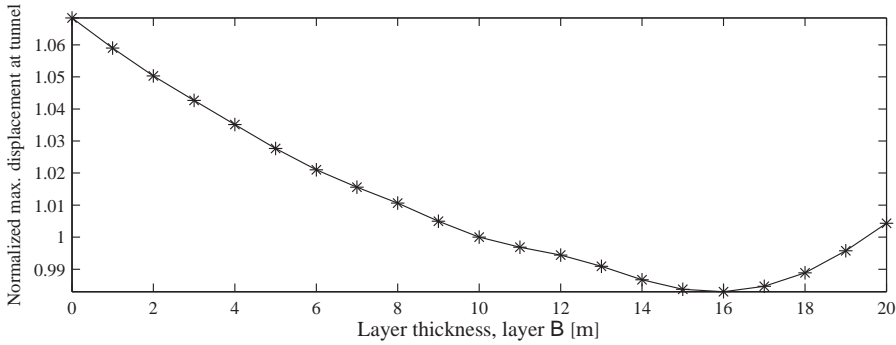


**Figure 11.2:** Influence of the thickness of layer B.

### 11.2.3 Distance to bedrock

In (COWI 2007) the thickness of layer C is estimated to 100 – 150 m as mentioned in Section 5.2. Since the thickness of the layer, *i.e.* the distance to the bedrock, is not well determined, the consequences of different thicknesses for layer C has been analysed. The result is plotted in Figure 11.3.

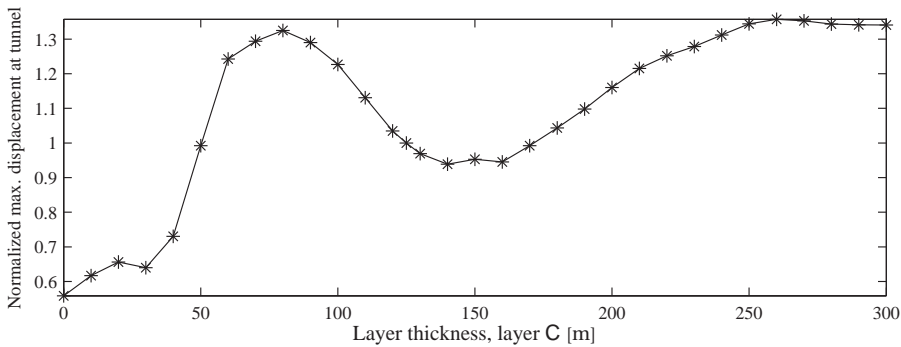


**Figure 11.3:** Influence of the thickness of layer C.

It can be seen that rather large sensitivity is present. Should the lower value of the estimated interval, 100 m, be the correct value of the layer thickness, the soil displacement is magnified with 20%. Even a magnification of approximately 30% is possible if the correct value should be 80 m.

In general, it can be concluded that the stratification is of rather high importance for the calculated displacements at the level of the tunnel. In a real-world design process, the exact stratification will never be known. Therefore, care should be taken when determining the stratification, and for a final design sensitivity analyses like the

above should be performed, and the design stratification chosen from the maximum displacement. Also, if the layer interfaces diverges significantly from being horizontal, this must be taken into consideration.

### 11.3 Wave velocity

The wave velocity depends on the shear stiffness and the density of the soil, as given by (A.4) on page 130. Therefore, the result for a sensitivity analysis of the wave velocity also applies for the soil shear stiffness and the soil density.

The sensitivities for varying wave velocities are plotted in Figure 11.4. Like it is discussed for the layer thicknesses, it can be seen that the design wave velocity can not be chosen on the safe side as an upper or lower value. Especially for layer C the wave velocity is significant, and magnifications of the displacements may be as high as 30% for a 30% increase in wave speed. For a final design, the expected interval of the wave velocities should be determined, and sensitivity analyses performed to determine the maximum displacement.

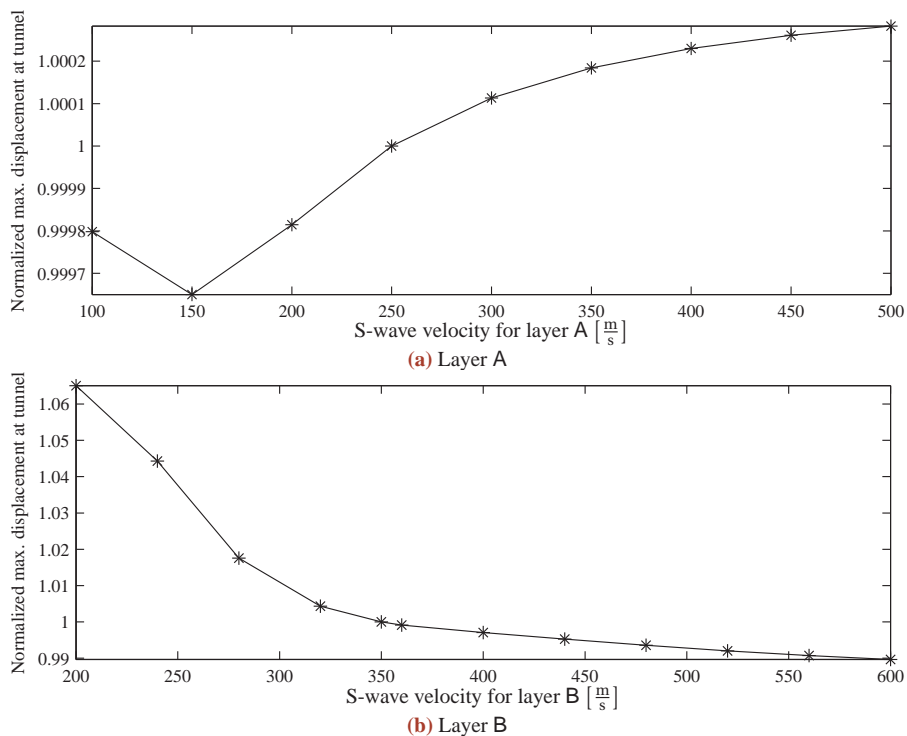


**Figure 11.4:** Influence of the wave velocity of the soil layers.

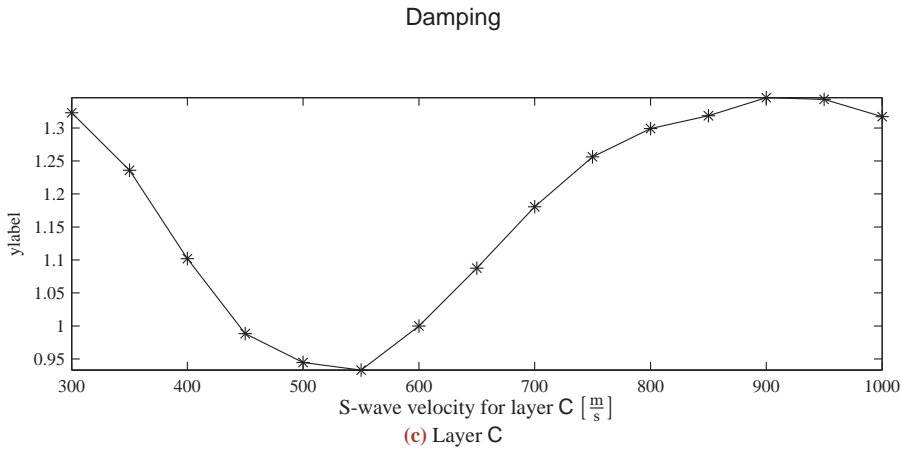


**Figure 11.4:** Influence of the wave velocity of the soil layers (Continued).

## 11.4 Damping

The application of damping in the thesis is outlined in Section 5.3. Here, the consequences are analysed.

### 11.4.1 Sensitivity

The sensitivity of the soil response with respect to the loss factor of the soil layers is plotted in Figure 11.5. Due to its greater thickness, layer C is the only layer showing a significant sensitivity. In general, it can be observed that more damping generates less soil response, as it would also be intuitively expected. However, it may be seen that the sensitivity of the the soil response is very little, since only up to 3% of the displacement fades for moderately high damping of soil C,  $\eta = 0.1$ .

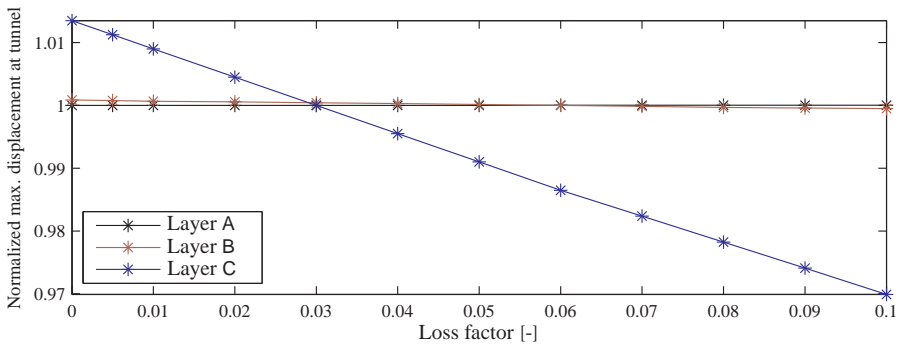


**Figure 11.5:** Influence of the damping loss factor  $\eta$ .

The effect of damping can also easily be seen in the frequency response function which is plotted in Figure 11.6. Especially the response in the eigenmodes is significantly damped.

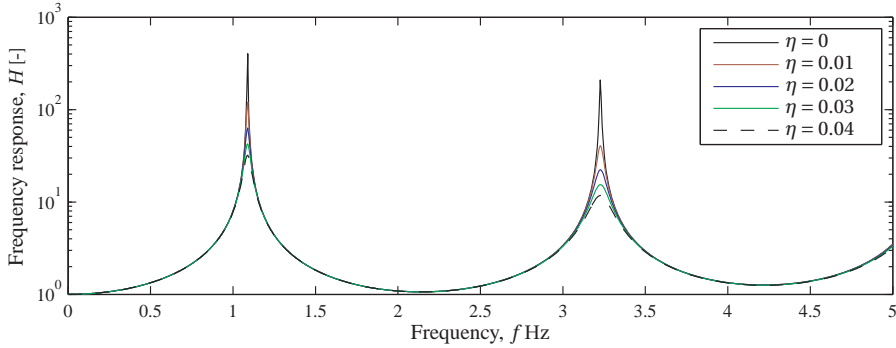
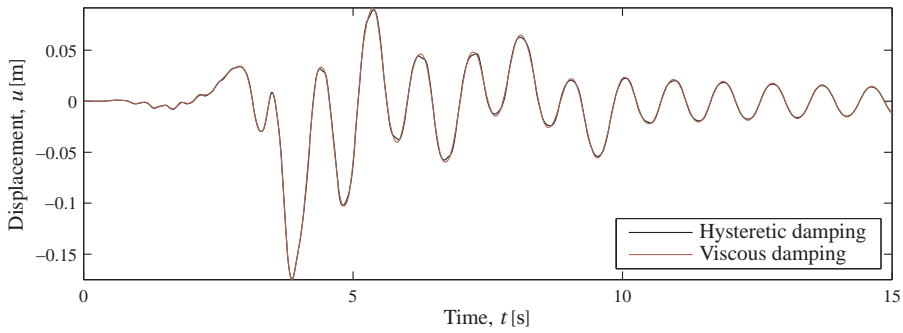


**Figure 11.6:** Frequency response function for the stratum at the level of the tunnel.

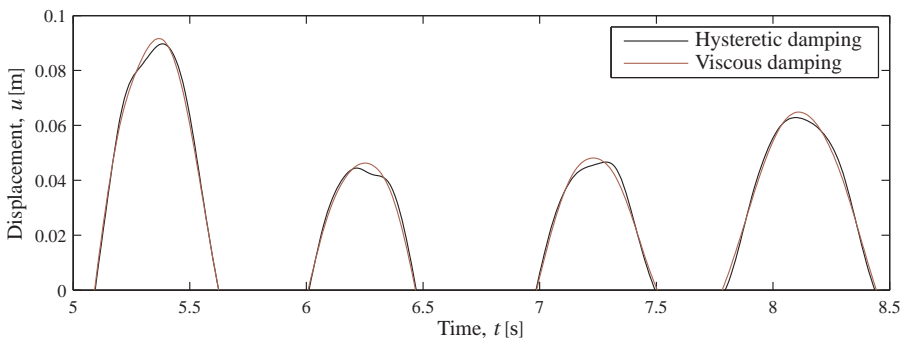
### 11.4.2 Hysteretic damping and viscous damping

Both hysteretic damping and viscous damping have been integrated in the domain transformation method, and two time series at the level of the tunnel have been calculated in the frequency domain and plotted in Figure 11.7 on the next page. It can be seen that very little difference exists between the two damping mechanisms. This was also the conclusion in Section 9.6.1, where the time series calculated with hysteretic damping has been applied to the continuum model, whose solution in the time domain entails application of viscous damping. In fact, it can be seen that the plot of Figure 11.7 is very similar to Figure 9.15 on page 80. This indicates that the coding of damping in the continuum model and the domain transformation method yields very similar results, thus verifying the coding of both models.

## Hysteretic damping and viscous damping



(a) Time series for the first 15 s



(b) Close-up

**Figure 11.7:** The soil response at the level of the tunnel. Viscous damping has been calibrated for the hysteretic damping at a frequency of 1.09 Hz.



## THE EARTHQUAKE

In this chapter sensitivity analyses are performed for the apparent velocity, the direction and the displacement amplitude of the earthquake.

The damage measure is for the continuum and the Winkler models chosen to the deformation of the gasket corner depicted in Figure 10.1. This is chosen instead of the maximal deformation at all gasket corners, since a comparison is deemed to be more appropriate and understandable when a specific node is used. For the closed form solution, only a single gasket deformation value exists.

### 12.1 Apparent velocity

Firstly, the sensitivity of the damage to the tunnel with respect to the apparent velocity is analysed. Different values of the apparent velocity have been used for simulations in the continuum model, and the maximum opening and compression of the gasket corner shown in Figure 10.1 has been plotted in Figure 12.1a. Even though the Winkler model and the closed form solution in Chapter 10 has been shown to be unreliable for the immersed tunnel, calculations with the Winkler model and the closed form solution have also been made, due to the simple formulations. The results are plotted in Figure 12.1b. The ease of making parameter studies with the Winkler model and the closed form solution, which is coded by hand in MATLAB, is the reason for the additional data.

Even though the models in Figure 12.1 do not yield the same results, a similar trend is clearly shown. The similarity between the models is further outlined in Figure 12.2 on page 113, where the results of Figure 12.1 are plotted for the three models together.

It can be seen that changes in apparent velocity of  $\pm 500 \frac{\text{m}}{\text{s}}$  yield changes in the gasket deformation of around  $\mp 20\%$ . Since the greater damage occurs for lower values of the

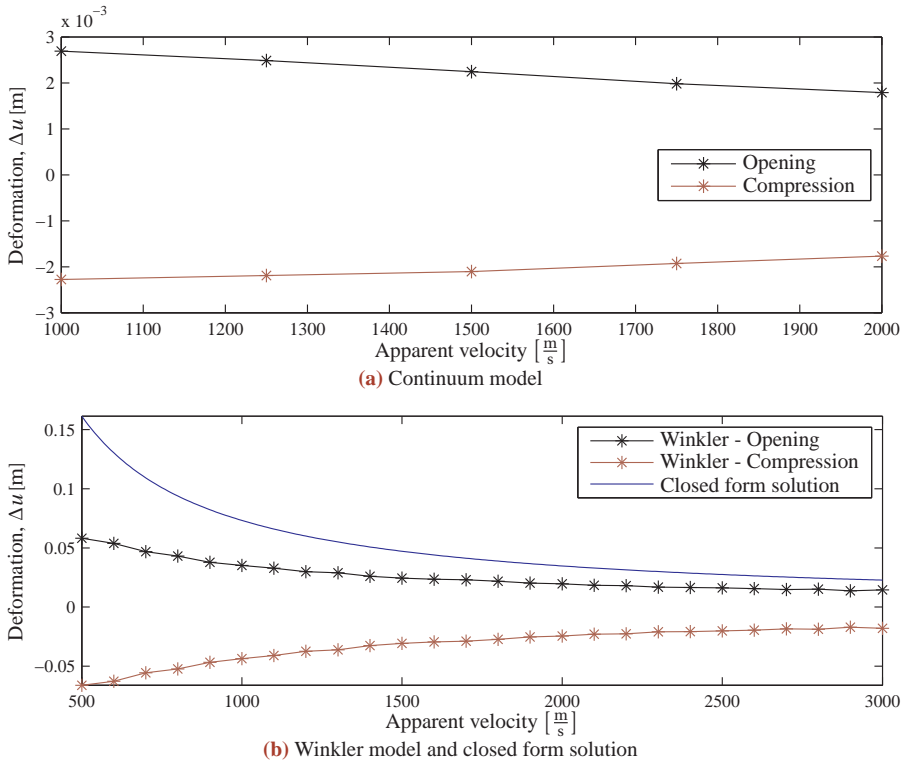


Figure 12.1: Maximum deformation in gasket corner shown in Figure 10.1.

apparent velocity, the lowest reasonable value should be used for a final design.

It does seem very reasonable that the general trend is increasing apparent velocity for decreasing damage of the tunnel, since the incoherence stems from the apparent velocity, and the incoherence is closely related to the damage of the tunnel, as it is discussed in Section 4.6. However, in a dynamic analyses it could normally be expected that certain eigenmodes of the system would be excited from certain apparent velocities. Thus, a decreasing tendency could be expected, but some local amplification would not be surprising to observe.

In Figure 12.2 however, the deformation is decreasing monotonously with increasing apparent velocity. The reason for this must be found in the discussion of Section 4.4; that the behaviour of an underground structures is not dominated by the inertia of the structure. Hence, the most important seismic parameter for underground structures is not the soil acceleration but the soil displacement, and the eigenmodes of the immersed tunnel become of minor importance.

## Direction

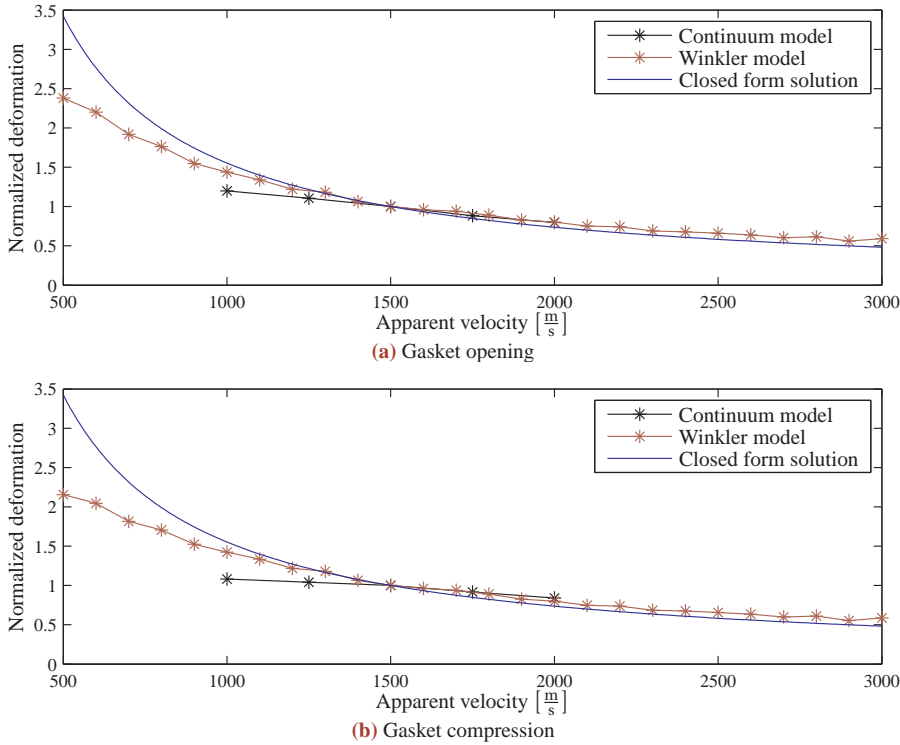


**Figure 12.2:** Results from Figure 12.1 with deformation normalized for an apparent velocity of  $1500 \frac{m}{s}$ .

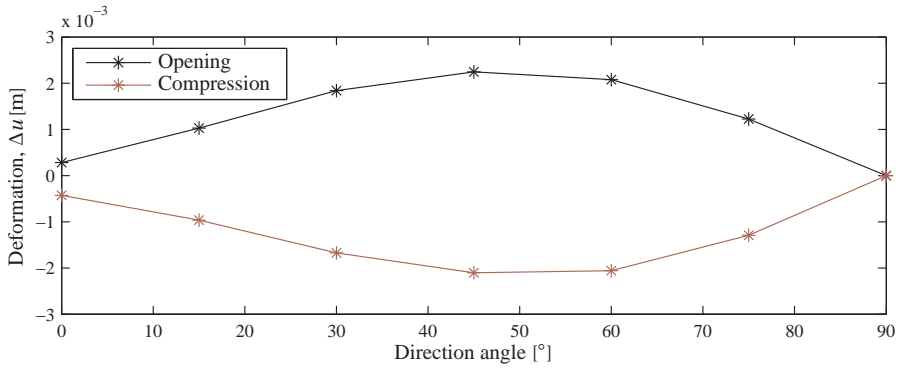
## 12.2 Direction

Similar to the previous section simulations have been performed, now with varying angle of direction. Since the system is double symmetric, only angles from  $\theta = 0^\circ$  to  $\theta = 90^\circ$  are used for the analysis. The definition of the angle is provided in Figure 5.9 on page 35.

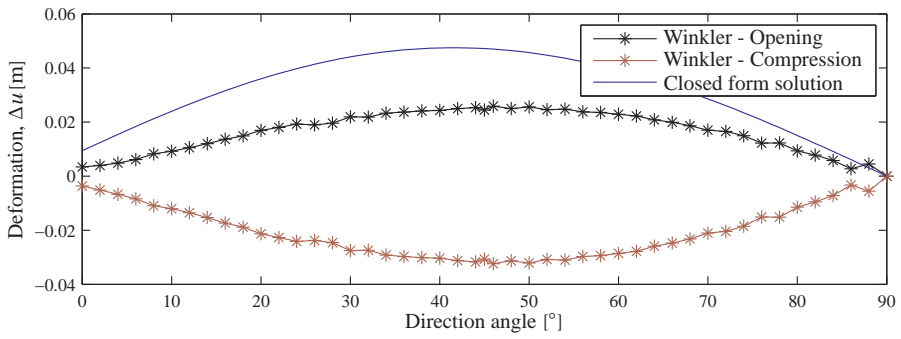
The gasket opening and compression as function of the angle of propagation are depicted in Figure 12.3 for the continuum model, the Winkler model, and the closed form solution. It is clearly seen that the maximal gasket deformation occur with a direction angle of approximately  $45^\circ$ . Thus, as it was deemed in Section 5.5.3, the critical angle of approach is oblique, where both axial particle motion, cross axial particle motion and an appropriate incoherence are present.

It should be noted that the calculated deformation is  $\Delta u = 0$  for  $\theta = 0$ . This is because no incoherence is present when the wave propagates perpendicular to the tunnel.

As in the previous section, the trend in Figure 12.3 is very similar for all three models. This is more evidently seen in Figure 12.4, where the deformations has been normalized. Thus, it is indicated that both the Winkler model and the closed form solution, even though the absolute values of the calculated deformations are highly conservative, advantageous could be used for some parameter studies.



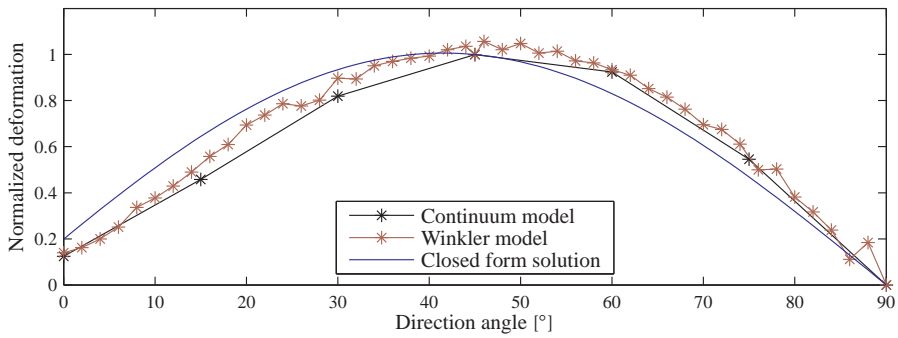
(a) Continuum model



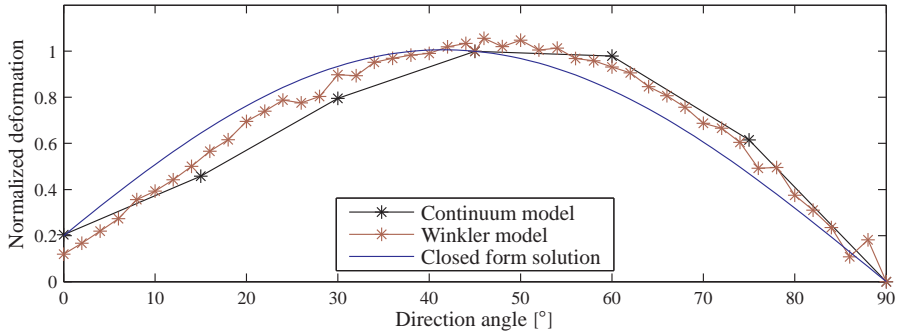
(b) Winkler model

**Figure 12.3:** Maximum deformation in gasket corner shown in Figure 10.1.

# Direction



(a) Gasket opening



(b) Gasket compression

Figure 12.4: Results from Figure 12.3 with deformation normalized for an angle of  $45^\circ$ .

## 12.3 Earthquake amplitude

The model is fully linear, and therefore should the gasket deformations – together with all other displacements and their derivatives – be directly proportional to a scaling of the input displacements. This has been verified through calculations in the Winkler and the continuum model; the closed form solution is omitted since the proportionality is very obvious seen from (7.1) on page 53. The displacement time series has been scaled with a varying factor, and the results are plotted in Figure 12.5.

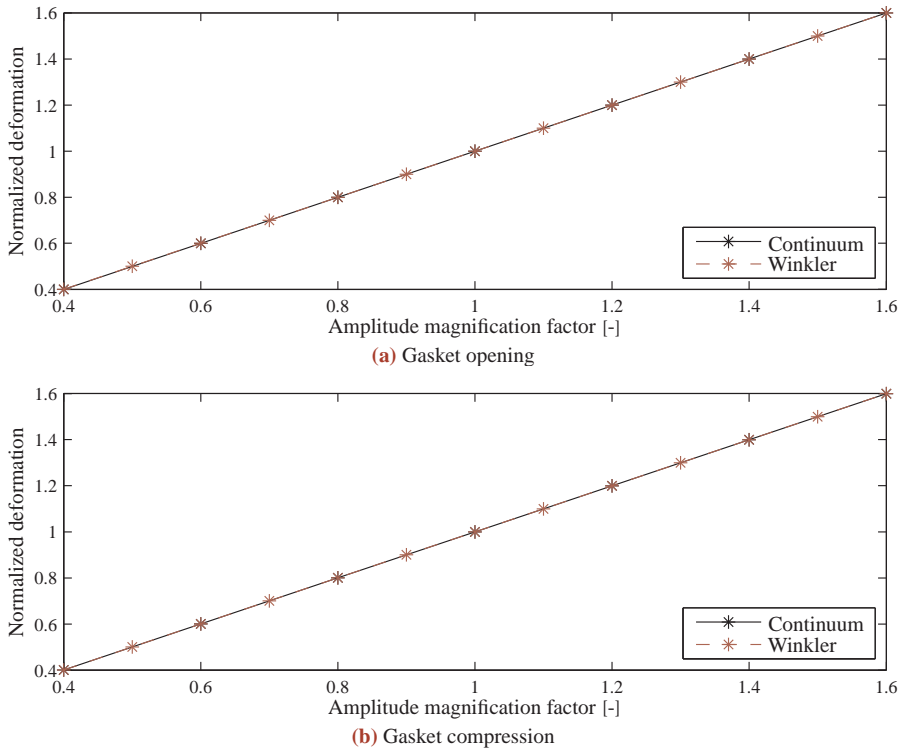


**Figure 12.5:** Normalized maximum deformation in gasket corner shown in Figure 10.1.

It can be seen that a scaling of the input displacement time series yields the very same scaling of the gasket deformations, thus verifying the linearity of the models. In the real world tunnel, this will only apply if the deformation state in the soil and structure is in the range where linear behaviour can be approximated.

## MODELLING OF GASKET JOINTS

As it is discussed in Section 5.6, the modelling of the Gina gaskets is not trivial. A linear approximation has been made, all though the behaviour is highly non-linear, both in the longitudinal and in the transverse and vertical direction.

As in Chapter 12, the continuum model and the Winkler model are used for the sensitivity analyses. However, since the gasket behaviour is not included in the closed form solution, this is omitted.

### 13.1 Longitudinal stiffness

The axial (longitudinal) stiffness of the Gina gaskets is highly non-linear, as presented in Section 5.6.1. A linearization has been made based on the gasket compression during the installation of the tunnel. As the gasket is compressed or opened, the actual stiffness will change rapidly. To give an indication of the impact of the linearization, a sensitivity analysis has been carried out.

The longitudinal gasket stiffness has been scaled with a factor, and in Figure 13.1 on the following page the damage to the reference gasket corner is plotted as function of the factor, for both the Winkler model and the continuum model.

As in Chapter 12 it is seen that the trend seems quite similar for the Winkler model and the continuum model. In Figure 13.2 this is more evidently seen as the normalized gasket deformation is plotted. The general trend is a slight decrease in the gasket deformation as the axial gasket stiffness is increased, as it would also be expected from a general static point of view. However, the change is very little, especially for the continuum model which is regarded the better one. This indicates that the modelling of the axial gasket stiffness should *not* be given very deep consideration when modelling the structure, since a variation in the stiffness does not affect the

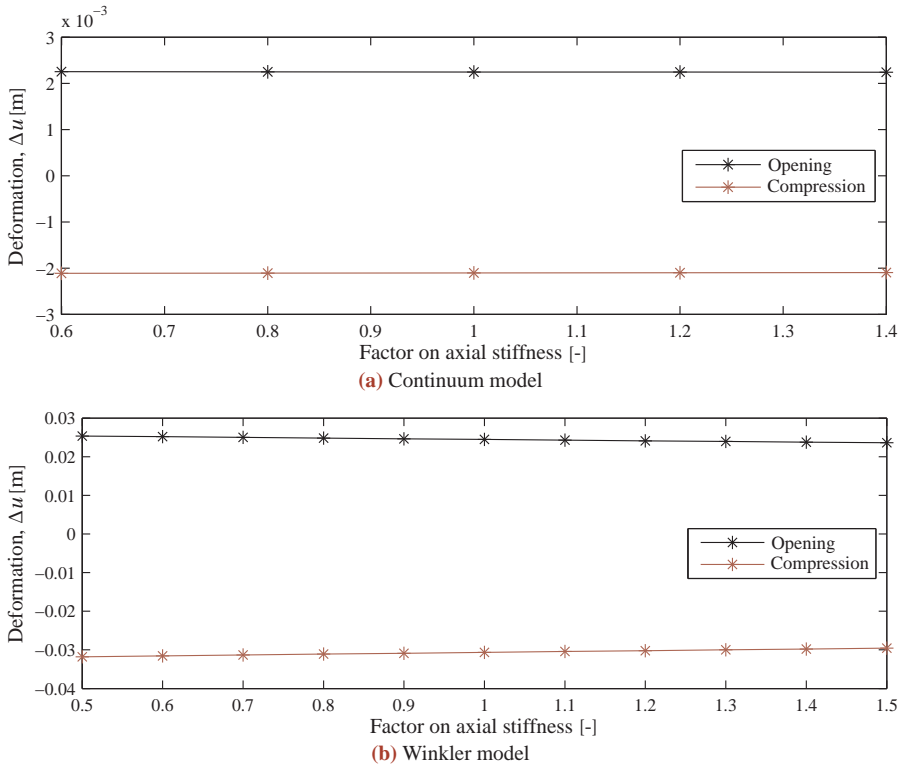


**Figure 13.1:** Maximum deformation in gasket corner shown in Figure 10.1.

gasket deformation significantly.

The results may be surprising, since it is documented in Chapter 10 that the axial deformation is very highly affective on the gasket deformation. The reason that variations of the axial gasket stiffness has very little effect on the gasket deformation is deemed to be the great difference between the stiffness of the tunnel elements and the axial gasket stiffness. The axial gasket stiffness make up approximately  $\frac{3.98 \cdot 10^6}{40 \cdot 10^9} = 0.1\%$  of the tunnel element stiffness. Since the tunnel is surrounded by soil, the overall displacements are governed by the soil motion and thus, it does not make very much difference if the gasket stiffness comprises 0.10‰ or 0.15‰ of the tunnel stiffness – the majority of the deformation is still lumped in the gasket.

## Shear stiffness

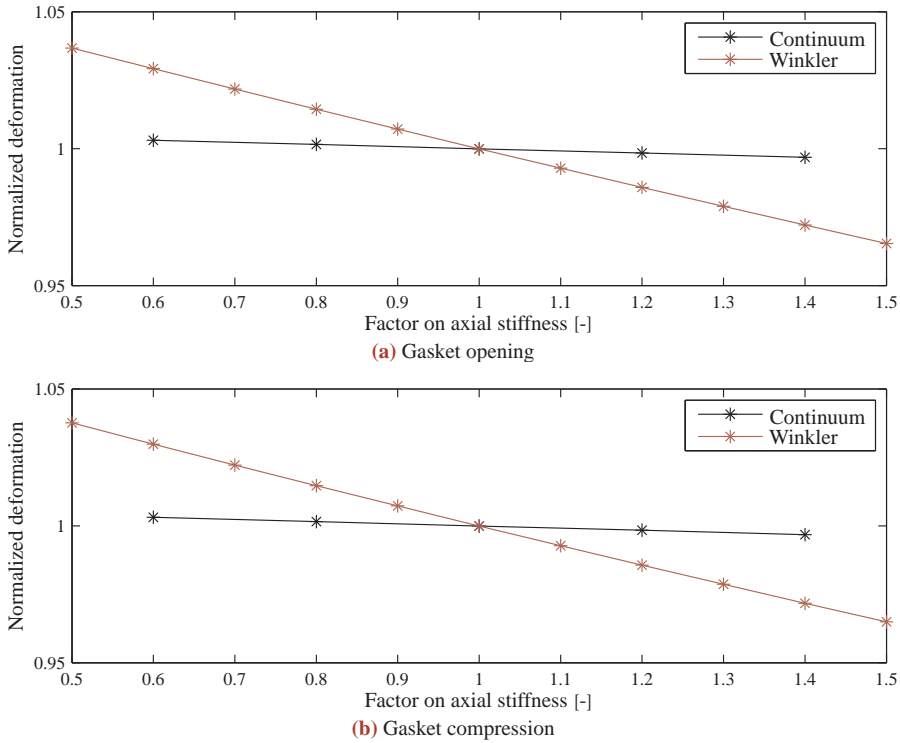


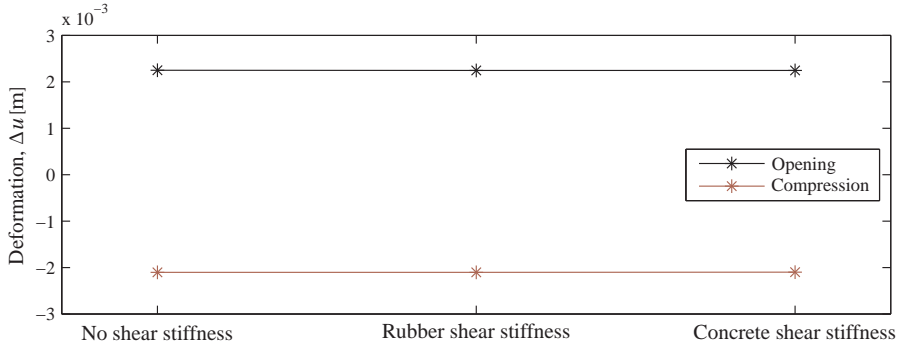
**Figure 13.2:** Results from Figure 13.1 with deformation normalized for the initial linearization of the gasket stiffness.

## 13.2 Shear stiffness

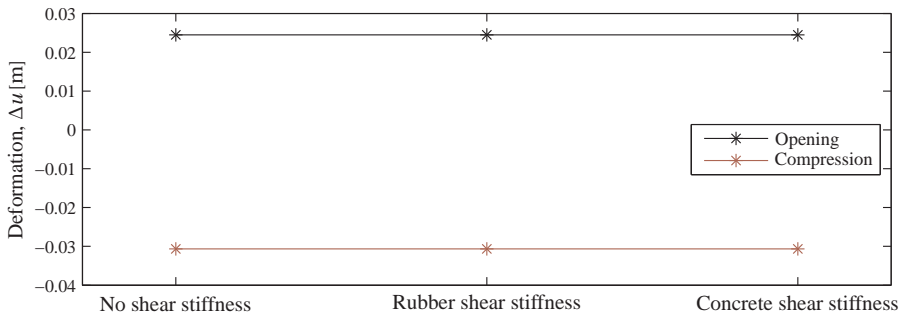
The choice of an appropriate shear stiffness for the gasket is discussed in Section 5.6.2. In this thesis, it has been chosen to use a shear stiffness of the joint corresponding to the shear stiffness of the rubber gasket itself, disregarding the shear keys of concrete.

As a sensitivity analysis, the gasket shear stiffness have been set to both zero and equivalent to the shear stiffness of the concrete tunnel elements, in two different calculations. The shear stiffness equivalent to concrete is used to model the shear keys in action as an upper value of the stiffness. For the continuum model this corresponds to shear modulus of  $G = 0\text{Pa}$  and  $G = 17.4 \cdot 10^9\text{Pa}$ , respectively. For comparison, the reference shear modulus of the rubber gasket profile is  $G = 1.3 \cdot 10^6\text{Pa}$ . The results for the Winkler model and for the continuum model are depicted in Figure 13.3 and Figure 13.4.

It is clearly seen that the magnitude of the gasket shear stiffness does not influence significantly on the gasket deformation. Thus, as for the axial gasket stiffness, the cross axial gasket stiffness should not be given significant considerations when modelling the immersed tunnel for a final design. The reason for this is primarily deemed to be the definition of damage in the present thesis, since transverse deformation does not contribute significantly to the total gasket deformation. In Figure 13.5 the maximum transverse deformation is plotted. It can be seen that the introduction of a shear stiff-



(a) Continuum model

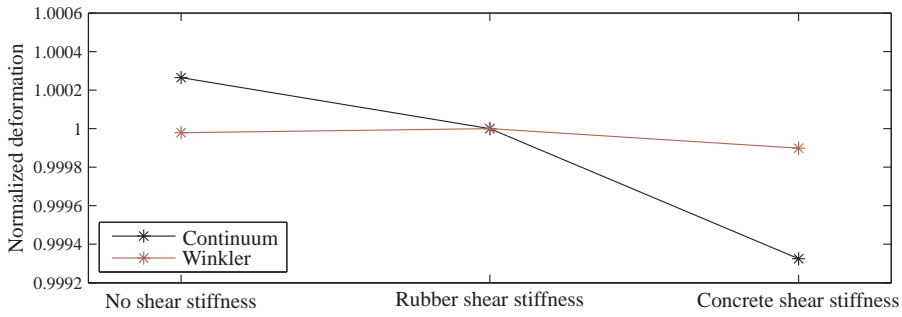


(b) Winkler model

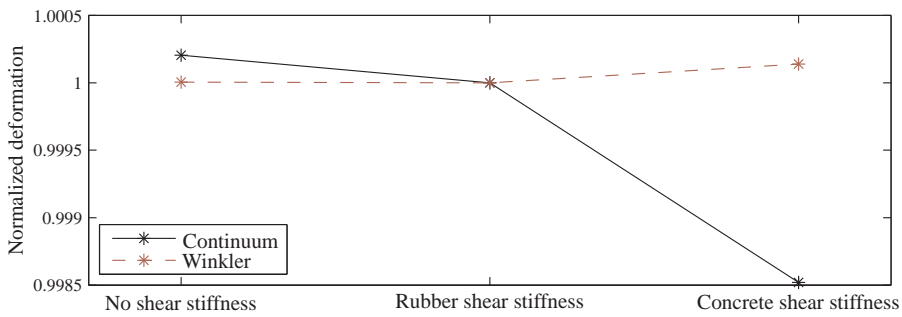
**Figure 13.3:** Maximum deformation in gasket corner shown in Figure 10.1.

ness like concrete *does* decrease the transverse gasket deformation significantly, from 1.1 mm to 0.06 mm, but this does not influence significantly on the final deformation.

## Shear stiffness



(a) Gasket opening



(b) Gasket compression

**Figure 13.4:** Results from Figure 13.3 with deformation normalized for the rubber shear stiffness.

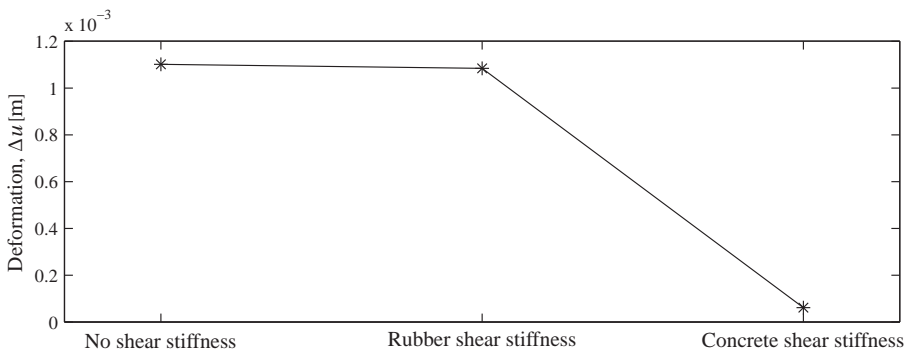


**Figure 13.5:** Maximum transverse deformation in gasket corner shown in Figure 10.1, for the continuum model.



## BIBLIOGRAPHY

- ANASTASIOS ANASTASIADIS, DIMITRIOS RAPTAKIS & KYRIAZIS PITILAKIS, 2001. *Thessaloniki's Detailed Microzoning: Subsurface Structure as Basis for Site Response Analysis*. *Pure and Applied Geophysics*, volume 158:pp. 2597–2633.
- IOANNIS ANASTASOPOULOS, NIKOS GEROLYMOS, VASILEIOS DROSOS, RALLIS KOURKOULIS, TAKIS GEORGARAKOS & GEORGE GAZETAS, 2007. *Nonlinear Response of Deep Immersed Tunnel to Strong Seismic Shaking*. *Journal of geotechnical and geoenvironmental engineering*, volume 133:pp. 1067–1090. ISSN 1090-0241/2007/9-1067–1090.
- LARS ANDERSEN, 2006. *Linear Elastodynamic Analysis*. DCE Lecture Notes No. 3. Dept. of Civil Engineering, Aalborg University, 1<sup>st</sup> edition.
- LARS ANDERSEN, 2007. *Lecture Slides from the course in Elastodynamics*. Aalborg University.
- LARS ANDERSEN, SØREN R. K. NIELSEN & STEEN KRENK, 2007. *Numerical methods for analysis of structure and ground vibration from moving loads*. *Computers & Structures*, volume 85:pp. 43–58.
- A. BAMBERGER, B. CHALINDARS, P. JOLY, J. E. ROBERTS & J.L. TERON, 1990. *Radiation boundary conditions for elastic wave propagation*. *SIAM Journal on Numerical Analysis*, volume 27(4):pp. 831–869. ISSN 0036-1429.
- ESBEN BYSKOV, 2002. *Elementary Continuum Mechanics for Everyone - and Some More*. "I need it like I need another hole in my head". Dept. of Building Technology and Structural Engineering, Aalborg University, 4<sup>th</sup> edition.
- RAY W. CLOUGH & JOSEPH PENZIEN, 1975. *Dynamics of structures*. McGraw-Hill Book Company. ISBN 0-07-011392-0.
- COMMONS, 2006. *Tectonic plate map with its relative movements*. Wikimedia Commons. [http://upload.wikimedia.org/wikipedia/commons/8/8a/Plates\\_tect2\\_en.svg](http://upload.wikimedia.org/wikipedia/commons/8/8a/Plates_tect2_en.svg).
- COMMONS, 2007. *Oceanic spreading ridge*. Wikimedia Commons. [http://en.wikipedia.org/wiki/Image:Oceanic\\_spreading.svg](http://en.wikipedia.org/wiki/Image:Oceanic_spreading.svg).
- COMMONS, 2008. *ADBC (Agriculture Development Bank of China) branch in Bei Chuan after earthquake*. Wikimedia Commons. [http://en.wikipedia.org/wiki/Image:ADBC\\_Branch\\_in\\_BeiChuan\\_after\\_earthquake.jpg](http://en.wikipedia.org/wiki/Image:ADBC_Branch_in_BeiChuan_after_earthquake.jpg).

## Bibliography

- COWI, 1995. *Time series from Aegion 1995 earthquake*. Delivered by Michael Tonnesen, 7 March 2008.
- COWI, 2007. *Internal information on Thessaloniki Submerged Tunnel*.
- COWI, 2008. *Grafik, Thessaloniki tunnel*. [http://www.cowi.dk/NR/rdonlyres/612E13BE-FAED-4CAA-A943-805EB593C773/0/Tunnel\\_2.pdf](http://www.cowi.dk/NR/rdonlyres/612E13BE-FAED-4CAA-A943-805EB593C773/0/Tunnel_2.pdf).
- DAEWOO, 2004. *Busan-Geoje Fixed Link - Immersed Tunnel, Seismic Analysis and Design*. Daewoo Engineering & Construction CO. Ltd.
- DGF, 2005. *Funderingshåndbogen*. DGF-bulletin no. 18. Danish Geotechnical Society. ISBN 87-89833-16-3.
- DAVID J. DOWRICK, 1987. *Earthquake resistant design*. John Wiley & Sons, 2<sup>nd</sup> edition. ISBN 0-471-91503-3.
- DS411, 1999. *Code of Practice for the Structural Use of Concrete*. Dansk Standard. ICS: 91.080.40.
- EAK, 2000. *Greek code for seismic resistant structures*. Organization of seismic resistant planning and protection. Unofficial Translation for EOAE.
- EN 1998-1, 2003. *Eurocode 8: Design of structures for earthquake resistance. Part 1: General rules, seismic actions and rules for buildings*. European Committee for Standardization. ICS: 91.120.20, Final Draft.
- M. FARDIS, E. CARVALHO, A. ELNASHAI, E. FACCIOLI, P. PINTO & A. PLUMIER, 2005. *Designers' guide to EN 1998-1 and EN 1998-5: Eurocode 8: Design of structures for earthquake resistance*. Designers' guide to the Eurocodes. Thomas Telford. ISBN 0-7277-3348-6.
- CARLOS A. FELIPPA, 2004. *Introduction to Finite Element Methods*. Department of Aerospace Engineering Sciences and Center for Aerospace Structures, University of Colorado. <http://www.colorado.edu/engineering/CAS/courses/d/IFEM.d/>.
- HERBERT GOLDSTEIN, 1980. *Classical Mechanics*. Addison-Wesley.
- GOOGLE EARTH, 2008. *Aerial view of Thessaloniki*. <http://earth.google.com/>.
- YOUSSEF M. A. HASHASH, JEFFREY J. HOOK, BIRGER SCHMIDT & JOHN I-CHIANG YAO, 2001. *Seismic design and analysis of underground structures. Tunnel and Underground Space Technology*, volume 16.
- R. L. HIGDON, 1992. *Absorbing boundary conditions for acoustic and elastic waves in stratified media*. *Journal of computational physics*, volume 101:p. 386–418. ISSN 0021-9991.
- ITA, 1999. *Immersed tunnels - a better way to cross waterways?* International Tunnelling and Underground Space Association. <http://www.ita-aites.org/cms/159.html>.

## Bibliography

- TINA NYGAARD JENSEN & RIKKE FREJO JØRGENSEN, 2006. *Seismic reliability analysis of plane frame structure*. Master's thesis, Aalborg University.
- O. KIYOMIYA, 1995. *Earthquake-resistant Design Features of Immersed Tunnels in Japan*. *Tunnelling and Underground Space Technology*, volume 10(4):pp. 463–475.
- STEVEN LAWRENCE KRAMER, 1996. *Geotechnical Earthquake Engineering*. Prentice Hall. ISBN 0-13-374943-6.
- STEEN KRENK, 2001. *Dispersion-corrected explicit integration of the wave equation*. *Archives of Computational Methods in Appl. Mech. Engrg.* 191 (2001) 975-987.
- W.B. KRÄTZIG & H.-J. NIEMANN, 1996. *Dynamics of civil engineering structures*. A. A. Balkema Publishers.
- SØREN R. K. NIELSEN, 2004. *Vibration Theory, Vol. 1, Linear Vibration Theory*. Aalborg tekniske Universitetsforlag, 3<sup>rd</sup> edition.
- SØREN R. K. NIELSEN, 2007. *Structural Dynamics, Vol. 9, Computational Dynamics*. Aalborg tekniske Universitetsforlag, 2<sup>nd</sup> edition.
- S. OKAMOTO, C. TAMURA, K. KATO & M. HAMADA, 1973. *Behaviors of submerged tunnels during earthquakes*. *Proceedings of the Fifth World Conference on Earthquake Engineering*, volume 1:pp. 544–553.
- G. N. OWEN & R. E. SCHOLL, 1981. *Earthquake engineering of large underground structures*. *Federal Highway Administration and National Science Foundation*. Report no. FHWA/RD-80/195.
- PIANC, 2001. *Seismic design guidelines for port structures*. Working Group No. 34 of the Maritime Navigation Commission, International Navigation Association. A. A. Balkema publishers.
- KYRIAZIS PITILAKIS, ANASTASIOS ANASTADIADIS, DIMITRIOS RAPTAKIS, NIKOLAOS BOUSSOULAS & ELENA PAPAGEORGIU, 2007. *Seismic design loads for metropolitan subway tunnels: The case of Thessaloniki metro*. *4<sup>th</sup> International Conference on Earthquake Geotechnical Engineering*. Paper no. 1700.
- M. S. POWER, D. ROSIDI & J. KANESHIRO, 1996. *Strawman: screening, evaluation and retrofit design of tunnels*. *Report Draft*. National Center for Earthquake Engineering Research, Buffalo, New York.
- C. F. SEMBLAT & J. J. BROIST, 2000. *Efficiency of higher order finite elements for the analysis of seismic wave propagation*. *Journal of Sound and Vibration*, volume 231(2):pp. 460–467.
- SIMULIA, 2007. *ABAQUS version 6.7 documentation*.
- C. M. ST JOHN & T. F. ZAHRAH, 1987. *Aseismic Design of Underground Structures*. *Tunnel and Underground Space Technology*, volume 2(2):pp. 165–197.
- JESPER W. STÆRDAHL, LARS ANDERSEN & JOHAN CLAUSEN, 2007. *Linear MATLAB FEM program for FEM courses on Aalborg University*.

## Bibliography

MICHAEL TONNESEN, 2008. *Guidance. Michael is Senior Project Manager at COWI.*

TRELLEBORG, 2007. *Gina gasket brochure.* [www.trelleborg.com/bakker/files/pdf\\_eng/Gina\\_eng.pdf](http://www.trelleborg.com/bakker/files/pdf_eng/Gina_eng.pdf).

CHRISTOS VRETTOS, BASIL KOLIAS, TELEMACHOS PANAGIOTAKOS & THOMAS RICHTER, 2007. *Seismic response analysis of an immersed tunnel using imposed deformations. 4<sup>th</sup> International Conference on Earthquake Geotechnical Engineering.* Paper no. 1473.

O.C. ZIENKIEWICZ & R.L. TAYLOR, 1989. *The Finite Element Method.* McGraw-Hill Book Company, London, 4<sup>th</sup> edition.

All URL's were available for Internet access on June 1, 2008.

# APPENDICES





## DERIVATION OF THE DOMAIN TRANSFORMATION METHOD

In this section the domain transformation method is derived, based upon (Andersen 2006). The bases for the method are outlined in Chapter 6, and the coordinates and layer indices used refer to Figure 6.2 on page 44.

### A.1 Constitutive model

The material model is in Section 6.1 given as homogeneous, isotropic and linear viscoelastic. The general constitutive model for a layer of such material is given by

$$\hat{\sigma}_{ik}^j = \lambda^j \hat{\epsilon}_{ll} \delta_{ik} + 2\mu^j \hat{\epsilon}_{ik}, \quad \hat{\epsilon}_{ik}^j = \frac{1}{2} \left( \frac{\partial U_i^j}{\partial x_k} + \frac{\partial U_k^j}{\partial x_i} \right) \quad (\text{A.1})$$

(Byskov 2002, p96), where the *hat* (^) signifies the formulation in the frequency domain. For hysteretic damping to be applied, the Lamé constants  $\lambda$  and  $\mu$  are expressed in terms of Young's modulus  $E$ , Poisson's ratio  $\nu$ , the circular frequency  $\omega$  and the loss factor  $\eta$  as

$$\begin{aligned} \lambda &= \lambda' \cdot (1 + i \text{sign}(\omega)\eta), & \lambda' &= \frac{\nu E}{(1 + \nu)(1 - 2\nu)} \\ \mu &= \mu' \cdot (1 + i \text{sign}(\omega)\eta), & \mu' &= \frac{E}{2(1 + \nu)} \end{aligned} \quad (\text{A.2})$$

(Andersen 2007)

## A.2 Governing equation

The layers ( $j = 1 \dots J$ ) are one by one regarded as linear elastic, isotropic and homogeneous media. The equations of motion for such media are for the general three-dimensional case the *Navier equations*

$$(\lambda + \mu) \frac{\partial^2 u_j}{\partial x_i \partial x_j} + \mu \frac{\partial^2 u_i}{\partial x_j \partial x_j} + \rho b_i = \rho \frac{\partial^2 u_i}{\partial t^2} \quad (\text{A.3})$$

where the conventions of index notation applies,  $u_i$  is the displacement in the direction of the coordinate  $x_i$ ,  $\rho$  is the mass density,  $b_i$  is the body forces per unit mass and  $t$  is the time coordinate.

In (A.3) nearly all terms reduces to zero when the simplified problem is observed. Since a vertically propagating SH-wave is considered, no vertical movement occurs, *i.e.*  $u_3^j = 0$ , with  $j$  and 3 indicating the  $j^{\text{th}}$  layer and the  $x_3$ -coordinate, respectively. Furthermore, the system of coordinates is oriented such that the wave motion is in the  $x_1$ -direction, providing  $u_2^j = 0$ .

The wave propagates in the  $x_3$ -direction. Thus, for a given  $x_3$ -coordinate the same displacement occurs for all  $x_1$  and  $x_2$ , *i.e.*  $\partial u_i^j / \partial x_1 = \partial u_i^j / \partial x_2 = 0$ .

If these simplifications for the SH-wave are incorporated into (A.3) and body forces are disregarded, the following one-dimensional wave equation, which governs the wave propagation, is found.

$$\frac{\partial^2 u^j(z, t)}{\partial z^2} = \frac{1}{(c_S^j)^2} \frac{\partial^2 u^j(z, t)}{\partial t^2}, \quad z = x_3, \quad u^j(z, t) = u_1^j(x_3, t), \quad c_S^j = \sqrt{\frac{\mu^j}{\rho^j}} \quad (\text{A.4})$$

where the  $z$ -coordinate is introduced together with the shear wave velocity  $c_S$ .

## A.3 Transformation into frequency domain

The governing equation (A.4) is formulated in the time domain (indicated by the presence of the time coordinate). The relation between the time and frequency domain representation of the displacement is provided by the inverse Fourier transformation

$$u^j(z, t) = \frac{1}{2\pi} \int_{-\infty}^{\infty} U^j(z, \omega) e^{i\omega t} d\omega \quad (\text{A.5})$$

The integral in (A.5) can be discretised to a complex Fourier series; a sum of  $N$  discrete harmonic waves with the frequency  $\omega_n$  as:

$$u^j(z, t) \approx \sum_{n=1}^N U_n^j(z) e^{i\omega_n t} \quad (\text{A.6})$$

## Relation between the layers

Each term of (A.6),  $u_n^j(z, t) = U_n^j(z) e^{i\omega_n t}$ , can be inserted into (A.4). The second-order derivatives of the term are

$$\begin{aligned}\frac{\partial^2 u_n^j(z, t)}{\partial z^2} &= \frac{\partial^2 U_n^j(z)}{\partial z^2} e^{i\omega_n t} \\ \frac{\partial^2 u_n^j(z, t)}{\partial t^2} &= (i\omega_n)^2 U_n^j(z) e^{i\omega_n t} = -\omega_n^2 U_n^j(z) e^{i\omega_n t}\end{aligned}\quad (\text{A.7})$$

and applied in (A.4) this yields

$$\begin{aligned}\frac{\partial^2 U_n^j(z)}{\partial z^2} e^{i\omega_n t} &= -\frac{1}{(c_S^j)^2} \omega_n^2 U_n^j(z) e^{i\omega_n t} \\ \frac{\partial^2 U_n^j(z)}{\partial z^2} &= -\frac{1}{(c_S^j)^2} \omega_n^2 U_n^j(z) = -(k_n^j)^2 U_n^j(z)\end{aligned}\quad (\text{A.8})$$

where the wave number  $k_n^j = \omega_n / c_S^j$  is introduced. (A.8) represents the equation of motion in the frequency domain for the  $n^{\text{th}}$  frequency of the  $j^{\text{th}}$  layer.

A local  $z^j$ -axis is applied for every layer, as shown in Figure 6.2 on page 44. The height of each layer is denoted  $h^j$ , and (A.8) is a constant-coefficient differential equation with the solution

$$U_n^j(z^j) = B_n^j e^{ik_n^j z^j} + C_n^j e^{-ik_n^j(z^j - h^j)} \quad (\text{A.9})$$

where  $B_n^j$  and  $C_n^j$  are integration constants.

Now the stresses can be found from the displacements through the constitutive relation (A.1) on page 129. As indicated in Section A.2, only the partial derivative  $\partial U_1^j / \partial x_3$  is different from zero, which simplifies (A.1) to

$$\hat{\sigma}_{13}^j = \hat{\sigma}_{31}^j = \mu^j \frac{\partial U_1^j}{\partial x_3} \quad (\text{A.10})$$

By utilization of (A.9) and  $x_3 = z$ , and by introducing the stress amplitude  $P_n^j(z^j) = \hat{\sigma}_{13}^j$ , (A.10) ends up to

$$P_n^j(z^j) = ik_n^j \mu^j \left( B_n^j e^{ik_n^j z^j} - C_n^j e^{ik_n^j(z^j - h^j)} \right) \quad (\text{A.11})$$

## A.4 Relation between the layers

Two auxiliary matrices  $\mathbf{S}_n^j$  and  $\mathbf{A}_n^j$  which gathers the strain and stresses, are now introduced as

$$\mathbf{S}_n^j(z^j) = \begin{bmatrix} U_n^j(z^j) \\ P_n^j(z^j) \end{bmatrix} = \mathbf{A}_n^j(z^j) \begin{bmatrix} B_n^j \\ C_n^j \end{bmatrix} \quad (\text{A.12})$$

$\mathbf{A}_n^j$  is defined according to (A.9) and (A.11) as

$$\mathbf{A}_n^j(z^j) = \begin{bmatrix} e^{ik_n^j z^j} & e^{-ik_n^j(z^j - h^j)} \\ ik_n^j \mu^j e^{ik_n^j z^j} & -ik_n^j \mu^j e^{-ik_n^j(z^j - h^j)} \end{bmatrix} \quad (\text{A.13})$$

Now, the relation between the strain and stresses  $\mathbf{S}_n^j$  at the top and the bottom of a layer can be found. Superscript 0 and 1 signifies the top and bottom of the layer, respectively, *i.e.* the requested relation is between  $\mathbf{S}_n^{j0} = \mathbf{S}_n^j(z^j = 0)$  and  $\mathbf{S}_n^{j1} = \mathbf{S}_n^j(z^j = h^j)$ . Through evaluation of (A.12) the relation is found as

$$\begin{aligned} \{\mathbf{A}_n^j(z^j = 0)\}^{-1} \mathbf{S}_n^j(z^j = 0) &= \begin{bmatrix} B_n^j \\ C_n^j \end{bmatrix} = \{\mathbf{A}_n^j(z^j = h^j)\}^{-1} \mathbf{S}_n^j(z^j = h^j) \\ \Rightarrow \mathbf{S}_n^{j0} &= \mathbf{A}_n^{j0} \{\mathbf{A}_n^{j1}\}^{-1} \mathbf{S}_n^{j1} \end{aligned} \quad (\text{A.14})$$

It is observed that  $\mathbf{S}_n^{j0}$  is found through simple multiplication of matrices onto  $\mathbf{S}_n^{j1}$ , a very fast operation for a computer, relative to inversion of large matrices.

Continuity is now required in the interfaces between the layers. In other words, it is required that the displacement is identical in the interface and that equilibrium is fulfilled, *i.e.*  $\mathbf{S}_n^{j0} = \mathbf{S}_n^{j-1,1}$ . This demand makes it possible to establish a simple relation between the top of the topmost layer  $\mathbf{S}_n^{10}$  and the bottom of the bottommost layer  $\mathbf{S}_n^{J1}$  through reiterated application of (A.14).

$$\begin{aligned} \mathbf{S}_n^{10} &= \mathbf{A}_n^{10} \{\mathbf{A}_n^{11}\}^{-1} \mathbf{S}_n^{11} = \mathbf{A}_n^{10} \{\mathbf{A}_n^{11}\}^{-1} \mathbf{S}_n^{20} = \mathbf{A}_n^{10} \{\mathbf{A}_n^{11}\}^{-1} \mathbf{A}_n^{20} \{\mathbf{A}_n^{21}\}^{-1} \mathbf{S}_n^{21} = \dots \\ &= \mathbf{A}_n^{10} \{\mathbf{A}_n^{11}\}^{-1} \mathbf{A}_n^{20} \{\mathbf{A}_n^{21}\}^{-1} \dots \mathbf{A}_n^{J0} \{\mathbf{A}_n^{J1}\}^{-1} \mathbf{S}_n^{J1} \end{aligned} \quad (\text{A.15})$$

The *transfer matrix*  $\mathbf{T}_n$  is then introduced, which reduces (A.15) to

$$\mathbf{S}_n^{10} = \mathbf{T}_n^{10} \mathbf{S}_n^{J1}, \quad \mathbf{T}_n^{10} = \mathbf{A}_n^{10} \{\mathbf{A}_n^{11}\}^{-1} \mathbf{A}_n^{20} \{\mathbf{A}_n^{21}\}^{-1} \dots \mathbf{A}_n^{J0} \{\mathbf{A}_n^{J1}\}^{-1} \quad (\text{A.16})$$

## A.5 Boundary conditions

The boundary conditions of the problem are: 1) No shear stress at the top of the topmost layer,  $P_n^{10} = 0$ , and 2) An earthquake-induced displacement at the bottom of the bottommost layer,  $U_n^{J1} = \bar{U}_n$ . The boundary conditions are introduced in (A.16) which yields the equation

$$\begin{bmatrix} U_n^{10} \\ 0 \end{bmatrix} = \begin{bmatrix} T_{11}^{10} & T_{12}^{10} \\ T_{21}^{10} & T_{22}^{10} \end{bmatrix} \begin{bmatrix} \bar{U}_n \\ P_n^{J1} \end{bmatrix} \quad (\text{A.17})$$

Solving (A.17), the displacement at the top of the topmost layer can be found directly as a function of the earthquake induced displacement.

$$U_n^{10} = \left( T_{11}^{10} - \frac{T_{12}^{10} T_{21}^{10}}{T_{22}^{10}} \right) \bar{U}_n = H_n^{10} \bar{U}_n, \quad H_n^{10} = T_{11}^{10} - \frac{T_{12}^{10} T_{21}^{10}}{T_{22}^{10}} \quad (\text{A.18})$$

where the frequency response function  $H_n$  has been introduced. This may be computed for each harmonic wave component in the earthquake spectra according to (A.6).

## A.6 Solution for inner interfaces

If the deformations and stresses in the interfaces between layers is of interest, they can be computed easily by a generalization of the transfer matrix  $\mathbf{T}_n$ . For the top of the  $j^{\text{th}}$  layer  $\mathbf{T}_n^{j0}$  can be defined analogous to (A.16) on the preceding page:

$$\mathbf{S}_n^{j0} = \mathbf{T}_n^{j0} \mathbf{S}_n^{j1}, \quad \mathbf{T}_n^{j0} = \mathbf{A}_n^{j0} \{\mathbf{A}_n^{j1}\}^{-1} \mathbf{A}_n^{j+1,0} \{\mathbf{A}_n^{j+1,1}\}^{-1} \dots \mathbf{A}_n^{j0} \{\mathbf{A}_n^{j1}\}^{-1} \quad (\text{A.19})$$

The stress amplitude can be found from (A.17):

$$0 = \bar{U}_n T_{21}^{10} + P_n^{j1} T_{22}^{10} \Rightarrow P_n^{j1} = -\frac{\bar{U}_n T_{21}^{10}}{T_{22}^{10}} \quad (\text{A.20})$$

Hence, the displacements and stresses gathered in  $\mathbf{S}_n^{j0}$  can be determined from known values:

$$\mathbf{S}_n^{j0} = \begin{bmatrix} U_n^{j0} \\ P_n^{j0} \end{bmatrix} = \begin{bmatrix} T_{11}^{j0} & T_{12}^{j0} \\ T_{21}^{j0} & T_{22}^{j0} \end{bmatrix} \begin{bmatrix} \bar{U}_n \\ P_n^{j1} \end{bmatrix} \quad (\text{A.21})$$

where the deformation at the top of the  $j^{\text{th}}$  layer, analogous to (A.18), can be expressed explicitly as

$$U_n^{j0} = \left( T_{11}^{j0} - \frac{T_{12}^{j0} T_{21}^{10}}{T_{22}^{10}} \right) \bar{U}_n = H_n^{j0} \bar{U}_n, \quad H_n^{j0} = T_{11}^{j0} - \frac{T_{12}^{j0} T_{21}^{10}}{T_{22}^{10}} \quad (\text{A.22})$$



## DERIVATION OF THE FINITE ELEMENT METHOD FOR WAVE PROPAGATION

In this appendix, the finite element method (FEM) for the frequency response in a stratum is derived. The method and its application is outlined in Section 6.3. The method has been implemented in a MATLAB program, which is enclosed on the attached DVD.

This application of the FEM is performed in the frequency domain. This differs from the application of the FEM in the Winkler model, cf. Chapter 8, which is performed in the time domain.

In the FEM, a system of matrices is established and solved. The damping of the system is, as stated in Section 6.3, applied as hysteretic damping, which enters in the stiffness matrix  $\mathbf{K}$ . Thus, the equation of motion in the frequency domain is

$$(\mathbf{K} - \omega^2 \mathbf{M}) \mathbf{U} = \mathbf{F} \quad (\text{B.1})$$

where  $\mathbf{K}$  and  $\mathbf{M}$  are the stiffness and mass matrix, respectively,  $\mathbf{U}$  and  $\mathbf{F}$  are the displacement and load vector, respectively, and  $\omega$  is the circular frequency.

### B.1 Geometry and topology

The general geometry of the problem is sketched in Figure 6.2 on page 44. The geometry is discretized with finite elements. Each soil layer is discretized into a chosen number of soil elements, as it is depicted in Figure B.1 on the next page. As it is sketched in this figure, only the vertical coordinate,  $z$ , determines the node position. The displacement in the nodes are measured on a horizontal coordinate.

The soil elements are connected in nodes, and both the elements and the nodes are numbered ascending with the  $z$ -coordinate. In each layer, the soil parameters and the

element sizes are identical, which entails that the element matrices in each layer also are identical.

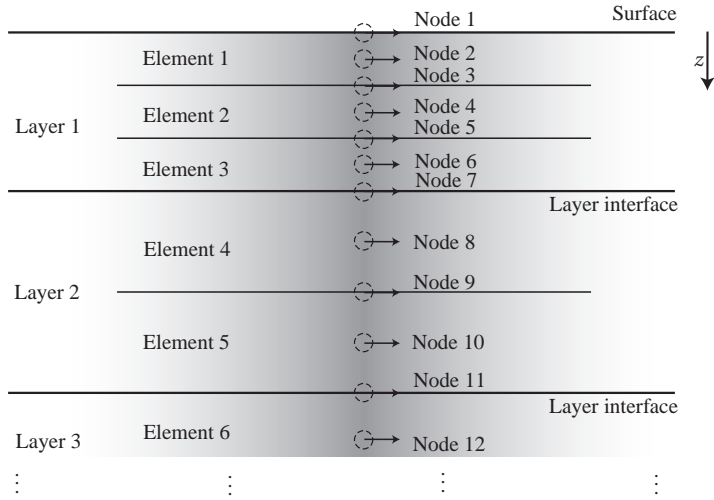


**Figure B.1:** Sketch of geometry and topology for the FEM.

## B.2 Element matrices

The element matrices for the soil elements are established on the basis of the chosen shape functions of the elements. As stated in Section 6.3.1, it is chosen to use second-order elements for the analysis. The second-order shape functions require a node in the middle of the element, as it is shown in Figure B.1. The shape functions are depicted in Figure 6.5 on page 46.

### B.2.1 Stiffness matrix

On the basis of the given shape functions, and taken the physics of the problem (shearing of a soil column with shear stiffness  $G$  and depth  $l_e$ ) into consideration, the stiffness matrix for a soil element may be formulated as

$$\mathbf{K}_e = \frac{G}{3l_e} \begin{bmatrix} 7 & -8 & 1 \\ -8 & 16 & -8 \\ 1 & -8 & 7 \end{bmatrix} \quad (\text{B.2})$$

(Felippa 2004, p32-11), where it should be remembered that  $G$  is modified to model hysteretic damping.

### B.2.2 Mass matrix

The mass matrix may be obtained in a number of ways, since an exact solution to model a continuum distributed mass does not exist. The mass matrix has been com-

## Solution of the system

bined of two ways of treating the mass: a *lumped* mass matrix and a *consistent* mass matrix.

The lumped mass matrix, (B.3), is a simple diagonal matrix, which models the mass as if it where lumped entirely at the nodes of the soil element. The division of the mass in portions of 1/6, 1/6 and 2/3 are obtained according to Simpson's rule.

$$\mathbf{M}_{e, \text{Imp}} = \frac{\rho l_e}{6} \begin{bmatrix} 1 & 0 & 0 \\ 0 & 4 & 0 \\ 0 & 0 & 1 \end{bmatrix} \quad (\text{B.3})$$

(Felippa 2004, p31-8)

The consistent mass matrix, (B.5) should in fact be called the *stiffness-consistent* mass matrix, since it is constructed by using the same shape functions, depicted in Figure 6.5, as used for the construction of the stiffness matrix.

The consistent mass matrix is calculated as

$$\mathbf{M}_{e, \text{cons}} = \int_0^L \mathbf{N}^T(x) \mu(x) \mathbf{N}(x) dx \quad (\text{B.4})$$

(Nielsen 2004, p153), where  $\mathbf{N}$  is the shape function matrix,  $\mu$  is the distributed mass, and  $L$  is the element length. For the second-order soil element this yields

$$\mathbf{M}_{e, \text{cons}} = \frac{\rho l_e}{30} \begin{bmatrix} 4 & 2 & -1 \\ 2 & 16 & 2 \\ -1 & 2 & 4 \end{bmatrix} \quad (\text{B.5})$$

(Felippa 2004, p31-8)

The goodness of the mass matrix chosen can be quantified in terms of its ability to preserve linear and angular momentum, and by modelling the dispersive behaviour of a continuum. It can be shown that the better combination of the lumped and consistent mass matrices is a simple linear combination,

$$M_e = \frac{M_{e, \text{cons}} + M_{e, \text{Imp}}}{2} \quad (\text{B.6})$$

(Felippa 2004, p31-5) (Krenk 2001)

The element matrices, the stiffness as well as the mass matrices, are assembled to the global system matrices according to the topology.

### B.3 Solution of the system

The solution of the system, (B.1), now follows easily. For clarity, a 'dynamic stiffness' is introduced as

$$\mathbf{K}_{\text{dyn}} = \mathbf{K} - \omega^2 \mathbf{M} \quad (\text{B.7})$$

The earthquake enters into the system through forced displacements,  $u_j = \bar{u}$ , at bedrock.  $J$  is the total number of nodes. The force vector,  $\mathbf{F}$  consists of zeroes. To account for this, the system is rewritten, similar to what has been showed in Section C.3, where

Appendix B. Derivation of the finite element method for wave propagation

further details can be found. The dynamic stiffness matrix are divided into four sub-matrices

$$\mathbf{K}_{\text{dyn}} = \begin{array}{c|c} \begin{array}{c} 1 \cdots (J-1) \\ \mathbf{K}_{\text{dyn},11} \end{array} & \begin{array}{c} J \\ \mathbf{K}_{\text{dyn},12} \end{array} \\ \hline \begin{array}{c} \mathbf{K}_{\text{dyn},21} \end{array} & \begin{array}{c} \mathbf{K}_{\text{dyn},22} \\ (1-J) \cdots 1 \end{array} \end{array} \quad (\text{B.8})$$

and the solution to the system, the unknown displacements  $\mathbf{U}_1$ , follows as

$$\mathbf{U}_1 = \mathbf{K}_{\text{dyn},11} (\mathbf{F} - \mathbf{K}_{\text{dyn},12} \cdot \bar{\mathbf{u}})^{-1} \quad (\text{B.9})$$



## ENHANCEMENTS TO FE WINKLER MODEL

The Winkler model, described in Chapter 8, has been coded in MATLAB on the basis of an existing linear FE program for static analysis, by Stærdahl *et al.* (2007). The program has been altered, so that a dynamic analysis with forced displacements can be carried out. In this appendix, the necessary enhancements to the existing program are described. What already was part of the program, *e.g.* the global matrix assembler and the element stiffness matrix for a beam element, is not described.

### Equations of motion

The basic set of equations which has to be solved is the global equation of motion

$$\mathbf{M}\ddot{\mathbf{u}}(t) + \mathbf{C}\dot{\mathbf{u}}(t) + \mathbf{K}\mathbf{u}(t) = \mathbf{f}(t) \quad (\text{C.1})$$

where  $\mathbf{u}$  signifies the displacement vector for the degrees of freedom,  $\mathbf{f}$  is the load vector,  $\mathbf{M}$ ,  $\mathbf{C}$  and  $\mathbf{K}$  is the mass, damping and stiffness matrices, respectively, and where a dot (·) signifies differentiation with respect to time.

### C.1 Damping and mass matrices

The damping,  $\mathbf{C}$ , and mass,  $\mathbf{M}$ , matrices are generated for each finite element and assembled to the global matrices according to the topology in the same way as the element stiffness matrices.

Since the analysis is performed in the time domain, viscous damping is applied cf. Section 5.3.4. Hence, the damping matrix is calculated by the use of (5.5)

$$\mathbf{C}_e = \beta \mathbf{K}_e \quad (\text{C.2})$$

where the damping coefficient  $\beta$  is given by (5.10) on page 31.

The soil springs and the gaskets are modelled as massless. Therefore, their element mass matrices are 12x12 zero-matrices. For the tunnel beam elements, the consistent element mass matrix,  $M_{e,cons}$ , can be calculated from the shape functions, similar to what has been done in Section B.2.2 with the help of (B.4). The consistent mass matrix ends up to

$$M_{e,cons} = \mu L \begin{bmatrix} \frac{1}{3} & 0 & 0 & 0 & 0 & 0 & \frac{1}{6} & 0 & 0 & 0 & 0 & 0 \\ 0 & \frac{13}{35} & 0 & 0 & 0 & \frac{11L}{210} & 0 & \frac{9}{70} & 0 & 0 & 0 & \frac{-13L}{420} \\ 0 & 0 & \frac{13}{35} & 0 & \frac{-11L}{210} & 0 & 0 & 0 & \frac{9}{70} & 0 & \frac{13L}{420} & 0 \\ 0 & 0 & 0 & \frac{1}{3} & 0 & 0 & 0 & 0 & 0 & \frac{1}{6} & 0 & 0 \\ 0 & 0 & \frac{-11L}{210} & 0 & \frac{L^2}{105} & 0 & 0 & 0 & \frac{-13L}{420} & 0 & \frac{-L^2}{140} & 0 \\ 0 & \frac{11L}{210} & 0 & 0 & 0 & \frac{L^2}{105} & 0 & \frac{13L}{420} & 0 & 0 & 0 & \frac{-L^2}{140} \\ \frac{1}{6} & 2 & 0 & 0 & 0 & 0 & \frac{1}{3} & 0 & 0 & 0 & 0 & 0 \\ 0 & \frac{9}{70} & 0 & 0 & 0 & \frac{13L}{420} & 0 & \frac{13}{35} & 0 & 0 & 0 & \frac{-11L}{210} \\ 0 & 0 & \frac{9}{70} & 0 & \frac{-13L}{420} & 0 & 0 & 0 & \frac{13}{35} & 0 & \frac{11L}{210} & 0 \\ 0 & 0 & 0 & \frac{1}{6} & 0 & 0 & 0 & 0 & 0 & \frac{1}{3} & 0 & 0 \\ 0 & 0 & \frac{13L}{420} & 0 & \frac{-L^2}{140} & 0 & 0 & 0 & \frac{11L}{210} & 0 & \frac{L^2}{105} & 0 \\ 0 & \frac{-13L}{420} & 0 & 0 & 0 & \frac{-L^2}{140} & 0 & \frac{-11L}{210} & 0 & 0 & 0 & \frac{L^2}{105} \end{bmatrix}$$

The lumped mass matrix,  $M_{e,imp}$ , is calculated by the ‘‘row-sum’’ method, where the lumped mass matrix is formed by adding the off-diagonal entries in each row of the consistent matrix to the diagonal entry, according to Zienkiewicz & Taylor (1989)

$$M_{e,imp} = \mu L \text{diag} \begin{bmatrix} \frac{1}{2} \\ \frac{1}{2} + \frac{3L}{140} \\ \frac{1}{2} - \frac{3L}{140} \\ \frac{1}{2} \\ -\frac{L}{12} + \frac{L^2}{420} \\ \frac{L}{12} + \frac{L^2}{420} \\ \frac{1}{2} \\ \frac{1}{2} - \frac{3L}{140} \\ \frac{1}{2} + \frac{3L}{140} \\ \frac{1}{2} \\ \frac{L}{12} + \frac{L^2}{420} \\ -\frac{L}{12} + \frac{L^2}{420} \end{bmatrix} \quad (C.3)$$

The lumped and consistent matrices are combined with (B.6) on page 137.

## C.2 Time integration

The numerical integration of the equations of motion, (C.1), is performed with a Newmark family algorithm. This family of algorithms is widely used in structural dynamics. To ensure unconditional stability, the Crank-Nicolson algorithm, which is a special case of the Newmark algorithm with the Newmark parameters  $(\beta, \gamma) = (\frac{1}{4}, \frac{1}{2})$ , has been employed. The time step is  $\Delta t = 0.01s$  as for the continuum model cf. Section 9.1.4. The Newmark family of algorithms has been documented by e.g. Nielsen (2007).

### C.3 Forced displacements

Since the earthquake does not influence the system through external loads, but through forced displacements as described in Section 4.4, the forces in the load vector  $\mathbf{f}(t)$  are unknown at the degrees of freedom with forced displacement. In stead, the forced displacements are introduced into the set of equations, thus rewriting (C.1) to

$$\begin{bmatrix} \mathbf{K}_{11} & \mathbf{K}_{12} \\ \mathbf{K}_{21} & \mathbf{K}_{22} \end{bmatrix} \begin{bmatrix} \bar{\mathbf{u}}_1 \\ \bar{\mathbf{u}}_2 \end{bmatrix} + \begin{bmatrix} \mathbf{C}_{11} & \mathbf{C}_{12} \\ \mathbf{C}_{21} & \mathbf{C}_{22} \end{bmatrix} \begin{bmatrix} \dot{\bar{\mathbf{u}}}_1 \\ \dot{\bar{\mathbf{u}}}_2 \end{bmatrix} + \begin{bmatrix} \mathbf{M}_{11} & \mathbf{M}_{12} \\ \mathbf{M}_{21} & \mathbf{M}_{22} \end{bmatrix} \begin{bmatrix} \ddot{\bar{\mathbf{u}}}_1 \\ \ddot{\bar{\mathbf{u}}}_2 \end{bmatrix} = \begin{bmatrix} \bar{\mathbf{f}}_1 \\ \bar{\mathbf{f}}_2 \end{bmatrix} \quad (\text{C.4})$$

where a bar ( $\bar{\quad}$ ) denotes a prescribed value, *i.e.* the known forced displacements, and the known forces in the degrees of freedom without prescribed displacements. All of these forces is zero in the present case.

The equations of (C.4) with prescribed forces can now be rewritten to

$$\mathbf{K}_{11}\mathbf{u}_1 + \mathbf{C}_{11}\dot{\mathbf{u}}_1 + \mathbf{M}_{11}\ddot{\mathbf{u}}_1 = (\bar{\mathbf{f}}_1 - \mathbf{K}_{12}\bar{\mathbf{u}}_2 - \mathbf{C}_{12}\dot{\bar{\mathbf{u}}}_2 - \mathbf{M}_{12}\ddot{\bar{\mathbf{u}}}_2) \quad (\text{C.5})$$

$$\tilde{\mathbf{K}}\tilde{\mathbf{u}} + \tilde{\mathbf{C}}\dot{\tilde{\mathbf{u}}} + \tilde{\mathbf{M}}\ddot{\tilde{\mathbf{u}}} = \tilde{\mathbf{f}} \quad (\text{C.6})$$

where tilde ( $\tilde{\quad}$ ) denotes reduced vectors and matrices, the definition of which should be clear from the rewriting of (C.5) to (C.6). The similarity between (C.6) and the basic equation of motion (C.1) should be noted. This form is easily implemented into standard Newmark schemes.

### C.4 Spring elements

Two new elements are introduced in the program: the soil spring element and the gasket element. Both are built on the basis of the three-dimension beam element, simply by editing the generated element matrices. The element matrices of the beam element are 12x12 matrices, since the beam element consists of three translational and three rotational degrees of freedom in each beam end. The stiffness matrix for the spring element is changed to a new 12x12 matrix, with the spring stiffness  $k$  in entries 1 and 7. Thus, only the axial translational degrees of freedom provide any stiffness.

$$\mathbf{K}_{e,\text{spring}} = \begin{bmatrix} k & 0 & \cdots & 0 & -k & & & & & & & \\ 0 & 0 & & & 0 & & & & & & & \\ \vdots & & \ddots & & \vdots & & & & & & & \\ 0 & & & & 0 & 0 & & & & & & \\ -k & 0 & \cdots & 0 & k & & & & & & & \\ & & & \mathbf{0}_{(5 \times 7)} & & & & & & & & \\ & & & & & & & & & & \mathbf{0}_{(5 \times 5)} & \end{bmatrix} \quad (\text{C.7})$$

Similarly, the gasket element is constructed from the beam element stiffness matrix. Since the shearing stiffness enters, uncoupled with other degrees of freedom, the 12x12 matrix is constructed with the longitudinal spring stiffness  $k_l$  in entries 1 and 7, and the shear spring stiffness  $k_s$  in entries 2, 3, 8 and 9. Thus, all translational

## Appendix C. Enhancements to FE Winkler model

degrees of freedom in the two element ends are coupled.

$$\mathbf{K}_{e,\text{spring}} = \begin{bmatrix} k_1 & & & -k_1 & & \\ & k_s & & & -k_s & \mathbf{0}_{(3 \times 3)} \\ & & k_s & & & -k_s \\ -k_1 & \mathbf{0}_{(3 \times 3)} & & \mathbf{0}_{(3 \times 3)} & \mathbf{0}_{(3 \times 3)} & \mathbf{0}_{(3 \times 3)} \\ & -k_s & & k_1 & k_s & \mathbf{0}_{(3 \times 3)} \\ & & -k_s & & & k_s \\ \mathbf{0}_{(3 \times 3)} & & \mathbf{0}_{(3 \times 3)} & \mathbf{0}_{(3 \times 3)} & \mathbf{0}_{(3 \times 3)} & \mathbf{0}_{(3 \times 3)} \end{bmatrix} \quad (\text{C.8})$$

## CROSS SECTION DATA

In this appendix, the data for the cross section of the immersed tunnel is outlined. The data is used throughout the thesis, *i.a.* in the Winkler model.

A typical cross section is presented in Figure 5.2 on page 28. For the present thesis, some simplifications of the geometry of the tunnel has been made. The cross section used in the thesis is presented in Figure D.1.

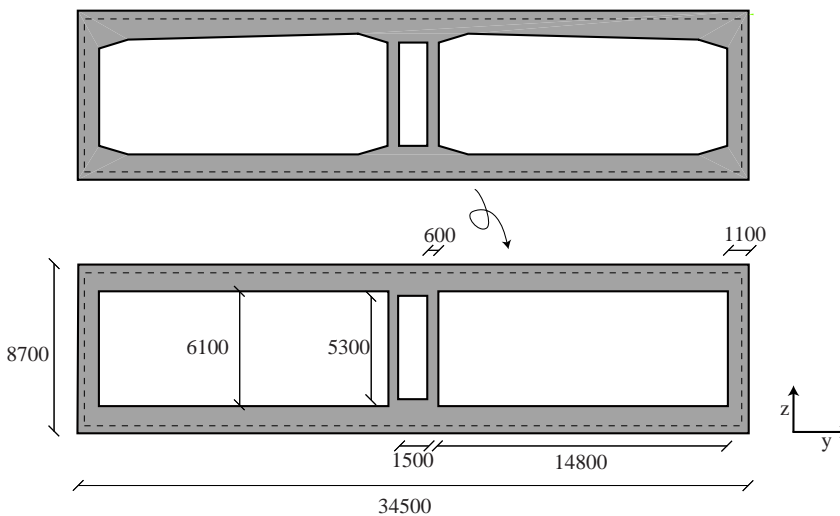


**Figure D.1:** Definition sketch of typical cross section of the tunnel. The dotted line around the perimeter shows the location of the Gina gasket. The section is both horizontal and vertical symmetric about the centre of gravity. All measures in mm. After COWI (2007).

## D.1 Length of gasket

Around the perimeter of the cross section, the Gina gasket is located. The total length  $L_{\text{gasket}}$  of the gasket is

$$L_{\text{gasket}} = 84.4 \text{ m}$$

## D.2 Area

The full area  $A_{\text{full}}$  and the solid area  $A_{\text{solid}}$  of the cross section of the tunnel can be calculated according to Figure D.1 to

$$\begin{aligned} A_{\text{full}} &= 300.2 \text{ m}^2 \\ A_{\text{solid}} &= 111.6 \text{ m}^2 \end{aligned}$$

## D.3 Second moment of area

The second moments of area around the centre of gravity are calculated as

$$\begin{aligned} I_{yy} &= \frac{1}{12} (34.5 \text{ m} \cdot (8.7 \text{ m})^3 - 2 \cdot 14.8 \text{ m} \cdot (6.1 \text{ m})^3 - 1.5 \text{ m} \cdot (5.3 \text{ m})^3) \\ &= 1315 \text{ m}^4 \\ I_{zz} &= \frac{1}{12} (8.7 \text{ m} \cdot (34.5 \text{ m})^3 - 5.3 \text{ m} \cdot (1.5 \text{ m})^3) \\ &\quad - 2 \left( \frac{1}{12} \cdot 6.1 \text{ m} \cdot (14.8 \text{ m})^3 + (8.75 \text{ m})^2 \cdot 6.1 \text{ m} \cdot 14.8 \text{ m} \right) \\ &= 12650 \text{ m}^4 \end{aligned}$$



## ROTATION MATRICES

To obtain results from the Winkler model, it is needed to rotate a vector in space, as it is described in Section 8.4.2. The rotation is obtained with transformation matrices. The notation follows Figure 8.13 on page 65.

The direction vector  $\vec{P}$  is transformed into the rotated direction vector  $\vec{P}_{\text{rot}}$  by multiplication with the transformation matrices  $\mathbf{R}_z$ ,  $\mathbf{R}_y$  and  $\mathbf{R}_x$ .

$$\vec{P}_{\text{rot}} = \mathbf{R}_z \cdot \mathbf{R}_y \cdot \mathbf{R}_x \cdot \vec{P} \quad (\text{E.1})$$

It should be noted that the order of the matrix multiplications in (E.1) in principle is *not* trivial. In general, it matters, which rotation is applied first, but in the present case the rotations are very small. In practical use, this makes the order of multiplication unimportant.

The rotation matrices are by *e.g.* Goldstein (1980, pp146-147) given as:

$$\mathbf{R}_z = \begin{bmatrix} \cos(\theta_z) & -\sin(\theta_z) & 0 \\ \sin(\theta_z) & \cos(\theta_z) & 0 \\ 0 & 0 & 1 \end{bmatrix} \quad (\text{E.2})$$

$$\mathbf{R}_y = \begin{bmatrix} \cos(\theta_y) & 0 & \sin(\theta_y) \\ 0 & 1 & 0 \\ -\sin(\theta_y) & 0 & \cos(\theta_y) \end{bmatrix} \quad (\text{E.3})$$

$$\mathbf{R}_x = \begin{bmatrix} 1 & 0 & 0 \\ 0 & \cos(\theta_x) & -\sin(\theta_x) \\ 0 & \sin(\theta_x) & \cos(\theta_x) \end{bmatrix} \quad (\text{E.4})$$